SLAC-624

STUDY OF HIGH TEMPERATURE SUPERCONDUCTORS WITH ANGLE-RESOLVED PHOTOEMISSION SPECTROSCOPY

Pavel Valer'evich Bogdanov

Stanford Synchrotron Radiation Laboratory
Stanford Linear Accelerator Center
Stanford University, Stanford, California 94309

SLAC-Report-624
December 2001

Prepared for the Department of Energy
under contract number DE-AC03-76SF00515

Printed in the United States of America. Available from the National Technical
Information Service, U.S. Department of Commerce,
5285 Port Royal Road, Springfield, VA 22161

---

* Ph.D. thesis, Stanford University, Stanford, CA 94309.

STUDY OF HIGH TEMPERATURE SUPERCONDUCTORS WITH ANGLE-RESOLVED PHOTOEMISSION SPECTROSCOPY

A DISSERTATION
SUBMITTED TO THE DEPARTMENT OF APPLIED PHYSICS
AND THE COMMITTEE ON GRADUATE STUDIES
OF STANFORD UNIVERSITY
IN PARTIAL FULFILLMENT OF THE REQUIREMENTS
FOR THE DEGREE OF
DOCTOR OF PHILOSOPHY

Pavel Valer'evich Bogdanov
December 2001

I certify that I have read this dissertation and that, in my opinion, it is fully adequate in scope and quality as a dissertation for the degree of Doctor of Philosophy.

Zhi-Xun Shen
(Principal Adviser)

I certify that I have read this dissertation and that, in my opinion, it is fully adequate in scope and quality as a dissertation for the degree of Doctor of Philosophy.

Sebastian Doniach

I certify that I have read this dissertation and that, in my opinion, it is fully adequate in scope and quality as a dissertation for the degree of Doctor of Philosophy.

Martin Greven

Approved for the University Committee on Graduate Studies:

Abstract

The Angle Resolved Photoemission Spectroscopy (ARPES) recently emerged as a powerful tool for the study of highly correlated materials. This thesis describes the new generation of ARPES experiment, based on the third generation synchrotron radiation source and utilizing very high resolution electron energy and momentum analyzer. This new setup is used to study the physics of high temperature superconductors. New results on the Fermi surfaces, dispersions, scattering rate and superconducting gap in high temperature superconductors are presented.

Acknowledgements

I would like to thank my advisor, Zhi-Xun Shen, for his many suggestions and constant support during my years in graduate school. His insight led to the research in Bi2212 compound, which I originally considered too well researched and not very promising. However experience proved me wrong, and we were able to discover phonon energy scale in Bi2212, observe bilayer splitting and more. I would also like to acknowledge the help of Zahid Hussain, my Berkeley advisor, who helped me settle at the Lawrence Berkeley National Laboratory and whose support I could always count on. I am also very grateful to Xingjiang Zhou. Him and Scot Kellar were essential for making HERS endstation at the Advanced Light Source possible and were very helpful with experiments and data analysis. Alessandra Lanzara joined the group in a later part of my graduate term, but she became an essential part of Bi2212 research. She was the driving force in phonon interpretation of the data, and I enjoyed every moment of our collaboration. Over the years, all members of the Berkeley group became my friends, and it helped to make the long PhD experience enjoyable.

I would also like to acknowledge the support of Julia and my parents. Their presence helped me not to give up in times of trouble and stay focused.

I also wish to thank Er Dong Lu, Wan Li Wong, and Jonathan Denlinger. I want to acknowledge the support of the ALS stuff, in particular the work of Noel Kellog and Ed Wang, who helped make HERS endstation a functioning reality.

Finally, I'd like to acknowledge my many group mates from Stanford- Peter Armitage, Stuart Friedman, Anton Puchkov, Filip Ronning, Donglai Feng, Zhengyu

Wang, Anne Matsuura - whom I worked with extensively in my early years at Stanford, as well as other group members - Jeff Harris, Changyoung Kim, Donghui Lu, Kyle Shen, Paul White, Teppei Yoshida and Tchnag-Uh Nahm. And of course lots of thanks goes to Gloria Barnes and Marilyn Gordon, who saved us all from bureaucratic nightmares. Thank you all!

Stanford, California   Pavel Bogdanov

Contents

List of Figures

Chapter 1

Introduction

Solid state physics is arguably the most exciting and dynamic area of physics today. Indeed, the study of the conglomerates of zillions of atoms is directly related to our everyday life, and the complexities of the behavior of large particle ensembles are far from understood. Many prominent scientists suggest that the reductionist idea by the Ancient Greeks is dead, although it can still provide us with new information, e.g., from elementary particle experiments. In the world around us multitudes of particles are governed by emergent laws which can not be derived from elementary single-particle laws [1]. The action in solid state physics today is to discover and understand these laws.

There has been a lot of progress along this path. One of the most significant achievements was the development of band theory of metals. The theory is based on the solution for a single electron wave function in a periodic potential, and works perfectly for simple systems, such as Si or GaAs. However band theory remarkably breaks down for a whole class of materials with very unusual physical properties, which include high-temperature superconducting or colossal magneto-resistive ceramics. For example, band theory predicts that these materials are metals, but they exhibit insulating behavior.

This unusual behavior results from the strong correlations of electrons. Angle resolved photoelecton spectroscopy (ARPES) emerged as a leading tool for the research of strongly correlated systems, because it directly measures momentum-dependent electronic spectra near the Fermi level.

This thesis describes the development of a state-of-the-art high-resolution ARPES system at the beamline 10.0.1 at the Advanced Light Source (ALS) at the Lawrence Berkeley National Laboratory (LBNL). The system is then used to study several classes of the high temperature superconductors, including $(\mathrm{La}_{2-x-y}\mathrm{Nd}_y\mathrm{Sr}_x)\mathrm{CuO}_4$, $Bi_2Sr_2CaCu_2O_{8+\delta}$ and $Bi_2Sr_2CuO_{6+\delta}$.

Chapter 2

Angle Resolved Photoemission Spectroscopy (ARPES). Theory and experiment.

In this chapter we describe ARPES from theoretical and experimental points of view. Photoemission has a long history, and it is a very powerful and unique tool for the analysis of the electronic structure of solid state materials.

2.1 Historical Developments

The process in which light excites an electron from a solid, called photo-electron emission, was discovered by Hertz in 1887. In 1905 Einstein explained the systematics observed by Hertz by invoking quantization of light and the notion of the work function. He came up with the famous equation for maximum kinetic energy of the excited electrons $E_{kinetic} = \hbar\omega - W$, where $\hbar\omega$ is the photon energy and W is the work function. Energy and momentum of the photo-electron can provide information about the electronic structure of the solids. A photoemission spectroscopy experiment is designed to measure the energy and momentum of the photo-electron, which reveal information about the energy and momentum of the electron inside the solid, which in turn is the key to understand the physical properties of the solid. For the photon

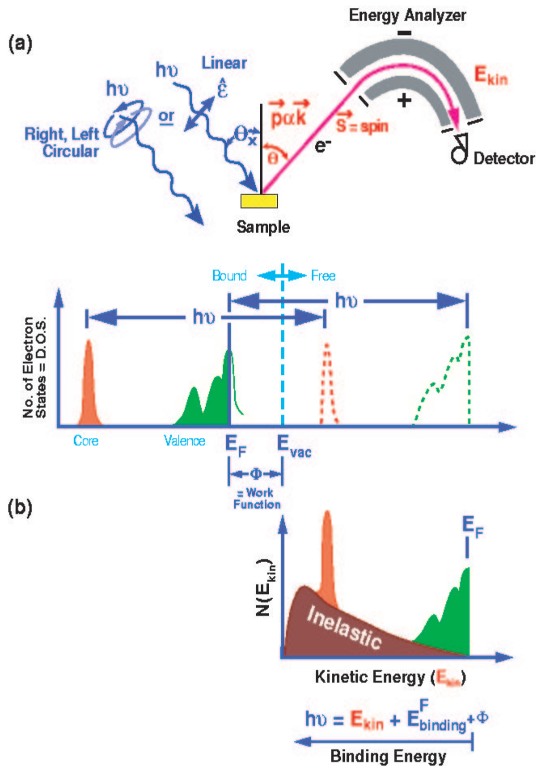

Figure 2.1: Panel a) shows a typical photo electron emission setup, with synchrotron light hitting the sample, and with a hemispherical analyzer scanning the electron energy. The bottom panel illustrates the ideal spectra for direct processes. Panel b) shows more realistic situation, where the resulting spectra is complicated by inelastically scattered electrons.

energies currently utilized in photoemission spectroscopy (15-200 eV) the photon momentum can be neglected ($k_p = E_p/c \ll k_e \approx \sqrt{E_p \cdot 2m_e}$). A typical photoemission spectroscopy experiment is done at a constant photon energy, while the energy of the emitted electrons is scanned and their intensity measured, see Fig. 2.1, although other experimental methods are also used [2].

For the simplest case of an individual atom (gas phase) such a scan will give the peaks at the energies equal to the photon energy minus the electron core level energies. In the case of a highly correlated material, the positions and shapes of the peaks can deviate from the simple situation, and their analysis can give more information on the underlying interactions in the material. States close to the Fermi level in the

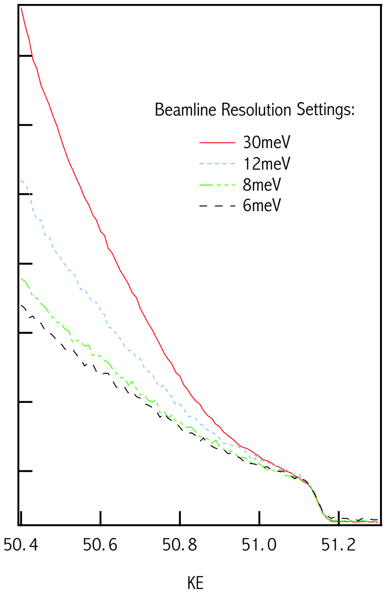

Figure 2.2: Figure shows near Fermi edge spectra of $La_1.48Nd_0.4Sr_0.12$ collected in analyzer angle mode with the integration of all spectra under identical conditions except for different photon flux (beamline resolution) settings.

interacting periodic system split and form bands. Then, resolving the momentum of emitted electrons gives information about band dispersions. Momentum-resolved (or angle-resolved) photoemission spectroscopy (ARPES) measures the intensity of the photo electrons at a certain energy and a certain momentum. In vacuum the value of the momentum is given by the value of energy via free electron relationship ($E = \frac{K^2}{2m}$), the direction of momentum is typically given by selecting a certain range of angles with the analyzer. The relationship between the measured electron momentum and energy and the corresponding electronic structure in the material is not straightforward, especially in highly correlated systems (see, e.g., Section 2.3).

2.2 How to do a correct experiment

In a real experiment at first we need to establish that our experimental output is indeed the correct representation of photo electron angle and energy distribution.

There are several factors that we usually have to control.

One factor is due to the fact that several beam harmonics come through from the synchrotron source. As a result, response to higher harmonics overlaps with the signal from the lowest most-intense harmonic, distorting data. The solution is that unless higher harmonics excite a core state to the kinetic energy in our experimental range, they create an approximately angle-independent background which is easy to subtract from the spectra.

Another factor is nonlinearity in the response of the electron analyzer. The problem is illustrated in Fig. 2.2 and Fig. 2.3. In each figure different curves were taken under identical conditions using beam of different intensity as controlled via beamline slits (nominal beamline resolution). The difference due to the change of photon flux is quite remarkable. The changes with the flux were reproducible. However, at sufficiently low flux levels the response of the analyzer becomes linear, so that at low beam intensities the curves become identical up to a factor. So for each material we have to establish the flux range where the analyzer is working in a linear response regime, and use it for data acquisition.

Another important experimental factor is correct energy and angle determination by the analyzer. Regular calibration of the instrument insures that the energy and angle results we read are real and reproducible. To calibrate energy we measure the Ar 3p peak position and set the measured energy equal to the known value for all lens modes and pass energies. We calibrate the angular mode by performing a grid experiment (see the last part of Chapter 2) and by adjusting lens tables to get the same angles at all kinetic energies for different pass energies.

Finally we have to address the issue of sensitivity in different analyzer channels. The difference in sensitivity is quite large, and even in a linear response mode can by a factor of 2 or more. However the Scienta analyzer installed at Beamline 10.0.1 has a stepping detection mode, in which each energy is measured by every channel, and the results for all channels are summed together. In this mode, the sensitivity problem is automatically taken care of. All of the data presented in this thesis were collected in this mode.

Having established that our experiment measures the photo-electron angle and

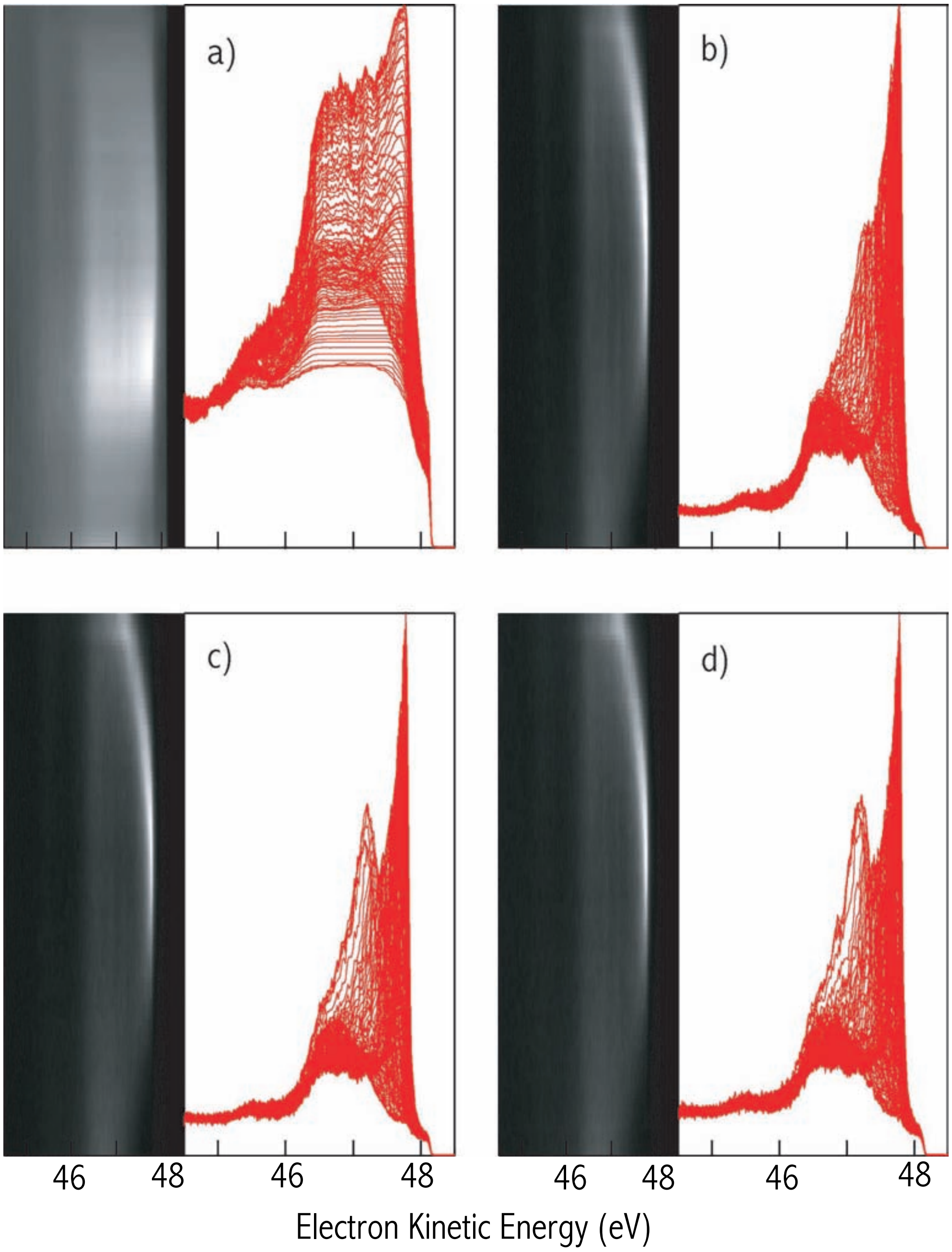

Figure 2.3: Panel a) shows angle-resolved near Fermi edge spectra from $LuNi_2B_2C$ with beamline resolution set to 15 meV. Panels b)-d) correspond to beamline resolution settings of 7 meV, 5 meV and 4 meV respectively.

energy distribution correctly, we have the hard task of interpreting the data. In a typical ARPES experiment it is justified to take the crystal surface plane component of the momentum of an emitted electron equal to the same component of the crystal momentum of an electron in the solid. For an emission angle α, $K_\alpha = \sqrt[2]{2mE_{kinetic}}cos(\alpha)$. In two-dimensional materials, the electronic structure can be described by the spectral function $A(K_\alpha, \omega)$. In the approximation that the emission process provides information on the unperturbed system, the photocurrent is equal to $I * A(k, \omega) * f(\omega) * M(k, \omega)^2$ [3]. Here I is a photon beam intensity, A is an electron spectral function, f is a fermi function, M is a photo excitation matrix element.

In reality, even in a two-dimensional system, the K component normal to the surface matters, because $K_\perp$ changes at the surface. In addition, only the electrons excited from 5 - 15 $\mathring{A}$ near the surface can escape without suffering scattering, for a photons in 20 - 800 eV energy range. The materials mostly studied on the HERS endstation, the high transition temperature superconductors (HTSC), are two-dimensional materials with unit cell lengths from 13 to 30 $\mathring{A}$. Because we are usually interested in bulk properties of the material, making sure that the data are representative of the bulk is very important.

Another issue is factoring out photo-excitation matrix element effects in the sample plane. As will be shown later, matrix elements play an important role in ARPES and can greatly change the spectra. Including matrix elements in the analysis is a complicated issue [4]. We discuss it in more detail in Chapter 5.

In practice, even the simple task of determining the Fermi surface from the correct experimental data is hard. At present, there are many methods routinely used to extract Fermi surface information from ARPES spectra: N(k) (integrated spectral weight in a large energy window) and N'(k) (derivative of the integrated spectral weight), symmetrization, dispersion interpolation, maximum spectral intensity at the Fermi level (Ef), temperature test [5]. Sometimes these methods give conflicting results, and then further research is needed to find the correct answer (e.g., see Chapter 5).

In the next section we describe the problems with determining quasiparticle dispersions and scattering rates from ARPES data.

2.3 How to analyze ARPES data (MDCs vs EDCs)

Recently [7], the term of momentum distributuion curves (MDC) was introduced for the analysis of ARPES spectra. With the new advances in experimental machinery, in particular with the appearance of the new Scienta analyzers with angle mode, unprecedented angular resolution has been achieved, making much more momentum data available. These data allow a new way of data analysis, sometimes superior to that of energy distribution curve (EDC), the traditional way to present data [7]. The results of this radical improvement in ARPES data quality have already been seen: great quality maps of Fermi surfaces and extremely clear identification of the superstructure in high temperature superconductor (high-Tc) $Bi_2Sr_2CaCu_2O_8$[8, 9, 10], phonon effects in electronic structure of various materials were directly observed for the first time [14, 13]. The latter result is based on the use of EDCs and MDCs to extract the dispersion and scattering rate of quasiparticles. For both MDCs and EDCs, the peak position as a function of momentum was taken to represent the quasiparticle dispersion. The peak width (velocity corrected for MDC) was taken to represent the scattering rate, or the imaginary part of the self-energy. Here we show, that even for the simple spectral function these quantities derived from EDC and MDC are different. In real experiments, matrix element effects further complicate the question.

For the simplest case, the Fermi liquid, the spectral function is given by

$$A(\vec{k},E) = \frac{1}{\pi}\frac{\beta \cdot E^2}{(E-E_{\vec{k}})^2 + (\beta \cdot E^2)^2}$$

Here, $E_{\vec{k}} = Z_{k_F} \cdot E^0_{\vec{k}}$, $\beta = Z_{k_F} \cdot \beta^0$. We are interested in extracting the self-energy $\Sigma(\vec{k},E) = \alpha E + i\beta^0 \cdot E^2$. Then $Z_{k_F} = \frac{1}{1-\alpha}$. We want to comment that the form of the Fermi liquid spectral function used here has several flaws from a theoretical standpoint. It is not causal at large E [15]. Furthermore, in theory, quasiparticles are defined for the case of $\Delta E \ll E$. In this limit $E^2 \ll E$, and both EDC and MDC results are the same. However, in practice the analysis is carried out far away from this limit, see, for example [7]. Also, as we point out later, the results are not

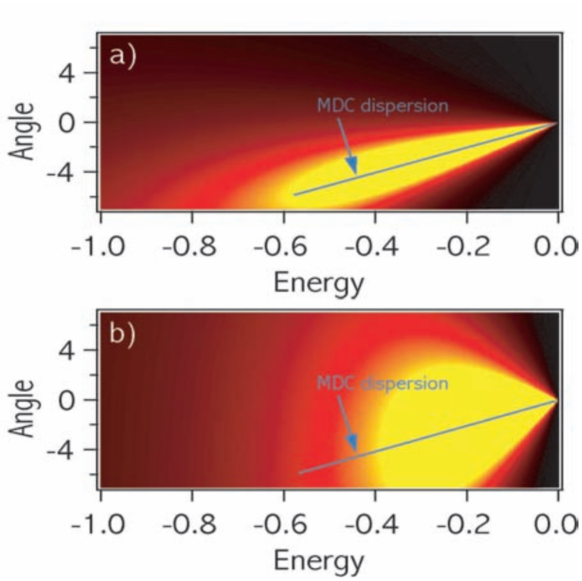

Figure 2.4: In this figure we plot simulated ARPES spectra for a Fermi liquid spectral function. Here β is equal to 1 in panel a) and to 7 in panel b). $E - 0.1K$ is the line corresponding to MDC derived dispersion. It is plotted in blue.

dependent on the particular form of self-energy.

Let's take the simplest case of linear dispersion, $E^0_k = ak + b$. Then, in the case of the MDC, the conventionally derived dispersion is determined by $\frac{\partial A(\vec{k},E)}{\partial k}$. This leads to the condition:

$$E = E_{\vec{k}} = Z_{k_F} ak + Z_{k_F} b$$

This represents the noninteracting dispersion weighted by the factor Z_{k_F}. In the case of the EDC, the dispersion is given by the condition $\frac{\partial A(\vec{k},E)}{\partial E}$. This transfers into:

$$E^2_{\vec{k}} = E E_{\vec{k}} + \beta^2 E^4$$

We immediately see that $E = E_{\vec{k}}$ is no longer a solution. This produces the difference between EDC and MDC dispersions that becomes very large when the β term is large.

There is also a big difference between MDC and EDC derived widths of the ARPES peaks. In the case of Fermi liquid, the MDC peak width is given by $\frac{Im(\Sigma(\vec{k},E))^2}{a^2}$. One of the most interesting quantities is $Im(\Sigma(\vec{k},E))$, which characterizes the quasiparticle

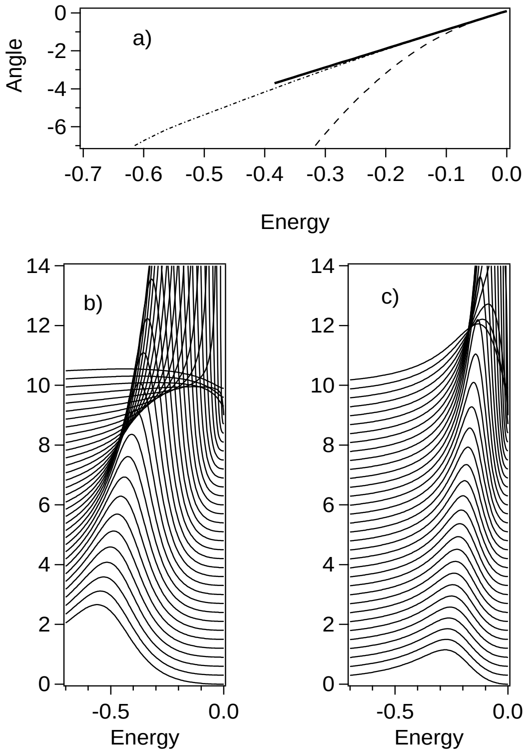

Figure 2.5: In panel a) solid line corresponds to MDC fits for β 1 and 7 cases. Broken line represents EDC fit for $\beta = 1$, dash represents EDC fit for $\beta = 7$. Panel b) shows EDCs for the angular interval $-7 < angle < 1$ for $\beta = 1$. Panel c) shows EDCs for the same angular interval as in b) for $\beta = 7$ case.

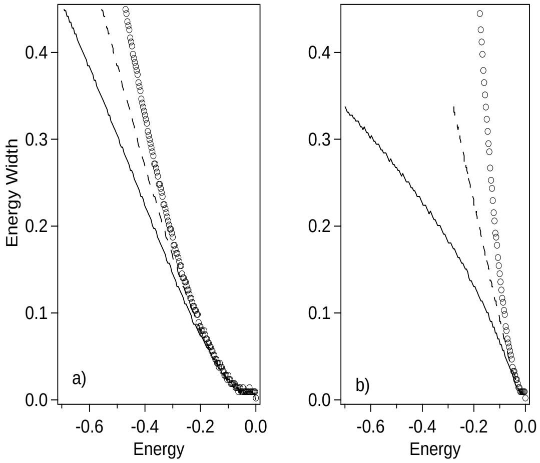

Figure 2.6: Open circles represent MDC width, solid line corresponds to EDC width using $E_{\vec{k}} = 0.1k$, dashed line corresponds to EDC width using EDC derived dispersion. Panel a) is for $\beta = 1$ case, panel b) is for $\beta = 7$

scattering rate τ. To make a transition from momentum to energy one can obtain $Z_{k_F} a$ from MDC dispersion, substitute a, and get

$$Z_{k_F} Im(\Sigma(\vec{k}, E))$$

for the energy width. More generally, for the self-energy of the form $\Sigma(\vec{k}, E) = \alpha E + iG(E)$, the MDC width gives $\frac{1}{1-\alpha} Im(\Sigma(\vec{k}, E))$. EDC derived widths, on the other hand, are not representative of the self-energy. There is no simple analytical expression for the EDC width even in the Fermi liquid case. Furthermore, the EDC derived dispersion is different from the theoretical E_k, and it is unclear which one of the two should be used to transfer momentum space locations of EDC slices into energy space. So far, the tradition in literature was to use the EDC dispersion to plot the EDC derived $\Delta E(E)$. In a more general case, when the self-energy depends on momentum as well, even the MDC derived dispersion no longer represents normalized non-interactive dispersion, and the width no longer gives the scattering rate.

In Figure 2.4 we plot simulated ARPES spectra, from the SES 200 analyser in angle mode, for a model Fermi liquid. In both panels $E_{\vec{k}} = 0.1k$. k is plotted as

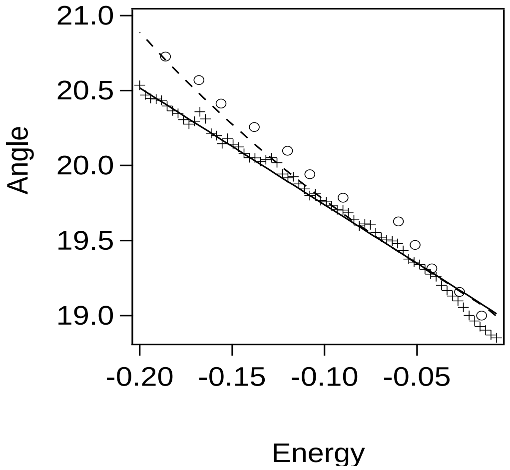

Figure 2.7: Comparison of MDC and EDC dispersion for the $\beta = 4$ Fermi liquid (solid and dashed lines respectively) and $Bi_2Sr_2CaCu_2O_8$ data for the optimally doped sample at $30K$ (crosses and open circles respectively).

angle to represent real Scienta spectra. The only difference between the panels is the β parameter. β is equal to 1 in panel a) and to 7 in panel b). However, the two cases appear to have different dispersion. The effect is further illustrated in Figure 2.5. In panel a) we plot peak positions of MDCs and EDCs for the two cases of Figure 2. Peak positions were determined as maximum intensity points of MDCs or EDCs. One can see, that while MDC dispersions for both cases are the same, EDC dispersions are different from MDC dispersions and from each other. Lorentzian or Gaussian fitting of MDCs or EDCs yields the same results. Panels b) and c) show EDCs for the cases in Figure 2.4.

The discrepancy is even larger for the peak widths. To compare EDC and MDC results, one has to plot data for both cases in the same reference frame. Since the EDC peak measures $\Delta E(k)$ and MDC measures $\Delta k(E)$, we use the theoretical dispersion of our model $E_{\vec{k}} = 0.1k$ to plot both results as $\Delta E(E)$. For the EDC widths we also use the EDC derived dispersion. The MDC width is plotted as open circles, the EDC width using $E_{\vec{k}} = 0.1k$, is plotted as a solid line, and the EDC width using the EDC derived dispersion is plotted with dashed line. In panel a) of Fig. 2.6 we show data for $\beta = 1$, and in panel b) for $\beta = 7$. Similar to the dispersions, EDC and MDC

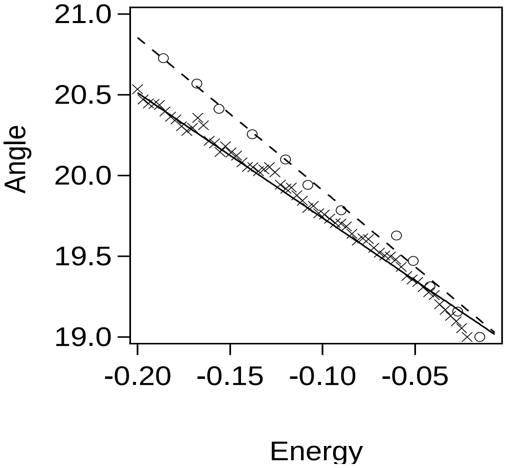

Figure 2.8: Comparison of MDC and EDC dispersion for the $\beta = .7$ marginal Fermi liquid (solid and dashed lines respectively) and $Bi_2Sr_2CaCu_2O_8$ data for the optimally doped sample at $30K$ (crosses and open circles respectively).

widths are drastically different. We find, that the EDC width, using the EDC derived dispersion, is closer to the MDC width, but the difference is still very large.

Since even the simplest Fermi liquid model produces a difference between EDC and MDC, it is interesting to see what happens in the case of real compounds. We have performed ARPES studies of $Bi_2Sr_2CaCu_2O_8$ along $\Gamma - Y$ high symmetry direction. Angle-resolved photoemission data have been recorded at beamline 10.0.1.1 of the Advanced Light Source utilizing a photon energy of $33eV$. The momentum resolution was ± 0.1 degrees. The energy resolution was $14meV$. The vacuum during the measurement was better than $4 \cdot 10^{-11} Torr$. The slightly overdoped $Bi_2Sr_2CaCu_2O_8$ sample ($T_c = 91K$) was grown using the floating-zone method. The measurement was done at $30K$. In Figure 2.7 we plot the EDC and MDC determined dispersion for this sample along with the Fermi-liquid model results with $\beta = 4$ and $E_k = -0.129 \cdot (k - 18.962)$. The model was chosen to fit the high-energy part of the MDC dispersion and to converge with the EDC dispersion at high binding energy. Fitting MDCs and EDCs in the full energy range is complicated, since as reported earlier, the real dispersion in $Bi_2Sr_2CaCu_2O_8$ exhibits a kink at a binding energy of $50meV$ [16]. While the high-energy MDC-derived dispersion fits well with our model, the EDC is different from the calculation, although its deviation from the MDC reaches about the same value at $200meV$ binding energy. We have to point out, that the EDC analysis is tricky, since there is a large background effect.

Another model often discussed in the case of $Bi_2Sr_2CaCu_2O_8$ is the marginal Fermi liquid [17]. In the case of marginal Fermi liquid, the imaginary part of the self-energy is proportional to E at low temperatures. In the marginal Fermi liquid case, MDC and EDC dispersions are also different. However, in this case the EDC dispersion remains proportional to the MDC dispersion E_k:

$$E = \frac{E_k}{\sqrt{1+\beta^2}}$$

Here β is a coefficient similar to that of the regular Fermi liquid. In Figure 2.8 we plot the marginal Fermi liquid fit to the data. Again, we focus on the high energy part. Now, the EDC fits look much better. Again, we took $E_k = -0.129 \cdot (k - 18.962)$. We determined β to be around 0.7 for the best fit. However, to get a better estimate of the parameter β one must have a theoretical model for E_k that includes the kink and low energy part of the dispersion.

In conclusion, we have shown, that even in the simplest case of the Fermi liquid different methods of dispersion and scattering rate analysis give different results. Momentum Distribution Curve analysis of the dispersion and scattering rate in the case of momentum-independent analysis results in a renormalized dispersion and renormalized imaginary part of self-energy. Energy distribution curve analysis always produces something different. We utilize this knowledge in other parts of this thesis.

Chapter 3

HERS endstation at Beamline 10.0.0.1 of the Advanced Light Source

In this chapter the description of the High Energy Resolution Spectroscopy (HERS) endstation is given. This endstation was designed to study highly correlated-materials, including the high temperature superconductors, with state-of-the-art resolution. As many feel that the most useful insight to understanding these fascinating materials will come from angle-resolved photoemission data, the 10-fold increase in momentum resolution afforded by the HERS endstation will likely be very valuable.

3.1 Beamline

The HERS endstation is located on beamline 10.0.0.1 of the Advanced Light Source (ALS). ALS is the world's brightest source of ultraviolet and soft x-ray beams, -and the world's first third-generation synchrotron light source in this energy range. Beamline 10.0.1 utilizes ALS capabilities and provides an intense beam of radiation in the photon energy range of 20-350 eV with very high resolution. The beamline consists of an undulator, pre-focusing optics, a spherical grating monochromator (SGM) and refocusing and deflecting optics. The light from the beamline can be directed down one of three end-station branchlines by moving the horizontal deflecting optics on

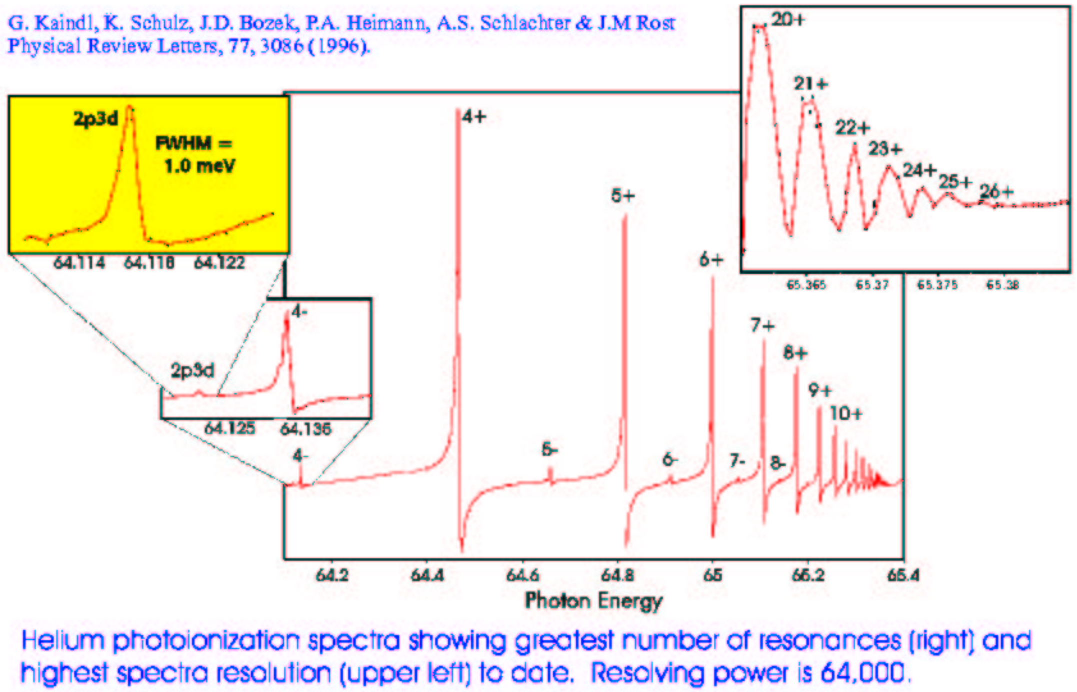

Figure 3.1: Beamline 10.0.1 resolution measured with He gas.

a translation stage. With automated mirror motion and utilizing beam position monitors, only minutes are required to change between the different end-stations. The beamline characteristics are summarized in Figures 3.1 and 3.2, which show beamline resolution and flux.

3.2 Endstation

We have designed the HERS endstation to use the unique characteristics of beamline 10.0.1 by bringing together a combination of high-performance components. The general view of the system without the manipulator is presented in Figure 3.3. The most important component of the endstation is the Scienta SES200 electron energy analyzer. The analyzer is discussed in detail in the next section.

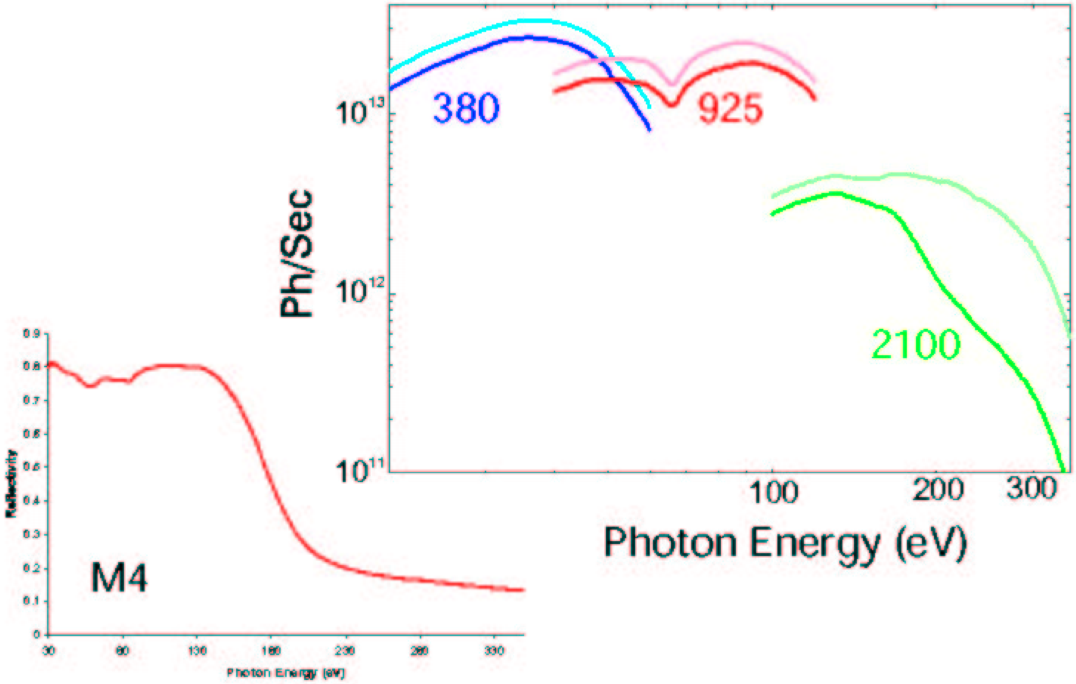

Figure 3.2: Beamline 10.0.1 flux as a function of grating and photon energy.

An important feature of the endstation is the ability to rotate the analyzer about the incoming beam. The main chamber, where the electron energy analyzer is mounted, rotates 120^o about the incoming beam. Because the radiation from the storage ring is polarized in the plane of the ring, this rotation allows one to vary the polarization incident on the target from s to p while maintaining a constant emission angle from the sample. Two differentially pumped rotary seals mounted to the chamber allow the rotation while maintaining good vacuum. The chamber base pressure is less than $4 \cdot 10^{-11}$ $Torr$, and there is no appreciable pressure change when the analyzer is rotated.

Very important to the success of the HERS endstation is the sample manipulator. The manipulator consists of two important parts. The first is the x, y, z stage. For this part we made use of existing technology and purchased a commercial mill table. The mill, while quite large, works very well in this application, allowing very precise

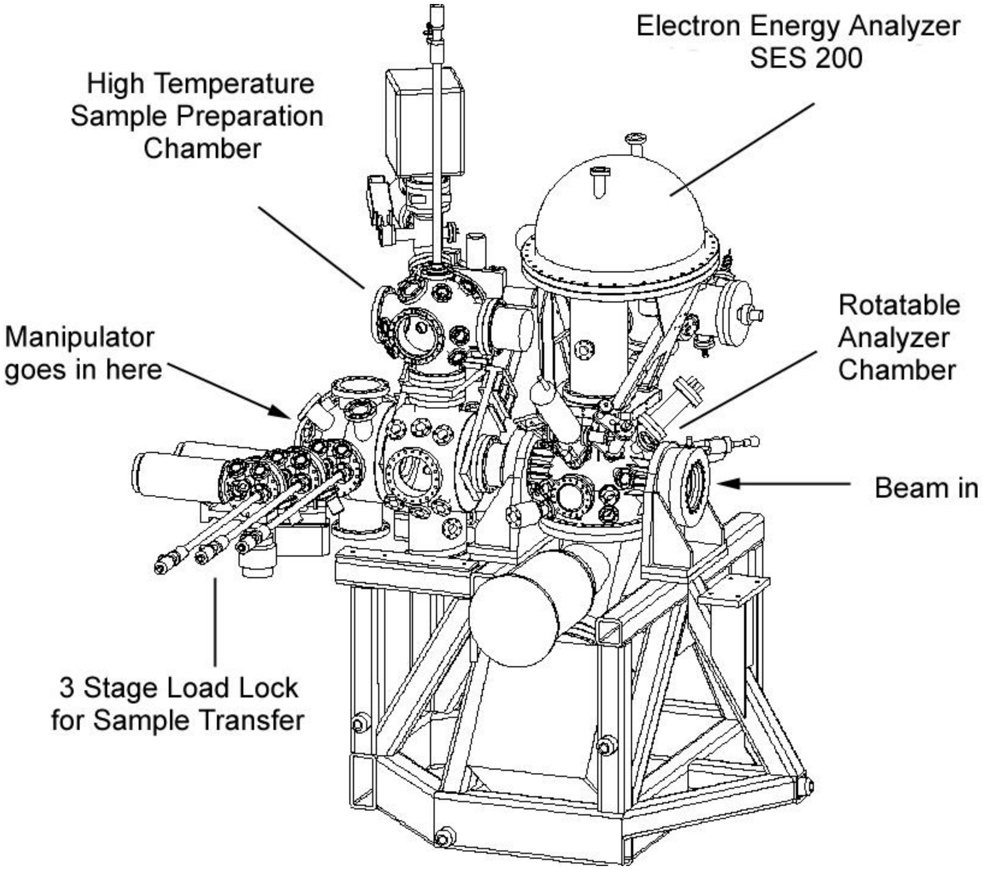

Figure 3.3: HERS endstation.

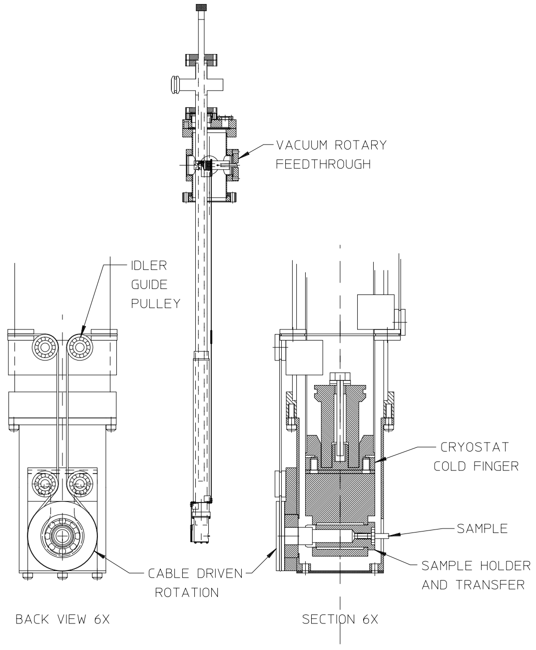

Figure 3.4: HERS manipulator schematics.

sample movements of 0.001" over the 37" of travel from the sample prep chamber to the analysis position in the analyzer chamber. The second part is the cryostat, shown in Figure 3.4. The sample polar rotation is accomplished by a differentially pumped rotary feedthrough to which the liquid helium cooled cryostat is mounted. The azimuthal rotation is accomplished via a cable driven through a rotary feedthrough. The rotational accuracy for both axes is 0.5^o. With the LHe cooled cryostat the sample temperature can be controlled from $10K$ to $450K$ with better than one degree accuracy.

Because many samples cannot withstand the high temperature bake-out necessary for UHV work, we developed an elaborate yet user-friendly load-lock system which allows one to move a fresh sample from atmosphere onto the manipulator in the main chamber, where the pressure is less than $4 \cdot 10^{-11}\ Torr$, in less than 2 hours without baking, see Figure 3.5. The multi-stage load lock has parking spots for 39 different samples. A sample is transferred into the first stage from air by using hand-held collat sample holder. The stage is equipped with a turbo pump and a titanium sublimation

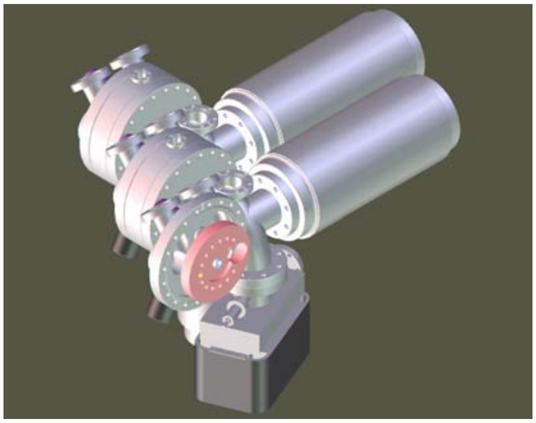

Figure 3.5: Load lock schematics.

pump. Due to the small volume of the stage, the pressure goes to $5 \cdot 10^{-8}$ $Torr$ in half an hour. The second stage is separated from the first one via a UHV lock. The second stage is pumped with an ion pump and a TSP. The lowest pressure achievable is $2 \cdot 10^{-10}$ $Torr$. The pressure in the stage recovers in 40 minutes after the sample is transferred from the first stage. Then, the sample is transferred to the main chamber via a third stage. All stages are connected with UHV valves.

The endstation is equipped with standard surface science preparation tools. Three horizontal chambers house cleaver, ion sputtering gun, and LEED spectrometer. For samples that cannot be cleaved and must be prepared in vacuum, we designed a special chamber capable of high-temperature sample treatment. The chamber is equipped with evaporators, ion sputtering guns, gas dosers, etc.. It is the uppermost chamber of the Figure 3.3.

3.3 Analyzer

The electron energy analyzer is a commercial unit purchased from Gammadata-Scienta AB. As Figs. 3.6 and 3.7 demonstrate, the energy resolution from this instrument is excellent. In Fig. 3.6 we display the photoemission spectra of the Fermi-edge function from a polycrystalline gold sample at temperature of $10K$. With thermal

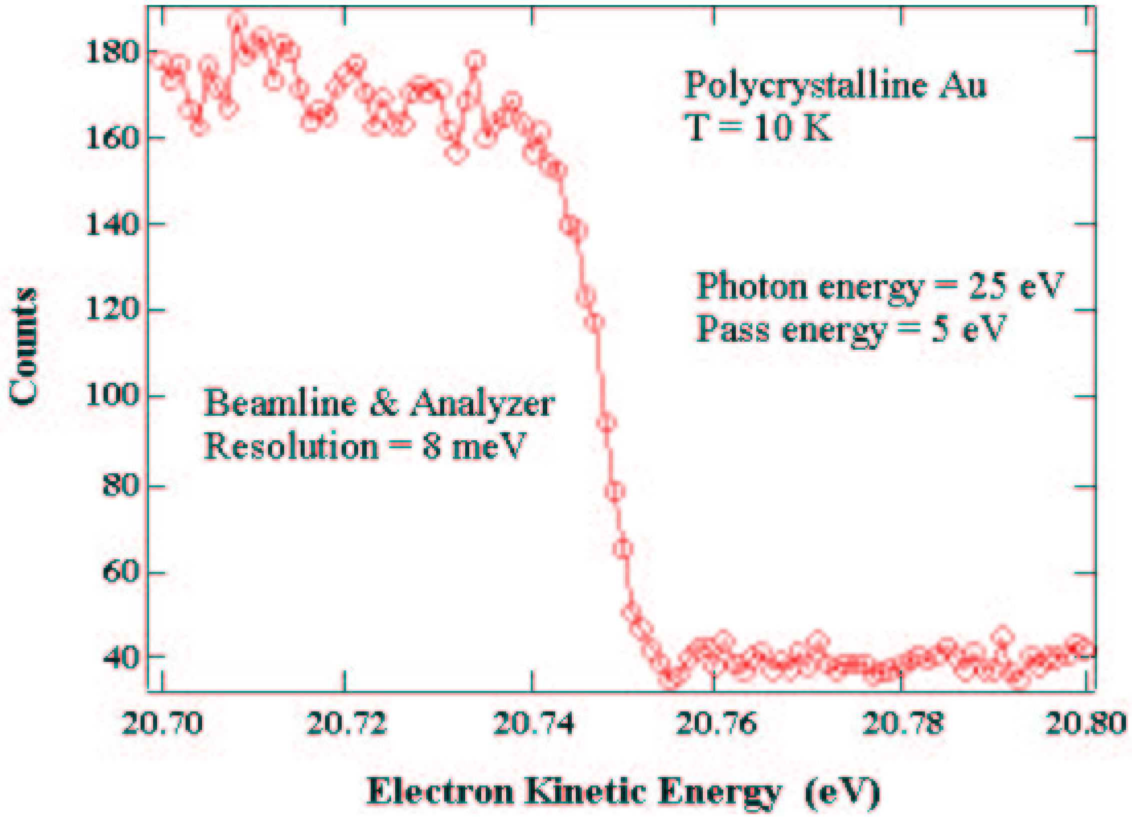

Figure 3.6: The photoemission spectra of the Fermi edge from a polycrystalline gold at 10 K. With thermal broadening of 4.4*k_BT or 4 meV at 10 K, the combined analyzer and beamline energy resolution is 8 meV.

broadening of $4.4 \cdot k_B \cdot T$ or 4 meV at $10K$, the combined analyzer and beamline energy resolution is 8 meV, because the data can be fit by 4 meV Fermi edge convolved with 8 meV Gaussian to represent combined resolution. Fig. 3.7 is the photoemission spectrum of the Ar $3p\frac{3}{2}$ core level taken using $25eV$ synchrotron radiation from beamline 10.0.1.1. The full width at half maximum of the peak is $8meV$. Taking into account the natural line width and Doppler broadening of the Ar $3p$ line, the total contribution from the beamline and the analyzer is $5meV$.

In addition to the excellent energy resolution, the analyzer also demonstrated very good angular resolution. When operating in the angular mode, the analyzer lens system focus changes, so that the lens diffraction plane is at the entrance slit to the

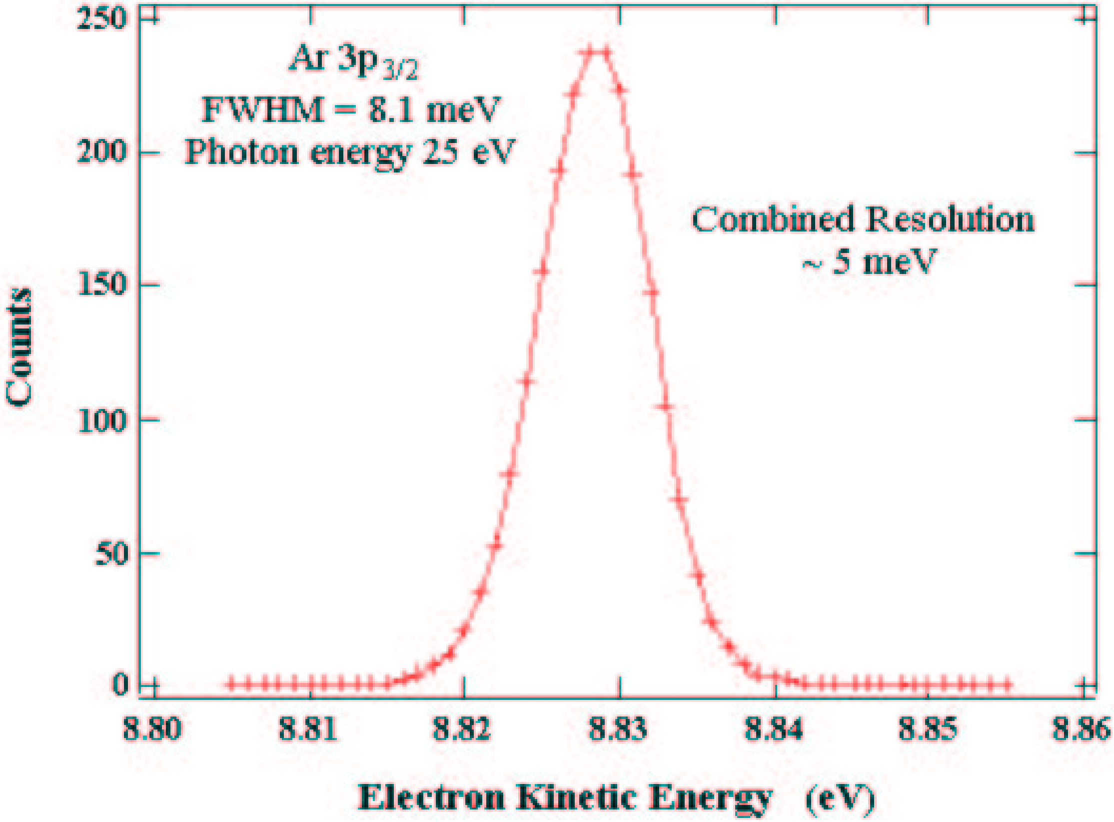

Figure 3.7: The photoemission spectrum of the Ar $3p\frac{3}{2}$ core level taken using $25eV$ synchrotron radiation from beamline 10.0.1.1 is shown. The full width at half maximum of the peak is $8meV$. Taking into account the natural line width and Doppler broadening of the $Ar3p$ line, the total contribution from the beamline and the analyzer is $3meV$.

analyzer. This allows the two-dimensional focusing of the hemispheres to maintain the angle with which the electrons leave the sample. Using proper image-capturing equipment we can at one time collect and energy analyze electrons leaving the sample within a cone of $\pm7^o$ with 0.2^o resolution. This angular resolution constitutes an order of magnitude increase in resolution over previous equipment. In Fig. 3.8, we show the results of the angular mode tests. The electron source is a thin wire illuminated by 55 eV photons from the synchrotron beam. This wire is parallel to a slit array positioned 25 mm above it. The slits are 100 μm wide and spaced 500 μm center to center, which gives a spacing between slits of 1.3°. This spectrum was collected using

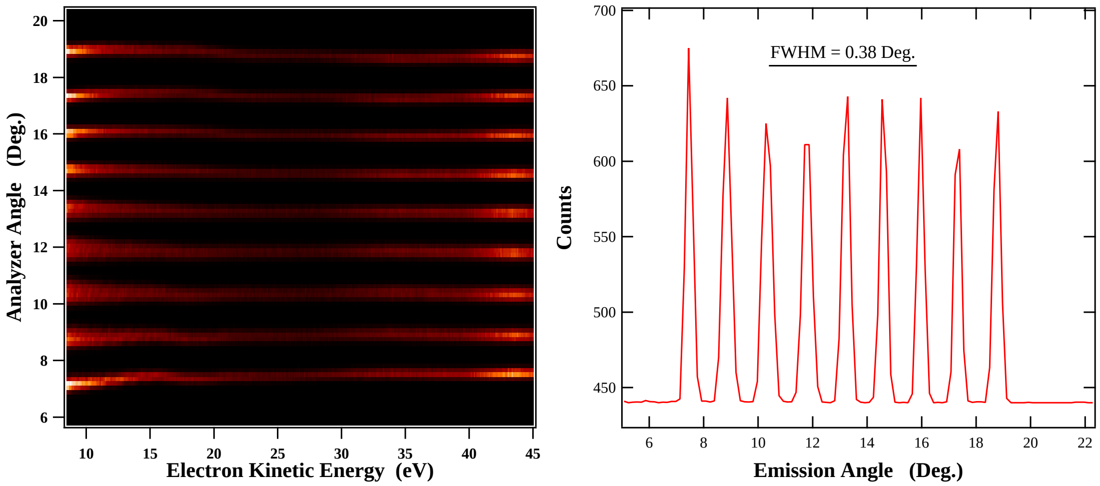

Figure 3.8: Angle resolution tests.

5 eV pass energy. As can be see in the Figure, the angular resolution is excellent, even at kinetic energies approaching the pass energy. Fitting a Gaussian to the individual peaks gives an angular resolution of $\pm 0.15^o$ when one accounts for the widths of the source and the slit. While the intensity is uneven over several channels, we believe this is an artifact due to inhomogeneous graphite coating on the slit array.

Chapter 4

High Temperature Supercoductors and ARPES

In this chapter we give a general description of the high temperature superconductors and introduce the issues that ARPES can address.

4.1 History of the problem

In 1911, H. K. Onnes discovered that the resistance of Hg abruptly dropped to zero upon lowering temperature. This phenomenon became known as superconductivity. Later, another signature of superconductivity was found - a complete screening of magnetic field by a superconductor, known as Meissner effect. Resistive and magnetic properties of supeconductors immediately drew a lot of attention from scientists because of the great promise for applications. By trial and error new compounds with ever higher superconducting transition temperatures (T_C) were found (see Fig. 4.1), but until 1986, the highest achievable T_C was barely above 20K.

The understanding of the superconductivity came almost half a century after the original discovery with the theory by Bardeen, Cooper and Schrieffer (BCS) in 1957 [18]. The theory was very successful in providing a microscopic mechanism of superconductivity. BCS showed that the coupling of electrons due to the exchange of phonons leads to a new superconducting ground state and a gapped excitation spectrum. The theory, typically formulated in the adiabatic weak-coupling limit, put

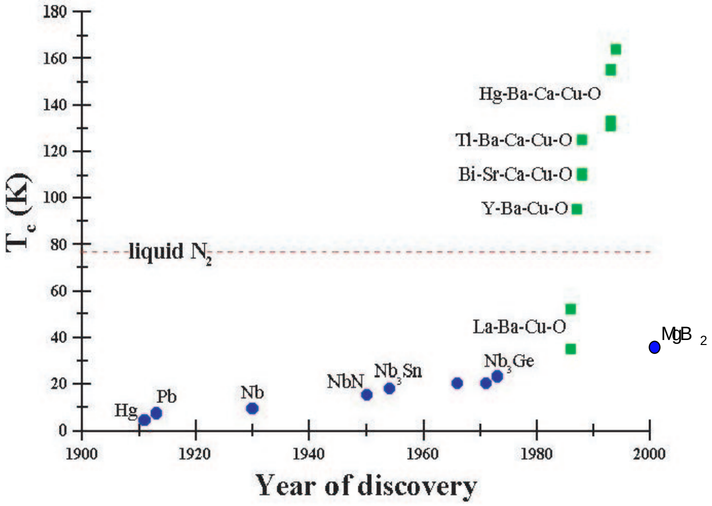

Figure 4.1: In this figure historical progress in record-breaking $T_C s$ is recorded. One can clearly see the high temperature superconductors standing out.

a limit on T_C of around 25K [19].

In 1986, Bednorz and Muller discovered superconductivity at 27K in $La_{2-x}Ba_xCuO_4$. This discovery shook the field. First, this compound was a very poor metal above T_C. Second, the T_C was very high. Third, the undoped compound (x=0) was an insulator, while band theory predicted it to be a metal. Finally, unlike earlier record keepers, it was not an elemental or a binary compound, but a very complex layered system.

4.2 High Temperature Superconductivity

As Figure 4.1 shows, following the discovery by Bednorz and Muller in 1986, many new complex materials with ever higher T_C were found. All of them are referred to as high temperature superconductors (HTSC). Early attempts to describe HTSC in terms of BCS theory were unsuccessful [20]. It was believed that the maximum T_C in BCS theory is naturally limited, as the increase in electron-phonon coupling strength (necessary for higher T_C) will at some point lead to an electron localization through

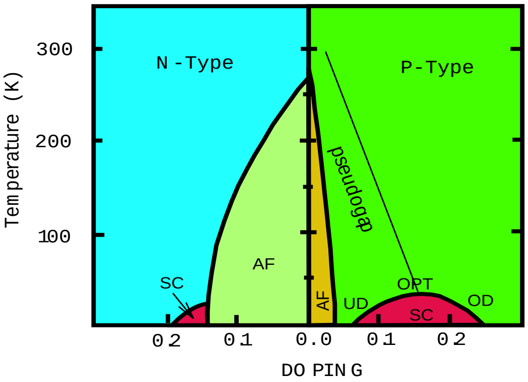

Figure 4.2: This figure shows generic doping phase diagram of HTSCs. Values for the p-type are those from $La_{2-x}Sr_xCuO_4$ system, and for the n-type from $Nd_{2-x}Ce_xCuO_4$ system.

polaron formation, decreased Coulomb screening, and suppression of transport. Further, direct checks of the electron-phonon coupling strength through isotope effect measurements in HTSC showed negligible changes in T_C upon isotope substitution in optimally doped materials [21]. Also, the discovered d-wave form of superconducting gap in HTSC was apparently inconsistent with almost isotropic electron-phonon coupling. Although ways to explain all of the above in terms of particular electron-phonon coupling models were later suggested, the research focus shifted to studying the effects of electron correlations as the main reason for HTSC properties.

This approach has a strong foundation in a generic phase diagram of HTSC, as shown in Fig. 4.2. The properties of HTSC change with doping. At zero doping, all of the HTSC are antiferromagnetic insulators. This insulating behavior contradicts band structure predictions of a metal, and can only be explained by strong electron interactions. By changing doping, the antiferromagnetic order is quickly destroyed and soon superconductivity sets in. The HTSC can be doped by holes (p-type) or by electrons (n-type). P-type HTSCs are more numerous and show the highest T_Cs. In this thesis I will report results exclusively from p-type superconductors.

In the superconducting doping range it is conventional to characterize p-type compounds as underdoped (UD), optimally doped (OPT) and overdoped (OD). A compound is optimally doped if its T_C is the highest T_C achievable (typically at $x = 0.15$

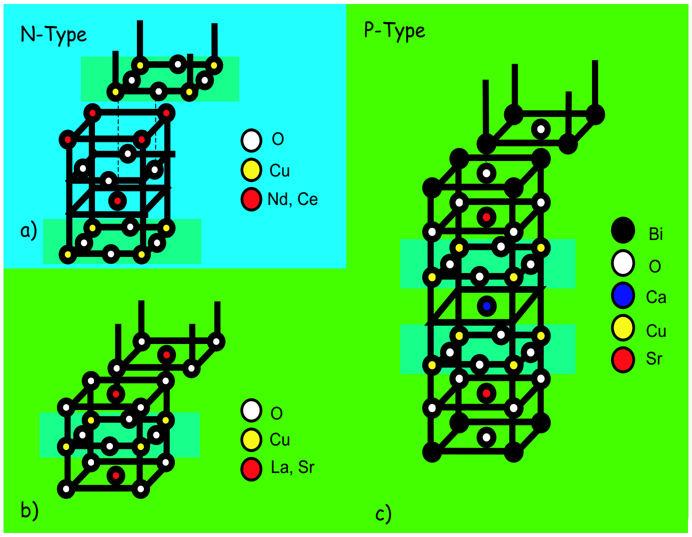

Figure 4.3: Panel a) shows the crystal structure of the n-type material - $Nd_{2-x}Ce_xCuO_4$. Panels b) and c) show p-type $La_{2-x}Sr_xCuO_4$ and $Bi_2Sr_2CaCu_2O_8$. CuO_2 layers are highlighted.

holes per Cu), underdoped if its doping is less than optimal, or overdoped if its doping level is more than optimal. The necessity to distinguish these three different doping ranges comes from the different normal state properties displayed by these materials in each doping range. For example, OD samples are good metals in the normal state. UD samples show a suppression of the electron density near the Fermi level known as pseudogap. This pseudogap was observed by many experimental techniques, such as NMR, transport, tunneling spectroscopy, ARPES, and optical reflectivity (see the review article [22]). The pseudogap opening temperature decreases with doping, and approaches T_C at optimal doping.

The similarity in properties of HTSC comes from the similarity in the crystal structure. All of the HTSCs are composed of 3 elements or more. All of the HTSC are layered and share the same building block - CuO_2 plane. Fig. 4.3 shows crystal structures of some of the HTSCs. In panel a) we plot the crystal structure of the n-type material $Nd_{2-x}Ce_xCuO_4$. In panels b) and c) we show p-type $La_{2-x}Sr_xCuO_4$ and $Bi_2Sr_2CaCu_2O_8$. All of these compounds share the same CuO_2 layer, highlighted in grey. Materials in panels a) and b) are called single layer compounds, while material

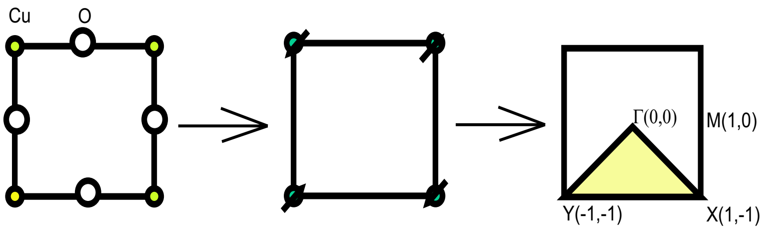

Figure 4.4: This figure shows the CuO_2 plane, the corresponding square lattice, and the Brillouin zone. Notation in the Brillouin zone is that for $Bi_2Sr_2CaCu_2O_8$.

in c) is a double-layer compound, since it has two neighboring layers in a single building block. In this thesis we study materials in panels b) and c).

Since the CuO_2 planes are common to all HTSC families, it is natural to approach the explanation of HTSC from the description of the CuO_2 plane. Band calculations show that the Cu $d_{x^2-y^2}$ orbital and the O p_x and p_y orbitals are the highest energy occupied orbitals for the CuO_2 plane [23, 20]. At zero doping there is only one electron per each CuO_2 unit cell. In this case, band structure predicts metallic behavior with the conduction band half filled. From the phase diagram in Fig. 4.2, we see that HTSCs at zero doping are insulators. The reason why band structure fails is that in considering the motion of one electron it treats the rest of electrons as a uniform potential. However, in highly correlated systems, this potential changes dramatically depending on the position of the electron. In the case of the CuO_2 plane, Cu 3d orditals are highly localized, and having two electrons in the same Cu orbital costs a lot of Coulomb energy U. In fact the kinetic energy gain associated with electron hopping is less than the energy loss due to Coulomb repulsion. As a result, transport at zero doping is suppressed (Mott limit). On the other hand, in calculating the ground state energy, virtual hopping is allowed. As a result, virtual hopping leads to the observed antiferromagnetism, because electrons have to have opposite spins to reside at the same orbital to satisfy the Pauli principle.

Zhang and Rice showed that upon doping CuO_2 a new low-energy state emerges [24]. This state is the combination of a hole residing on a Cu atom and a doped hole on hybridized Cu and O orbitals. This Zhang-Rice singlet state leads to an effective one-band picture. So, for the low-energy properties, it is possible to reduce the CuO_2

plane picture to a square lattice with hydrogen-like atoms in the corners, see Fig. 4.4. Of course, this one-band approach is an approximation. It fails in several important ways - for example, it predicts symmetry between p-type and n-type superconductors, which is not the case. However, due to its simplicity it is often used as a starting point to discuss the physics of the CuO plane with the correlation effects already incorporated.

4.3 ARPES study of High Temperature Superconductivity - Outline of this thesis

As explained in Chapter 1, ARPES gives information about the electronic structure in momentum space. From the crystal structure we determine that the Brillouin zone of the CuO_2 plane is a square. The sides of the zone are parallel to the Cu-O bond directions. In Fig. 4.4 we show the Brillouin zone notation used for $Bi_2Sr_2CaCu_2O_8$. From the square lattice picture described above we expect to observe one low-energy band for single layer compounds and two bands for double layer compounds (if the layers interact strongly enough).

Because the ARPES signal is proportional to the electronic spectral function, we can determine the band width, dispersions, Fermi surface size and shape, energy gap size and shape, etc.. We need this important information to understand high- T_C superconductors.

One of the fundamental issues in understanding the physics of high temperature superconduting cuprates is the transition from an insulator to a good metal with doping x. A good metal found on the overdoped ($x > 0.15$) side of the phase diagram has its Fermi surface well described by band structure and has more conventional properties, while the material at $x = 0$ is a Mott insulator, despite the band theory prediction of it being a metal. If one starts from the strong correlation theories that work well for the insulating state, one gets the total number of conducting holes equal to x at doping x . On the other hand, in a good band structure metal, the total number of conducting holes should be $1 + x$. One of the ways ARPES can help us in understanding the doping dependence of the number of carriers is by studying the Fermi surface. According to the Luttinger theorem, the Fermi surface area should be proportional to the total number of carriers. We present the results of our Fermi surface studies in Chapters 5 and 6.

Another important issue in understanding the microscopic properties of HTSC is the identification of the nature of coupling between electrons. In conventional superconductors two key experiments, the isotope effect and tunneling spectroscopy measurements (tunneling spectroscopy is very similar to ARPES, albeit angle-integrated), showed that the coupling is due to phonons. So far, there is no direct evidence for a strong coupling between electrons and phonons in HTSCs. The coupling to phonons has a characteristic signature in the electronic dispersion, which can be measured by ARPES. In Chapter 7, we present our results on the dispersions in $Bi_2Sr_2CaCu_2O_8$, and discuss different coupling scenarios.

Another interesting issue is the presence of remnant antiferromagnetic scattering in HTSC at high doping levels. Many strong correlation scenarios of high temperature superconductivity predict anisotropic coupling related to spin scattering centered at (π, π), that connects $(\pi, 0)$ to $(0, \pi)$ points in the Brillouin zone. We can look for the signature of this anisotropy in the momentum dependence of the quasiparticle widths, as studied in Chapter 8.

Predictions about the superconducting gap are important results in any theory of superconductivity. In the case of HTSC with d-wave like superconducting gap, ARPES is the only tool able to provide important details on the momentum dependence of the gap. Recent improvements in angular and energy resolution allowed us, for the first time, to resolve the states above the Fermi level due to the opening of the gap. In Chapter 9, we discuss these new results and show the momentum dependence of the superconducting gap near the gap node.

In Chapter 10, we propose more research that can shed light on the HTSC physics.

In Appendix A, we present preliminary results of the gap measurements on the bilayer-resolved $Bi_2Sr_2CaCu_2O_8$.

Chapter 5

Fermi Surface Studies: The Bi2212 system

High resolution angle resolved photoemission data from Pb doped $Bi_2Sr_2CaCu_2O_{8+\delta}$ (Bi2212) with suppressed superstructure is presented. Data were taken with improved resolution and very high momentum space sampling at various photon energies. Several complementary methods for determining the Fermi surface are applied, and all yield the same result. The photon energy dependence of a Fermi surface as well as the existence of two Fermi surface pieces provide a unifying picture of the Fermi surface in Bi2212.

5.1 Introduction

The Fermi surface plays an important role in developing an understanding of the physics of a material. Among other things, its shape and size determine the type and number of charge carriers in the material, as well as the charge and spin dynamics. For example, in the context of the Fermi liquid approach to the high temperature superconductors (HTSCs), the Fermi surface topology is related to the commensurate or incommensurate nature of neutron data [66]. Furthermore, detailed knowledge of the Fermi surface is essential to determine the superconducting gap size and symmetry in the superconducting state.

Angle resolved photoemission spectroscopy (ARPES) is a unique tool to probe the

Fermi surface of the HTSCs. Over the last decade, the HTSC system most extensively investigated by ARPES has been Bi2212 [67, 68, 69, 70, 71, 72, 73, 74, 75]. However, the existence of a superstructure in the BiO layer and of shadow bands has made the Fermi surface determination in this compound complicated, especially around the $M(\pi, 0)$ point, where 2 main bands, 4 superstructure bands, and 2 shadow bands cross the Fermi level. For several years, there was a general agreement on the existence of a hole-like Fermi surface centered around $Y(\pi, \pi)$, mainly based on ARPES experiments performed at $22eV$ photon energy [69, 70, 71, 72, 73, 74, 75]. This hole-like Fermi surface picture was believed to apply over the entire doping range studied by ARPES (from underdoped samples with $Tc \approx 15K$ to overdoped samples with $Tc \approx 68K$). Recently, however, experiments utilizing $33eV$ photon energy suggested an electron-like Fermi surface centered around the Γ point [10, 76, 77]. It has also been suggested that there are two kinds of Fermi surface features, a hole-like piece as seen in 22 eV data and an electron-like piece as seen at 33 eV data [77]. The main difference between the electron-like and hole-like Fermi surfaces resides near the $(\pi, 0)$ region, the former closed around the Γ point, and the latter open. Other groups disputed electron-like Fermi surface reports, explaining the observed results by the interplay of matrix element effects with BiO layer superstructure and shadowbands [8, 9, 78, 79]. It is of great importance to resolve the uncertainty in the Fermi surface of Bi2212 - the compound extensively studied and source of many significant results.

Because the main discrepancy originates in the $(\pi, 0)$ region, where the superstructure effect of the BiO layer is strongest, a definitive resolution of this issue can be found by studying the Pb-doped Bi2212 system. In this compound Pb is doped into the BiO plane disrupting the BiO plane modulation and removing the superstructure complication near the $(\pi, 0)$ region [8, 79, 80].

In this chapter we present results of Fermi surface mapping of Pb-doped Bi2212 with high energy resolution and very high k space sampling. We used various photon energies and different methods to determine the Fermi surface, unambiguously demonstrating the existence of two pieces of Fermi surfaces, whose relative intensities in ARPES data depend strongly on photon energy. This result contradicts earlier reports of a single universal hole-like Fermi surface in this compound [8, 73, 79]. On

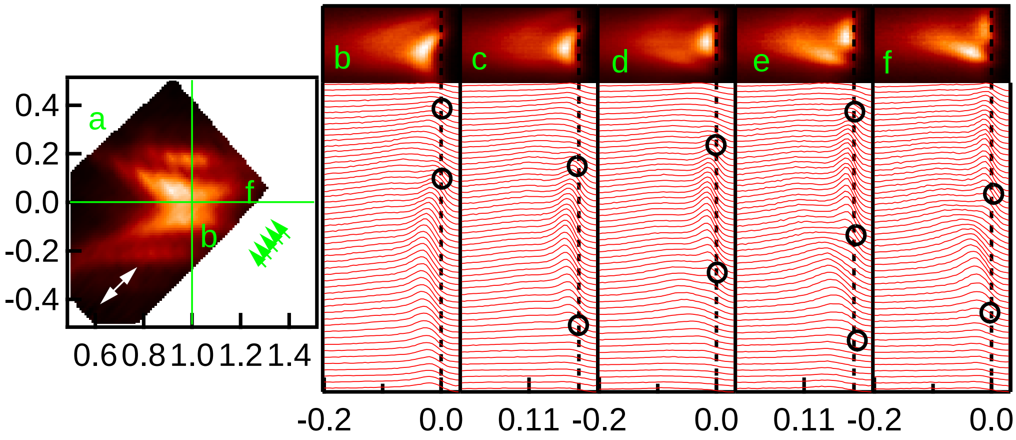

Figure 5.1: Panel a) shows the spectral intensity at the Fermi level for data collected with 22 eV photons. White arrow shows the light polarization. Panels b) - f) show EDCs along the cuts indicated in panel a).

the other hand our data provide a unifying foundation for understanding the controversies about the Fermi surface of this important superconductor, as different reports stress different aspects of the global Fermi surface features.

5.2 Experiment

ARPES data have been recorded at beamline 10.0.1.1 of the Advanced Light Source utilizing $55, 44, 33, 27$ and $22\ eV$ photon energy in $4 \cdot 10^{-11}\ Torr$ vacuum. The sample was kept in the fixed position relative to the beam polarization, and the analyzer was rotated. The beam polarization was in the sample plane perpendicular to $\Gamma - Y$ direction, with beam nearly at grazing incidence with the sample surface. We used a Scienta SES 200 analyzer in the angle mode, where cuts parallel to $\Gamma - Y$ direction are carried out. The momentum resolution was $\pm 0.006\ \AA^{-1}$ in the scan direction and $\pm 0.019 \AA^{-1}$ in the perpendicular direction for 55 eV photon energy and better for other energies, and the energy resolution was $7 - 18\ meV$. An extensive and fine sampling mesh with more than 4000 EDCs for each photon energy was collected. The slightly overdoped Pb-doped Bi2212 ($Tc = 84K$) and overdoped Pb-doped Bi2212 ($Tc =$

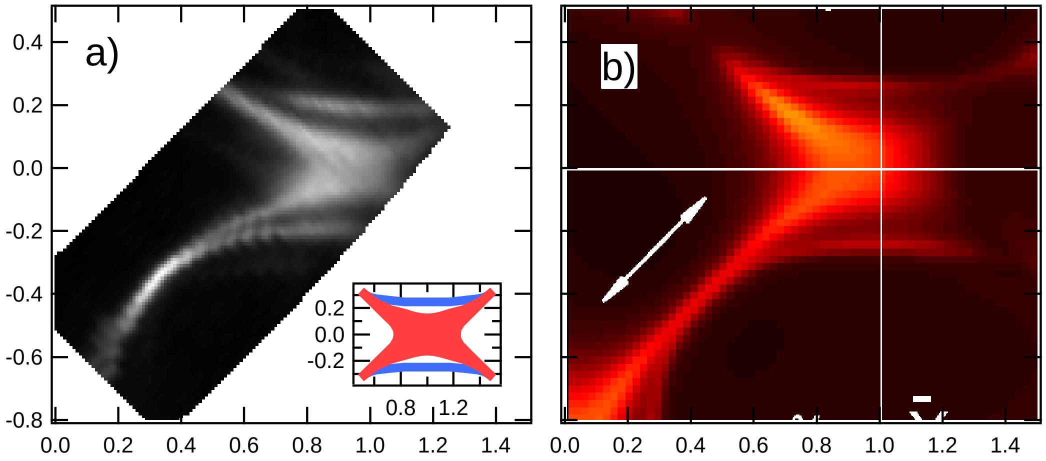

Figure 5.2: Panel a)shows experimental spectral intensity map at 12 meV BE collected using 22 eV photons. Panel b) shows calculated ARPES intensity for Bi2212 in the same experimental conditions by Bansil *et.al*. Light polarization is given by the arrow in this panel and is the same as in panel a). Inset in panel a) schematically indicates two Fermi surface pieces.

$70K$) were grown using the floating-zone method. The single crystalline samples were oriented by using Laue diffraction ex situ and cleaved in situ in vacuum. The samples were measured at 100K (Fig. 5.1, 5.2 and 5.4) and 20K (Fig. 5.3). The Fermi energy was obtained from the EDCs of polycrystalline Au.

5.3 Results and Discussion

In panel a) of Fig. 5.1 we show the map of spectral intensity at Fermi energy (E_F) obtained at 22 eV photon energy. The white arrow shows the polarization of radiation with respect to the crystal surface. To determine the spectral intensity map we divide each EDC by the integrated signal intensity from a 100 meV window above the E_F, which comes from higher order synchrotron light and is proportional to photon flux. The normalized EDCs represent electron spectral function weighted by the Fermi function and matrix element[3]. The highest intensity points in the spectral intensity map at the Fermi energy give one method for determining Fermi surface. In panels

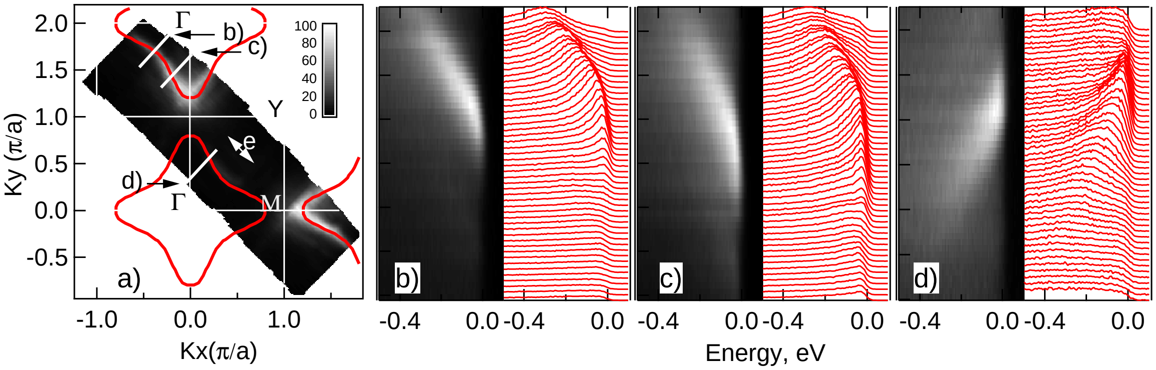

Figure 5.3: Gray scale image in panel a) shows the spectral intensity at the Fermi level collected with 55 ev photons. The white arrow shows the polarization of radiation with respect to the crystal surface. Arrows and thick lines indicate the cuts presented in panels b) - d). Red line indicates the Fermi surface shape. Panels b) - d) show data along select cuts in the Brillouin zone. Left side of each panel shows 2D plot with brightness proportional to signal intensity, while right side shows corresponding EDCs equally spaced in vertical direction for clarity.

1a)-5a) we plot raw EDC data obtained along select cuts shown in panel a) by green arrows. Here, the Fermi surface crossing is defined as the location in the momentum space where the intensity of the spectral feature decreases drastically and the leading edge crosses the Fermi level. From both the near E_F spectral weight image plot and from the EDCs one clearly sees two Fermi surfaces, as indicated by solid ovals in panels b to f. The concomitant presence of two Fermi surface pieces had not been reported before.

Fig. 5.2a) shows 22 eV data from another sample taken in a more extended k-space area. This data were taken at 20K in the superconducting state, where the spectral weight around the M point is suppressed at the Fermi level due to the superconducting gap opening, so the map shown corresponds to 12 meV BE. This map can effectively be used to indicate the underlying Fermi surface. Although the maximum gap is larger than the energy window, finite resolution still reveals the underlying Fermi surface, and a larger integration window does not change the picture. These data, as well as the normal state data in panel a) of Fig. 5.1, show striking resemblance to

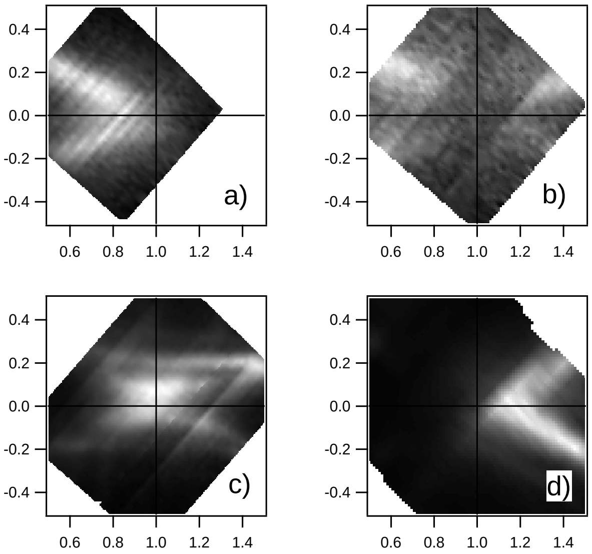

Figure 5.4: In this figure spectral intensity maps at the Fermi level for different photon energies are shown. Panel a) shows data collected at $27eV$, panel b) shows $33eV$ data, panel c) shows $44eV$ data and panel d) $55eV$ data.

theoretical simulation by Bansil et al. [4] for the same photon energy and polarization, as shown in panel b). The simulation uses first-principles one-step photoemission model calculation and comes up with two bands for two adjacent CuO_2 planes in a unit cell. These two bonding and antibonding bands give rise to two Fermi surfaces. The bonding piece is an outer hole-like piece, indicated by blue lines in the inset of panel a). On the other hand the antibonding piece, indicated by the red area in the inset of panel a), is hard to dicern from these data, because the saddle point of the band is very close to E_F at $(\pi, 0)$ [81]. The simulation also indicates that the image plot is very similar whether this piece of the Fermi surface is hole-like or electron-like, i.e. whether the Van Hove saddle point is above or below E_F. The absence of superstructure complication in our data and the striking similarity between experiment and theory strongly suggest that there are indeed two pieces of the Fermi surface in Pb Bi2212.

The Fermi surface as seen under other measurement conditions turns out to be very different. Fig. 5.3 shows data recorded at 55 eV under the same measurement geometry. Panel a) shows the map of spectral intensity at E_F in the momentum space. In panels b), c) and d) we plot raw data obtained along the select cuts shown in panel a) by thick white lines. Cut b) is close to the nodal direction in the second Brillouin zone, while cuts c) and d) are cuts equidistant from M point. The sampling density in the cuts is very high and is representative of the sampling density of the entire k-space studied. These high quality data clearly show a quasiparticle dispersing towards the Fermi level, eventually crossing it and disappearing. While the intensity map in panel a) hardly shows any features in the first zone, panel d) clearly shows a well-resolved feature crossing the Fermi level, similar to panel c), with the overall intensity a factor of 10 lower than that in panel c). In fact, all features seen in the second zone are observed in the first zone as well. The Fermi surface shape emerging for this photon energy is electron-like. We have confirmed this result with data taken in all three Brillouin zones by using three complimentary methods: intensity map at E_F, sharpest drop in $n(\vec{k})$ and the traditional method of tracking the EDCs. The contrast in data from Figures 5.1-5.3 immediately suggests that the 55 eV data picks out the inner piece of the Fermi surface.

To investigate the photon energy dependence of the FS further, we collected data at other photon energies, and in Fig. 5.4 we plot the measured spectral intensity maps at E_f. In panel a) we plot our spectral intensity map collected at 27 eV. We see an electron-like FS in the first zone, and the spectral weight in the second zone is significantly suppressed. This complements the 55 eV data in panel d). In panel b) at 33 eV photon energy spectral intensity map shows strong suppression of the spectral weight at the M point and can be interpreted as either hole-like and electron-like. These data are quite different from earlier results recorded at another geometry [75, 76, 77]. 44 eV data in panel c) look very similar to the 22 eV data in panel a) with bilayer-split Fermi surfaces. Spectral weight map FS results are supported by individual EDC analysis.

There is a very unusual photon energy related variation in the ARPES data. With the large unit cell size in the normal direction ($c \approx 30.6\mathring{A}$), one would expect a periodicity with 1-2 eV steps in photon energy for the energy range studied. Surprisingly,

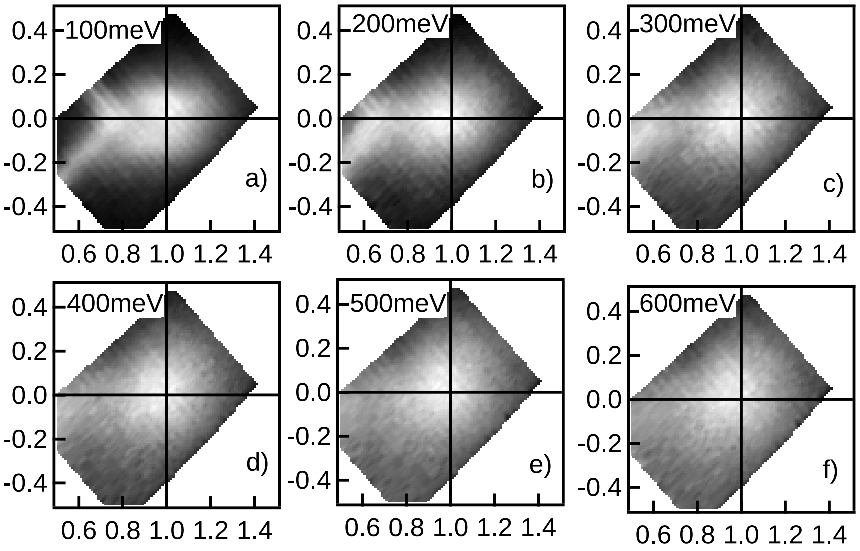

Figure 5.5: In this figure cuts at constant energy collected with 22 eV photons are shown. Panels a)-f) correspond to 100-600 meV binding energy.

this is not the case. The existence of bilayer split Fermi surface means strong interaction between the two CuO_2 planes in the Bi2212 unit cell. It is reasonable to assume that the variation in the data with photon energy is also driven by the separation of the layers, $d \approx 3.4\AA$, with corresponding $Kz = \frac{2\pi}{d} = 1.85\AA$. This would be more consistent with the observed variation with large photon energy intervals. Calculations similar to [4] for a range of photon energies will be very useful to understand this phenomenon.

The variation of the spectral intensity map at the Fermi level with photon energy is not the only interesting aspect of the data. Data collected at 22 eV and 27 eV photon energies show spectral weight at the M point, present up to the highest binding energy (BE) measured (600 meV), as illustrated for 22 eV in Figure 5.5. At the same time, data collected at 33 eV, 44 eV and 55 eV photon energies show no such feature. The location of this spectral weight as well as no noticeable dispersion of the feature are consistent with Bi-derived bands, since pure Bi 5d states are located at 23.8 eV and 26.9 eV BE.

Our results, in particular the variation of the Fermi surface picture with photon energies and the observation of the bilayer splitting, contradict earlier reports from Pb doped Bi2212. Previous data [8, 79] from the same material at different photon energies were interpreted as an evidence for the hole-like Fermi surface and were used to argue for the universality of the Fermi surface topology. We attribute this discrepancy mostly to poorer energy (70 meV compared to ours 7-18 meV) and momentum ($0.094\mathring{A}^{-1}$ compared to ours $0.006 \times 0.019\mathring{A}^{-1}$) resolution used in that study for photon energies other then 22.4 eV. Unconventional normalization procedure employed in [8, 79] can also be responsible. Recently attempts were made to support a single universal hole-like Fermi surface picture by invoking matrix element arguments[9, 78]. While a band calculation did show a strong spectral intensity variation with photon energy [4], it is not applicable to Fermi surface determination at a particular photon energy. What really matters is the matrix element variation in a small region in the same Brillouin zone, which is actually small [4]. The unambiguous evidence for two Fermi surface pieces show the matrix element argument for single universal hole-like Fermi surface to be misleading and incorrect.

The polarization setup used in our experiment is favorable for observing the bilayer splitting [4]. It may explain the failure by other researchers to observe two Fermi surface pieces at 22.4 eV. The failure to observe the splitting of the bands due to the interaction between the layers has been a long standing problem. Earlier photoemission results were interpreted as evidence for the absence of the bilayer splitting [73]. Our data in Fig. 5.1, 5.2 and 5.4, collected with much better energy and momentum resolution, show the splitting to be present, even for the samples with Tc not far from optimal.

5.4 Conclusions

The picture emerging from the above is clear: there are two pieces of the Fermi surface, one of them clearly hole-like. The other piece is different, as it lies very close to the special point where the Fermi surface changes from hole-like to electron-like, with small change in chemical potential or $\vec{K}_Z$. This is the underlying reason for this piece to behave slightly differently at different photon energies. This picture provides a unifying foundation for all the controversial reports on the FS shape in Bi2212. The Bi2212 Fermi surface has always been attributed to the CuO_2 plane, and because doping with Pb does not change the CuO_2 plane, the Fermi surface in Pb-doped and Pb-free compounds should be the same. Our finding indicates that the accepted picture of a single hole-like Fermi surface in Bi2212 for the entire doping range studied is incorrect. Instead, there exists another Fermi surface piece that is at the boundary between hole and electron character.

Chapter 6

Fermi Surface Studies: LSCO - Model Stripe Compound

In this chapter we report photoemission spectroscopy results from $(La_{2-x-y}Nd_ySr_x)CuO_4$ (pure ($y = 0$) and Nd-LSCO). $(La_{1.4-x}Nd_{0.6}Sr_x)CuO_4$ is a model system with static one-dimensional (1D) charge and spin order (stripe), and $La_{2-x}Sr_xCuO_4$ is a high temperature superconductor, with possibly dynamic stripes at low doping. In the electronic structure of the $x = 0.12$ Nd-LSCO the low energy excitations near the expected $d-$wave node region are strongly suppressed. The frequency integrated spectral weight is confined inside one−dimensional segments in the momentum space (defined by $|k_x|=\pi/4$ and $|k_y|=\pi/4$), deviating strongly from the more rounded Fermi surface expected from band calculations. More importantly, this departure from the two−dimensional Fermi surface persists to very high energy scale. Nd-LSCO at $x = 0.15$ doping and pure LSCO at $x = 0.15$ doping show a combination of 1D spectral weight similar to 0.12 Nd-LSCO, but also a signature of nodal spectral weight, while overdoped $x = 0.22$ LSCO shows two-dimensional Fermi surface consistent with band structure calculation with remnant signature of stripe order. These results provide important information for establishing a theory to understand the charge− and spin−ordering in cuprates and their relationship with high temperature superconductivity.

6.1 Introduction

The stripe phase [25, 26, 27] has attracted considerable attention in connection with recent neutron scattering data from Nd−substituted $(La_{1.48}Nd_{0.4}Sr_{0.12})CuO_4$ (Nd−LSCO) [28]. In the neutron data 4 incommensurate peaks in elastic neutron scattering were found near the antiferromagnetic (π, π) peak, with the (π, π) peak itself suppressed. The result was particularly exciting because of the suppression of T_C in Nd-LSCO at the same doping (see top panel of Fig 6.1). Other experiments observed elastic (Nd-LSCO) and inelasic (pure LSCO) incommensurate neutron peaks in a wide range of dopings [28, 29, 30] for the LSCO family of cuprates. The results of these measurements are summarized in the middle panel of Fig. 6.1. The phase diagram is separated into 3 distinct regions - anti-ferromagnetic region (I), diagonal stripe region (II), and horizontal stripe region (III). In each of these regions distinct neutron scattering pattern can be observed. Incommensurate neutron peaks can be characterized by their separation from the (π, π) direction δ. The bottom panel of Fig. 6.1 shows δ as a function of doping. We see, that δ increases gradually with doping, until it saturates at $x = 0.12$.

Tranquada et. al. [28] proposed an explanation for the $x = 0.12$ neutron data in terms of a static stripe picture, see Fig.6.2. The stripe picture represents a new paradigm to think about charge carriers in a solid. Unlike conventional metals where the charge distribution is homogeneous, the stripe picture asserts that the charge carriers are segregated into one−dimensional domain walls. At the same time, the electronic spins in the domain between the walls order antiferromagnetically with a π phase shift across the domain wall. The possibility of charge segregation propensity and its implications on conduction as well as superconducting mechanism are at the heart of the current debate in high−T_c research [25, 26, 27, 28, 29, 30, 31, 32, 33, 34, 35, 36, 37, 38, 39, 40, 41, 42, 43, 44, 45, 46, 47, 48, 49, 50, 51]. Within the context of stripe picture, it is a formidable task to develop a theory describing the electronic structure that provides the microscopic foundation to understand the physical properties. The difficulty stems from the fact that our theoretical machineries are developed either in real space or in momentum $k-$ space. For an inhomogeneous

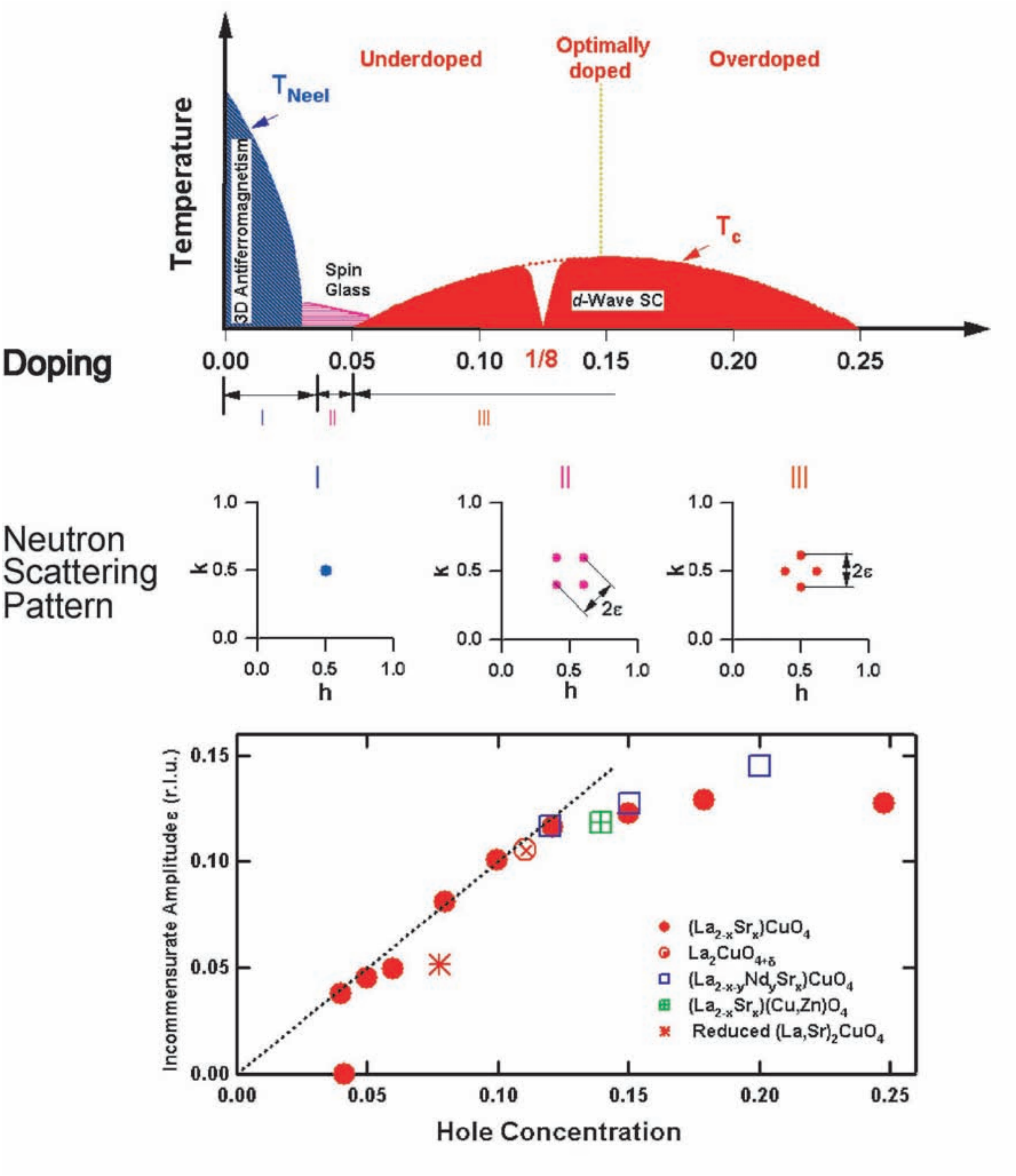

Figure 6.1: Top panel in this graph shows the phase diagram of La$_{1.6-x}$Nd$_{0.4}$Sr$_x$CuO$_4$, with the suppression of superconductivity at $x = 1/8$ doping. The phase diagram can be separated into 3 distinct regions from the results of neutron scattering measurements - anti-ferromagnetic region (I), diagonal stripe region (II) and horizontal stripe region (III). In each of these regions distinct neutron scattering pattern can be observed. Middle panels described the neutron scattering patterns in each doping range. The bottom panel shows the dependence of the peak separation δ as a function of doping x.

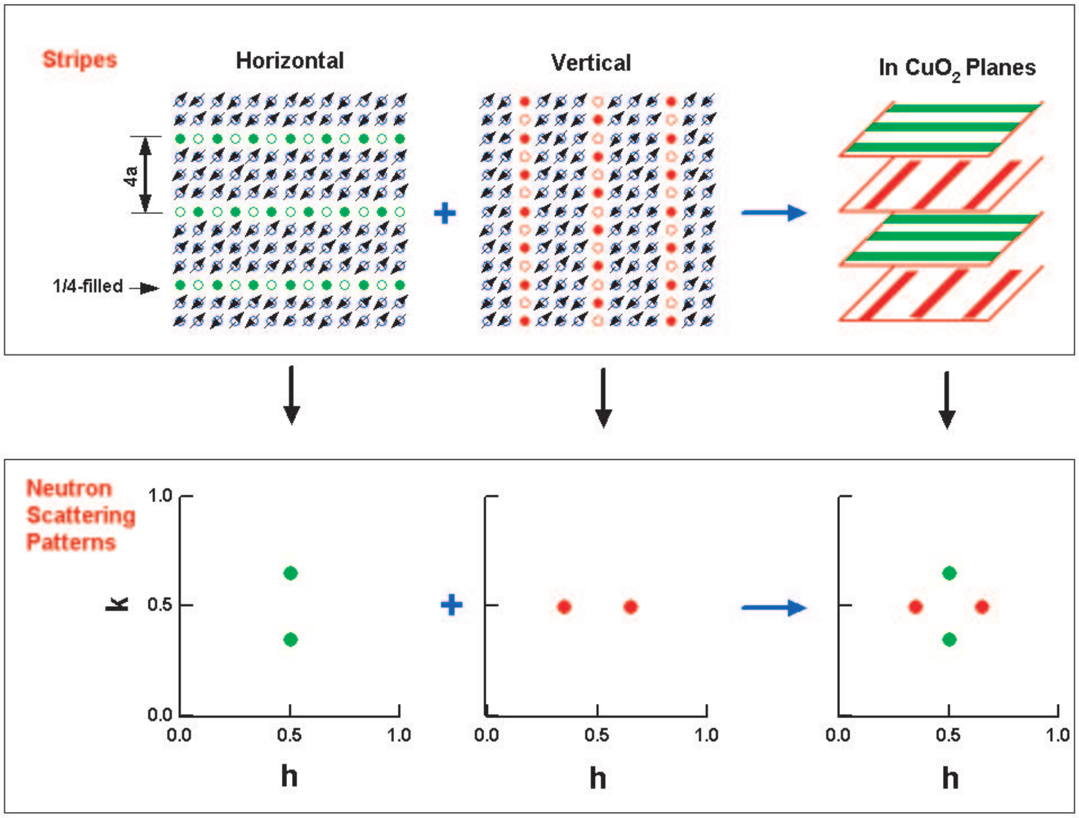

Figure 6.2: Top panel shows the model of static stripes in $x = 1/8$ Nd-LSCO. Bottom panel describes the effects such static stripes would have on neutron scattering.

system like the charge−ordered state, a hybrid description appears to be necessary. This is even more difficult when the strong many−body effects have to be taken into account. So far, little information about the electronic structure of the stripe phase is available. In this chapter angle−resolved photoemission data are reported for pure and Nd−LSCO. These results may provide a phenomenological foundation to build a comprehensive theory on the charge and spin ordering in cuprates, their doping dependence and relationship with superconductivity.

6.2 Experiment

The ARPES data have been recorded at the beamline 10.0.1.1 of the Advanced Light Source. 55eV photon energy was used for more efficient k−space sampling. Using the angular mode of the Scienta analyzer, the momentum resolution was 0.02π. The energy resolution is detuned from its optimal 7 meV to 16 meV so that a few thousand spectra with sufficient statistics can be obtained during the lifetime of a cleaved surface. For example, the 500 spectra presented in Fig. 6.3 of this chapter were recorded within the first 3 hours after cleaving; the results are robust from cleave to cleave. The vacuum during the measurement was $2{\sim}5\times10^{-11}$ Torr. Low energy electron diffraction (LEED) experiments have been performed to check the surface structure, yielding the expected four−fold symmetry. The pure and Nd−LSCO samples were grown using the traveling floating zone method. The same class of samples has been used for neutron scattering experiments [27].

The angular mode of the analyzer was used to scan along the crystal axis a (Cu-O bond direction) for x = 0.12 and 0.15 Nd-LSCO; the whole Brillouin zone was then measured by taking various k_y cuts. To check for polarization effects we also scanned along the diagonal direction for x = 0.15 Nd-LSCO and for x = 0.15 and 0.22 pure LSCO, and the mapping was realized by rotating the analyzer. In the first configuration the electrical vector $\vec{E}$ of the incident light was nearly normal to the sample surface, while for the second configuration it was parallel to the sample surface.

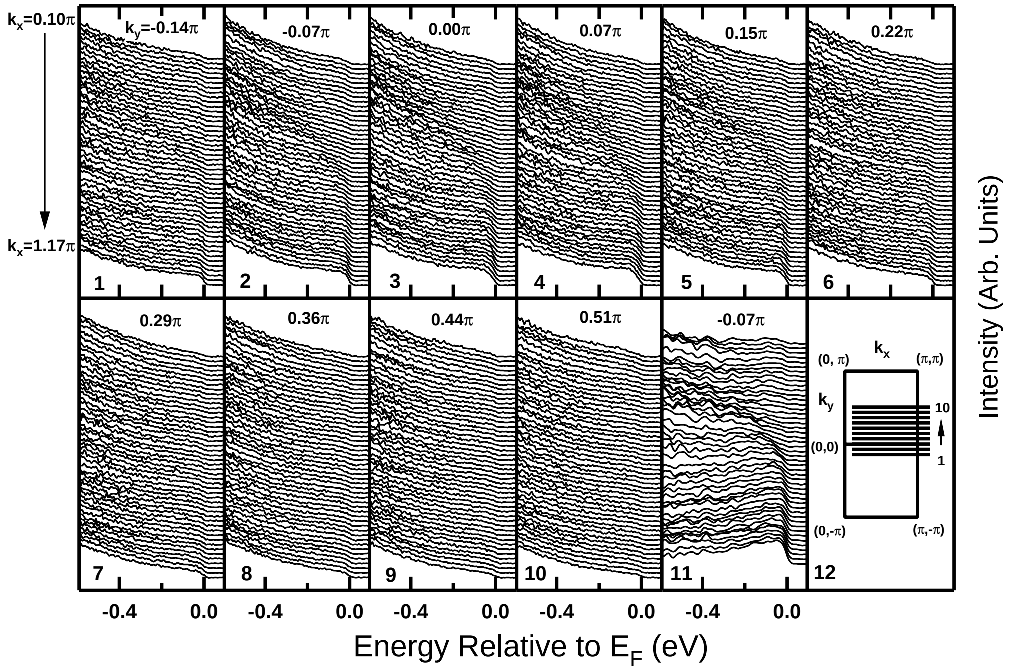

Figure 6.3: Angle−resolved photoemission spectra taken on Nd−LSCO at 20K. The measurement scheme is depicted in panel 12 which covers the first and fourth quadrants. Each of the panels 1−10 represents a cut parallel to the (0,0) to (π,0) direction with k_x covering from 0.10π to 1.17π with an interval of 0.023π. Panels 1 to 10 covers k_y from -0.14π to 0.51π with an interval of 0.07π. Panel 11 shows the same spectra in panel 2 but with the high energy background removed.

6.3 The Nd-LSCO results at the critical doping $x = 0.12$

In this section we discuss the results from the $x = 0.12$ Nd-LSCO sample, the material with the stripe structure proposed in Figure 6.2. To demonstrate the quality of the data we plot $x = 0.12$ Nd-LSCO data with different k_x in Figure 6.3. The 48 points presented in each panel were collected at the same time. Although the spectra do not contain sharp peak structure, the data still show edge or cusp−like structures with clear angular dependence. Typical spectra of Nd−LSCO (Fig. 6.3) were sampled from the first and fourth quadrants of the Brillouin Zone (BZ) at a temperature of 20 K. As seen from the panels 1 to 6, with k_x varying from 0.10π to 1.17π (the unit of the momentum is $1/a$ with a being the lattice constant), a broad feature moves from 200 meV or deeper towards the Fermi level E_F and stays there for an extended region near k_x=π. This dispersion, as well as a strong angular dependence of the spectral weight described below, indicates that the absence of well−defined peaks is not a consequence of random disorder or a poorly−cleaved surface. This conclusion is also consistent with the observed LEED pattern

In the spectral intensity plot integrated over 500 meV energy window of the Fermi level from $x = 0.12$ Nd-LSCO (Fig. 6.4), panel (A) plots the raw data while panel (B) gives the four−fold symmetrized data. This symmetrization is justified because, in a separate data set that covers the whole quadrant, we did observe high spectral intensity near (π,0) and (0, π), making the data nearly symmetric with respect to the (0,0)−(π,π) line. The spectral weight, when integrated over a large frequency window, represents the momentum distribution function $n(k)= \int_{-\infty}^{+\infty} A(k,\omega)f(\omega)d\omega$ weighted by the photoionization cross section. The k−dependence is very clear in the momentum distribution function, lending strong support for the k−resolved nature of the data even though the features are not very sharp in energy. The high $n(k)$ area is approximately confined within one−dimensional segments with the range of $|k_x|\leq\pi/4$ for any k_y or $|k_y|\leq\pi/4$ for any k_x (Fig. 6.4B). On the other hand, the low energy spectral weight (Fig. 6.5) is mostly concentrated near the (π,0) region. It is also striking that there is little or no low energy spectral weight near the zone diagonal [(0,0) to (π,π) direction], where the d−wave gap has nodes. The absence of such a Fermi crossing in Nd−LSCO can be best illustrated by the absence of any dispersive feature for the k_y=0.44π cut (Fig. 6.3(9)), indicating that the usual Fermi surface near the d−wave node region is very poorly defined.

In general, the $n(k)$ pattern allows one to determine the underlying Fermi surface that separates the occupied area from the unoccupied area. Here the “occupied” area means that the occupation probability is high. In an interacting system, $n(k)$ will not be zero even in the region when the “band” is above the Fermi level. There

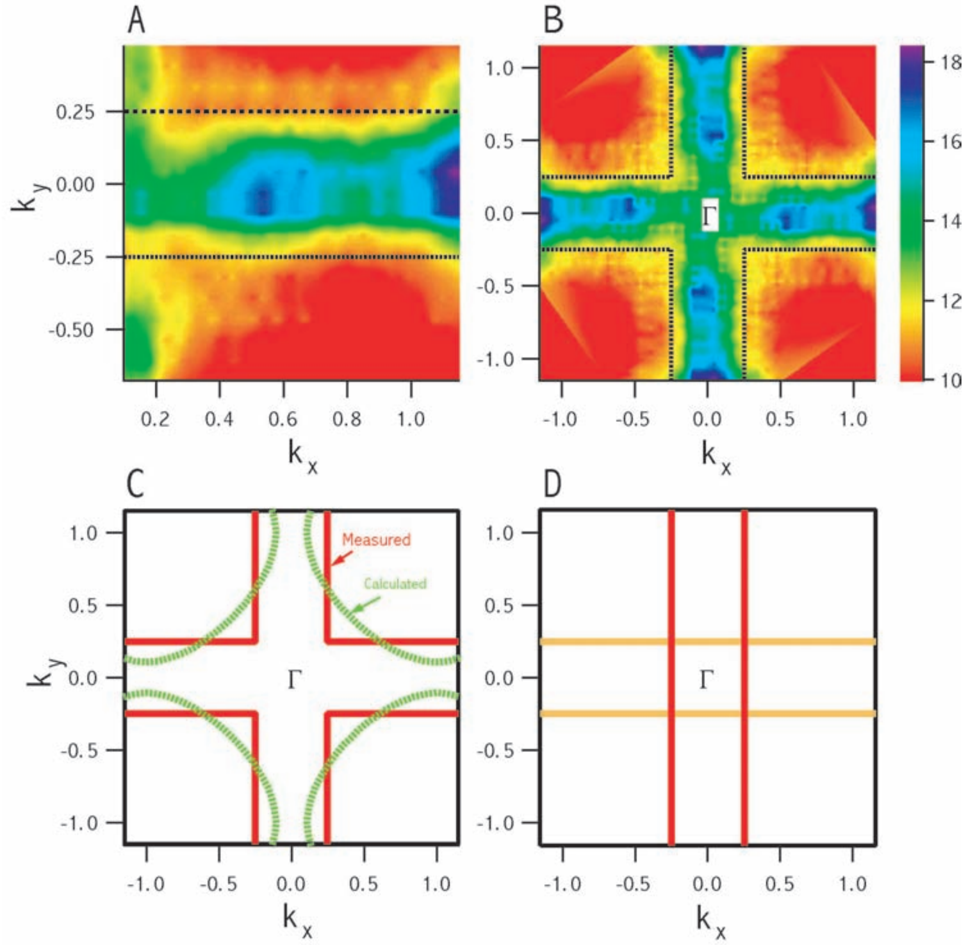

Figure 6.4: Spectral weight integrated within 500 meV of the Fermi level, as a function of k_x and k_y. **A** is obtained directly from the raw data while **B** is obtained by symmetrizing A using four−fold symmetry. The dashed lines in **A** and **B** define the regions where the spectral weight is mainly concentrated. **C** depicts the underlying Fermi surface (solid line) obtained from **B** that encloses the high spectral weight region. The calculated Fermi surface for 2D CuO_2 plane (*28*) is also shown (in dashed line) for comparison. **D** depicts the Fermi surface expected from two perpendicular 1D stripe domains in one−dimensional interpretation.

are two possible ways to think about the $x = 0.12$ data that are consistent with charge density modulations, albeit at very different limits. In the limit that the charge density modulation is weak, a 2D interpretation of the data is probably a reasonable starting point. The Fermi surface determined is approximately the lines of k_x=$\pm\pi/4$ or k_y=$\pm\pi/4$ as depicted in Fig. 6.4C. Counting the occupied area of the Brillouin zone, one gets 7/16, or 1/16 short of 1/2 of a BZ area. With the spin degeneracy, this is consistent with the 1/8 doping of the system. The shape of the Fermi surface has some qualitative resemblance to what one expects from a band calculation (dashed lines in Fig. 6.4C) [52], although the straight 1D segments are absent in the calculation. In this case, we have almost perfectly nested Fermi surface segments which would favor a charge−density wave (CDW) instability leading to a quasi−2D picture. Simple geometrical consideration of the cross−like Fermi surface leads to the conclusion that the Fermi surface nesting is commensurate with the lattice at 1/8 doping. Electron−phonon interaction would favor a CDW at this filling level. This is consistent with the fact that 1/8 doping is where most of the anomalies are observed and also that spin ordering temperature is correlated with structural phase transition [28, 29, 53].

There are serious problems with the above quasi−2D picture for the strongly charge−ordered Nd−LSCO. First, there is no obvious origin for the almost perfectly nested Fermi surface segments. Second, it is unclear why the states near the d−wave node are strongly suppressed if the charge modulation is very weak. As shown in Fig. 6.4 and 6.5, the suppression of the d−wave node state can be thought of as the opening of a large gap (500 meV or beyond) if one insists on the quasi−2D picture. It is difficult to justify the opening of such a large gap with phonons. Furthermore, a CDW would open a gap along the entire nested Fermi surface segments, not preferentially along the d−wave node only. Third, the quasi−2D picture is not consistent with the neutron scattering data where the two pairs of the incommensurate scattering spots are interpreted to be from stripes in two adjacent planes that are rotated by 90 degrees [28, 29]. In addition, the CDW picture does not have as natural a connection to the spin density wave observed as a stripe picture would.

We now discuss an alternative interpretation, which is consistent with the stripe

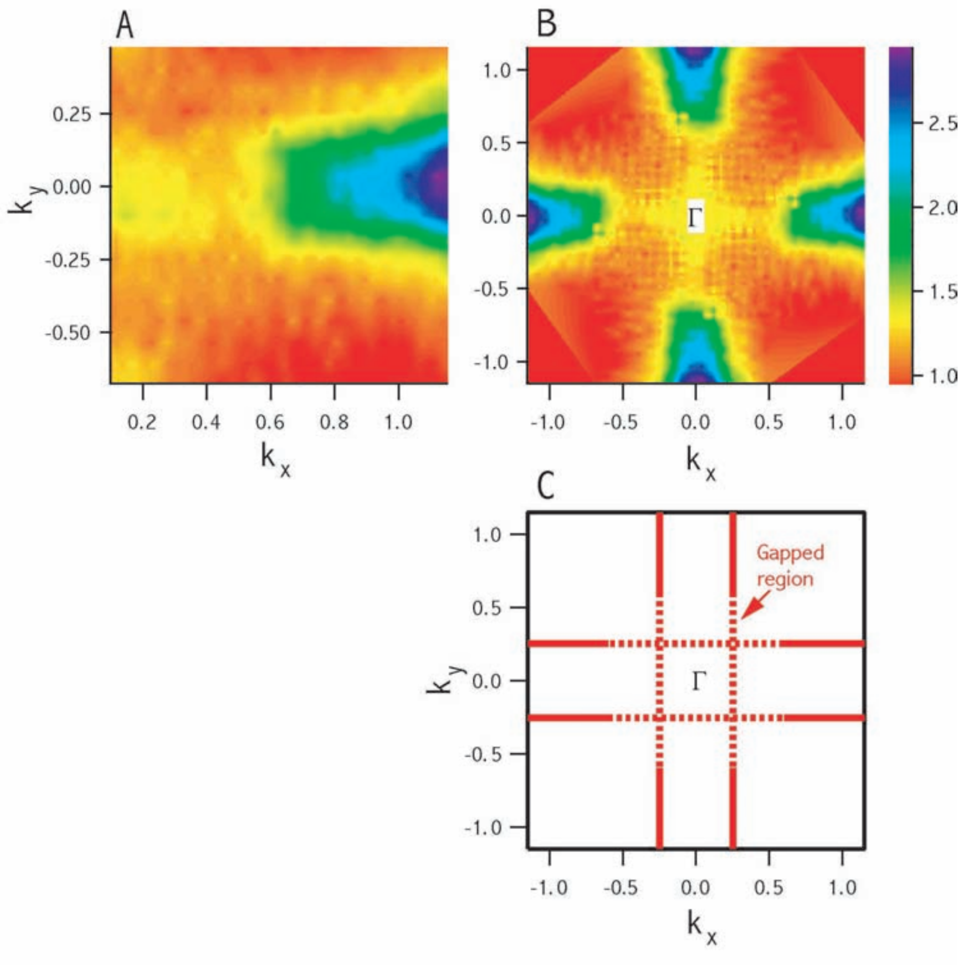

Figure 6.5: Spectral weight integrated within 100meV energy window of the Fermi level, as a function of k_x and k_y. **A** is obtained directly from the raw data while **B** is obtained by symmetrizing **A** using four−fold symmetry. **C** illustrates the underlying Fermi surface where the gap may open; the dashed lines indicate the possible gapped region.

picture, in terms of a hybrid of the real and $k-$space picture. Here the charge modulation is assumed to be much stronger. It is plausible that the four$-$fold symmetry seen in our experiments stems from two sets of orthogonal domains as depicted in Fig. 6.5. At 1/8 doping, neutron and X$-$ray scattering experiments suggest that each charge stripe is separated by three antiferromagnetic lines so the charge has a periodicity of $4a$, while the stripe itself is 1/4 filled (Fig. 6.6A and B) [28, 29, 54]. For each domain, the Fermi surface is either the k_x=$\pm\pi/4$ or k_y=$\pm\pi/4$ lines (Fig. 6.6C and D). Note that the stripes along the horizontal direction give rise to the vertical Fermi surface lines of k_x=$\pm\pi/4$. In this context, the Fermi surface observed can be understood as a superposition of two perpendicular Fermi surfaces arising from two different domains (Fig. 6.2D). The stripe phase contains undoped insulating areas and doped metallic areas. The signal from the insulating areas is pushed to higher binding energy because of the Mott gap; the low energy feature is thus mainly from the metallic region. A two component electronic state has been observed in $(\mathrm{La}_{2-x}\mathrm{Sr}_x)\mathrm{CuO}_4$ near the metal$-$insulator transition region of x$\sim$0.05-0.07, consistent with this picture [55]. With static stripes, one expects this effect to be enhanced in Nd$-$LSCO. Because the metallic stripes are 1/4 filled at 1/8 doping [28, 29], it is consistent with the occupied state being confined within $|k_x|$=$\pi/4$. In this scenario, there should be a potential between the charge$-$rich and charge$-$poor regions.

The above discussion leads to a picture that favors the 1D approach rather than the quasi$-$2D approach for the electronic structure of Nd$-$LSCO, although our results alone cannot definitely distinguish between them; the occupied area agrees with the Luttinger volume in both cases. The straight segments seen in the raw data clearly reveal the 1D$-$like Fermi surface sections that will manifest itself in transport experiments independent of the interpretation [53]. How to reconcile the $k-$space picture (Fermi surface, etc.) and the real space picture (inhomogeneous charge distribution) is a key difficulty to describe the stripe phase. The data can probably provide insight into this problem by providing $k-$space information of the stripe phase.

The likely interpretation of the data is that the horizontal spectral weight concentration is from vertical stripes (along the y direction). As shown in Fig. 6.6, the confinement of the spectral weight within k_y=$\pm\pi/4$ can be understood because, for a

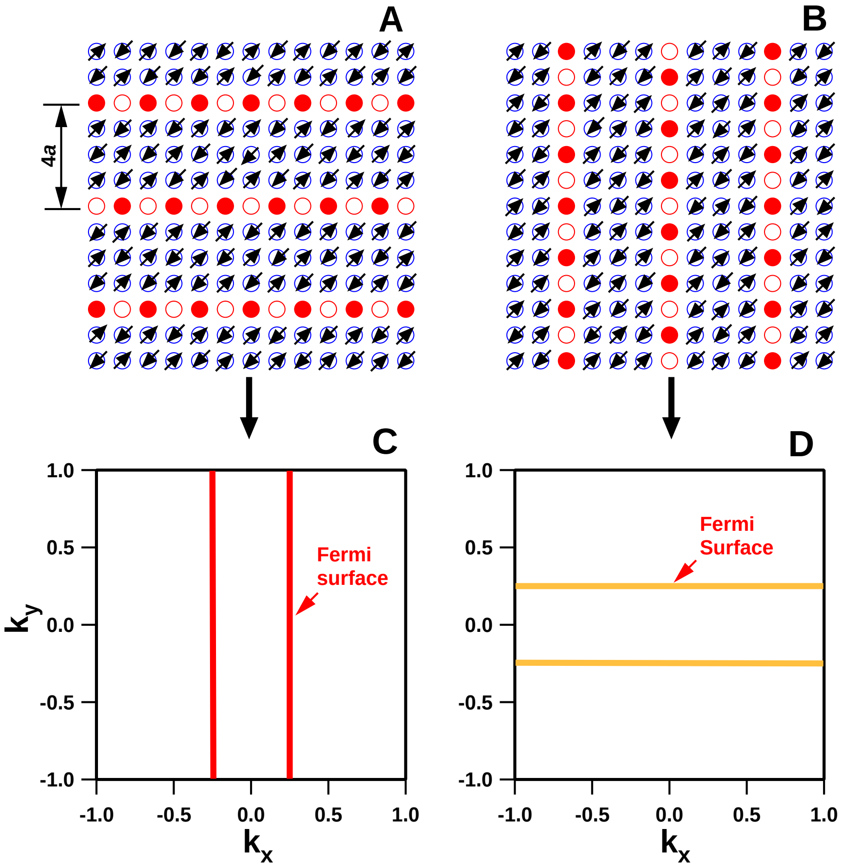

Figure 6.6: Models of static horizontal **A** and vertical **B** stripes and their corresponding Fermi surfaces. The horizontal stripe **A** is expected to result in the Fermi surface defined by the lines $|k_x|=\pi/4$ **C** while the vertical stripe **B** results in the Fermi surface defined by the lines $|k_y|=\pi/4$ **D**.

given k_x, one only sees the occupied band within $k_y \leq \pi/4$ as the vertical stripes are 1/4 filled. This interpretation is further supported by the model calculation, where the calculated spectral density for the vertical stripes is qualitatively in agreement with the measured spectral confinement near (π,0) (Fig. 6.5A) [44]. This picture also provides a possible explanation for the two broad intensity maxima in *n(k)* (Fig. 6.4A). These two maxima are separated in k_x by about 0.5π, consistent with a real space stripe periodicity of $4a$.

The data presented here seem to present some apparent paradoxes. The persistence of the 1D−like character up to 500 meV or beyond (Fig. 6.4) is unexpected from theories that start with quasiparticles defined very close to the Fermi energy. From the viewpoint of Fermi liquid plus CDW theory, and given the relatively low ordering temperature (30∼70 K), one would expect a 1D behavior only at an energy scale much lower than 500 meV. The solution to this dramatic departure from the Fermi liquid paradigm appears to call for a different basic starting point. Instead of quasiparticles, one may start with stripes that are at least locally stable up to very high energy, as reflected in ARPES data which are mainly sensitive to the local information at such high energy. The fluctuation of the stripes may give rise to the global 2D character in the intermediate energy and temperature scale. The ordering seen in neutron scattering and NQR experiments is the freezing out of these fluctuations [28, 29, 51] that results in the long range order. In this sense, one may consider that the ARPES data reflect the local amplitude of stripe formation which is of high energy scale, while the neutron scattering and NQR data reflect the phase of stripe correlation.

6.4 Optimally doped ($x = 0.15$) Nd-LSCO and pure LSCO results

In this section, we discuss the results away from 1/4 filled stripes in $x = 0.12$ Nd-LSCO. Signatures similar to that from the $x = 0.12$ sample were observed at other dopings in Nd-LSCO [54, 51, 56]. Evidence for dynamic stripes was also observed in pure LSCO and other high temperature superconductors. [57, 58, 59, 30, 50] (see also bottom panel of Fig. 6.1). A key issue is whether the stripe phase can conduct, and the related issue is whether stripe formation is responsible for high temperature superconductivity [25, 26]. We describe the results from $x = 0.15$ Nd-LSCO and $x = 0.15$ pure LSCO samples. Unlike the $x = 0.12$ Nd-LSCO case, here we have identified the existence of the spectral weight along the [1,1] nodal direction. This spectral weight is weaker in static stripe material and is stronger in dynamic stripe material.

In Figure 6.7, we plot low energy (30 meV integration) spectral weight of Nd-LSCO (x=0.15) (a) and LSCO (x=0.15) (b). We can describe the spectral map in terms of two features: the straight segment near the antinodal region and the spectral weight near the nodal region with its associated Fermi surface. While it seems to be straightforward to associate the straight segments with stripes because of their 1D nature [44], the detection of spectral weight near the nodal region in the *static* stripe phase in $x = 0.15$ Nd-LSCO poses a new challenge to our understanding of this charge-ordered state because nodal spectral weight is expected to be suppressed in a simple static stripe picture [46, 60]. The experimental question regarding the origin is whether they originate from another distinct phase or they are intrinsic properties of the same stripe type. In the case of phase separation, this would mean that, besides stripes, there is another non-stripe metallic phase with a much higher carrier concentration, as estimated from the Luttinger volume of the diamond-shaped Fermi surface (Fig. 3). As far as we know, there is little evidence of such a phase separation in Nd−LSCO and LSCO systems at the doping level discussed here [55], although it has been observed in a related $La_2CuO_{4+\delta}$ system [48].

The detection of nodal spectral intensity in the stripe system provides a clear distinction of the stripe physics from the ordinary 1D charge motion in a rigid one−dimensional system. In the stripe context, the nodal Fermi surface may arise from disorder or fluctuation of stripes where the holes leak into the antiferromagnetic region[44]. Here disorder also induces the effect that the antiferromagnetic region may not be fully gapped when it becomes very narrow. The measured spectral weight in Fig. 6.7 for Nd−LSCO and LSCO is similar to the one calculated based on such a

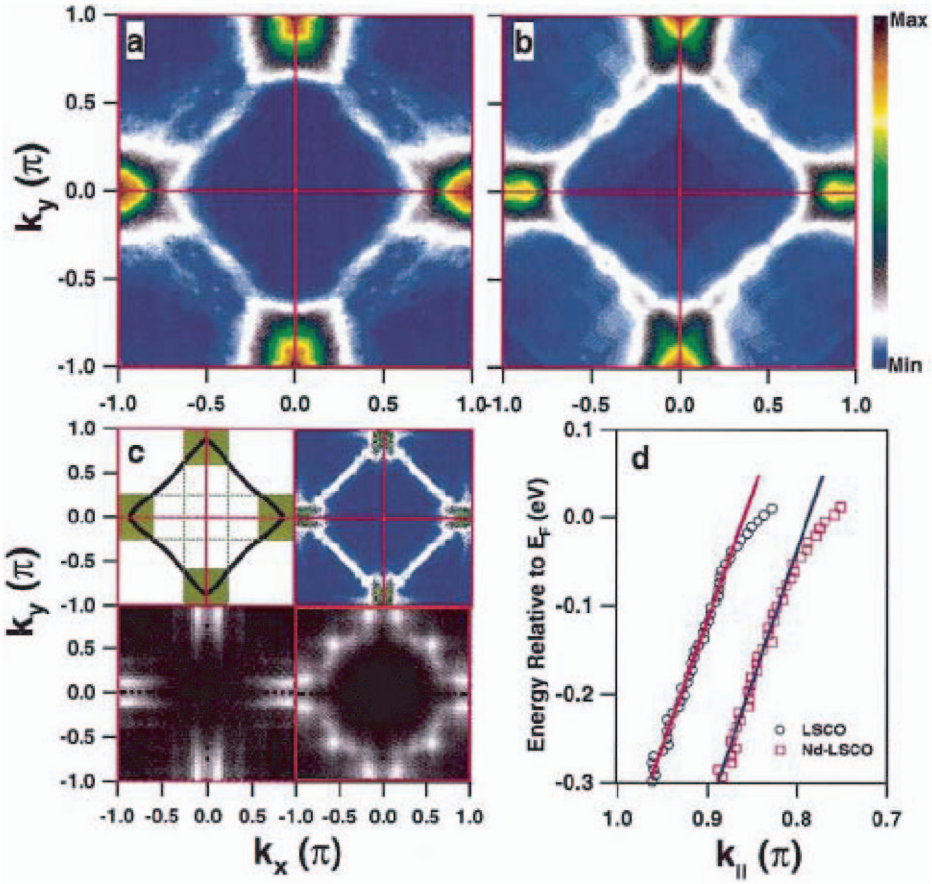

Figure 6.7: Measured low energy (30meV integration) spectral weight of Nd−LSCO (x=0.15) (a) and LSCO (x=0.15)(b), as obtained by symmetrizing the first zone data of Fig. 2. The observed two features are schematically illustrated in (c) (upper−left panel): diamond−shaped nodal Fermi surface (black line) and 1D spectral confinements near (π,0) and (0,π) regions. The spectral weight patterns calculated from stripe fluctuation (upper-right panel)[19], from the site-centered stripe (lower−left panel) and bond−centered stripe (lower−right panel) [26] are also included in (c) for comparison. Fig. 3(d) shows the dispersion along the nodal direction (in the second zone) for the Nd−LSCO and LSCO samples; a slope breakdown in the dispersion can be seen for both cases at nearly -50meV. The dispersion for Nd−LSCO is horizontally offset for clarity, with the two solid lines as guide to the eye.

disordered stripe picture (Fig. 6.7(c), upper−right panel)[44]. This also seems to be consistent with the trend that in LSCO the nodal spectral weight is more intense than that in Nd-LSCO because the stripes in the former are dynamic while they are more static in the latter. Note that, in this picture, the nodal Fermi surface is actually a superposition of Fermi surface features from two perpendicular stripe domains; for an individual stripe domain, this Fermi surface feature can be discrete[44].

An alternative scenario to understand the two features in the stripe context is a possible coexistence of site− and bond−centered stripes[61]. Both types of stripes are compatible with neutron experiments[28, 29], and are close in energy as indicated by various calculations[62]. As shown in Fig. 6.7(c), the calculated $A(k,E_F)$ patterns for the site−centered (lower−left panel) and bond−centered stripes (lower−right panel)[61] bear a clear resemblance to the data in Fig. 6.4 (b) and Fig. 6.7 (b), respectively. It is therefore tempting to associate the 1D straight segment to site−centered stripes and the nodal Fermi surface feature to bond−centered stripes. Since these two types of stripes are different in their wave functions, it may also help explain why they show different behaviors under different measurement conditions. Moreover, the sudden slope change (or "kink") of the dispersion along the nodal direction for both Nd−LSCO and LSCO (Fig. 3(d)) is also consistent with this scenario[60, 61]. If this picture proves to be true, it would imply that, with increasing doping, bond−centered stripes are produced at the expense of site−centered stripes, and more bond−centered stripes may be generated as the stripes become more dynamic (Fig. 6.7). This seems to further suggest that the bond−centered stripes are more favorable for superconductivity than the site−centered stripes, a possibility that remains to be investigated further. We note that the above scenarios can be closely related to each other. Stripe disorder or fluctuation may naturally give rise to hole−rich and hole−poor regions as in phase separation case, particularly with the possible existence of stripe dislocations in the system. In the case of stripe fluctuation, the randomness in the stripe separations may necessarily give rise to a mixture of site−centered and bond−centered stripes.

6.5 $x = 0.22$ pure LSCO results

Finally, in this section we report results from $x = 0.22$ LSCO, overdoped sample with weak dynamic stripe ordering. The spectral weight results from this overdoped sample are very similar to the band calculations. Figure 6.8 shows the spectral weight plot integrated over a 30 meV window around the Fermi level [(a),(c)] for both geometries and simulations of the spectral weight plot for each geometry including transition matrix element effects [(b),(d)] (see below). Integrating over the narrow window of the order of the energy resolution makes it possible to obtain the spectral weight at E_F, which approximately represents the Fermi surface. The Fermi surfaces at $k_z = 0$ and π/c from the band-structure calculation for $\mathrm{La}_{2-x}M_x\mathrm{CuO}_4$ ($x = 0.2$) [63], as well as the Fermi surface from the tight-binding fit [64] are superimposed on Fig. 6.8 (a). As a whole, they well describe the global features related to the Fermi surface obtained from ARPES. In particular, looking at the nodal direction in the second BZ, they agree well with each other. The volume enclosed by the tight-binding Fermi surface is $S_{FS} \approx 0.8 \times 2\pi^2$, which satisfies Luttinger's sum rule [$S_F S = 2\pi^2(1 - x)$] within experimental accuracy.

As shown in Fig. 6.8(b), in geometry with cuts along the CuO bond direction, the nodal states in the first BZ show almost no spectral weight while those in second BZ are enhanced, consistent with the experimental data in Fig. 6.8 (a). This implies that the suppression in geometry with cuts along the CuO bond direction compared to geometry with cuts along the nodal direction is caused by matrix element effects. According to the simulation, the smaller matrix elements in the first BZ are a result of the combination of the symmetry of the $d_{x^2-y^2}$ orbital and the large out of plane component in the E-vector. The enhancement in the second BZ may be caused by the angular distribution factor of the three atomic orbitals, because they have a small emission probability for small angles when the E-vector is vertical to the surface. In geometry with cuts along the nodal direction, we can see the clear dispersion and spectral weight in the nodal state in the first BZ as shown in Fig. 6.8(c). The simulation in Fig. 6.8(d) shows an enhancement of the spectral weight in the (0,0)-(π, π) direction compared to the nodal states of the first BZ in geometry with cuts along

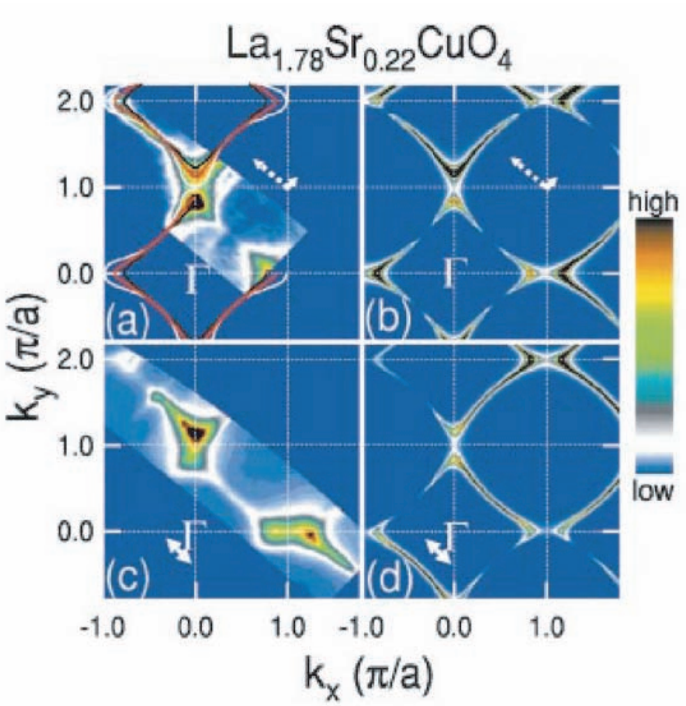

Figure 6.8: Spectral weight integrated within 30 meV of the Fermi level. White arrows designate the E vector. (a)(c); Experiment. (b)(d); Simulation. White and black curves in (a) represent the Fermi surfaces of band calculation [63] at $k_z = 0$ and π/c, respectively, and red curves represents the Fermi surface from the tight-binding fit [64]. Note that the spectral weight in the nodal direction is enhanced for geometry with cuts along the nodal direction [(c) and (d)] compared to geometry with cuts along the CuO bond direction [(a) and (b)].

the CuO bond direction, which qualitatively agrees with the experimental results.

While the overall features in the experimental results agree with the simulation as shown above, there was still a discrepancy between them regarding the spectral weight distribution near $(\pi, 0)$. The spectral weight distribution around $(\pi, 0)$ shows a relatively straight contour along the k_x direction, which is slightly narrower than that in Nd-LSCO ($|k_y| < \pi/4$)[11]. This spectral weight distribution is very similar to that of the flat band which appears below E_F for smaller x. Presumably the $(\pi, 0)$ flat band feature which exists in the optimum and underdoped regions does not completely lose its spectral weight even for $x = 0.22$ (and probably for $x = 0.3$, see data in Ref.[55]) where the saddle point is located above E_F. Therefore, the spectral weight around $(\pi, 0)$ appears as a remnant of the "flat band". In the present case, strong intensity around $(\pi, 0)$, which is not predicted by the simulation, always exists irrespective of polarization geometries, while the nodal states are strongly affected by matrix element effects. This implies an intrinsic unusual electronic structure such as stripes associated with the "flat band" feature.

As seen in Fig. 6.8, we have shown that the electronic structure of LSCO with $x = 0.22$ shows two features. One is the nodal Fermi surface which is found to be consistent with the band structure calculation. The other is the remnant flat band which gives rise to a straight segment of spectral weight near the $(\pi, 0)$ region. These two features are qualitatively similar to those observed in Nd-LSCO and LSCO with $x = 0.15$ samples in previous section [11, 65], although quantitatively the flat band effect in LSCO with $x = 0.22$ is weaker. This dual nature of the electronic structure can be explained in terms of order-disorder stripes competition [65]. The origin of the nodal state can be understood by considering strongly disordered stripes and/or weakened stripe order. In the latter case, one may begin to recover the underlying band structure. The underlying electronic structure will manifest itself stronger as the charge ordering effect becomes weaker in LSCO with $x = 0.22$.

In conclusion, we have shown the evolution of the electronic structure of the stripe phase with doping in pure and Nd-LSCO. We have shown, for the case of $x = 0.12$ Nd-LSCO, that stripes manifest themselves by confining ARPES spectral weight in 1D structures. We have also seen evidence for nodal spectral weight, which is more pronounced in dynamic stripe phase in pure-LSCO compounds. In overdoped samples the electronic structure can be fairly well explained by the homogeneous band structure calculation, although extra 1D spectral weight near $(\pi, 0)$ indicates presence of the remnant stripe order. These observations are consistent with the picture of order-disorder competition of stripes in the system.

Chapter 7

Dispersions in Bi2212 and other cuprates - observation of electron-phonon coupling.

In this chapter we report quasiparticle dispersion study in $Bi_2Sr_2CaCu_2O_8$. Unlike the linear dispersion predicted by the band calculation in a narrow energy window near E_F, the data show a sharp break in dispersion at 50 meV binding energy where the velocity changes by approximately a factor of two. This change is a signature of an energy scale that impacts quasiparticle self-energy. This break in dispersion is evident at and away from the d-wave node line, but the magnitude of the dispersion change decreases with temperature and with increasing doping. We also report the presence of this break in dispersion (kink) in other families of high temperature superconductors. Results from $\mathrm{La}_{2-x}\mathrm{Sr}_x\mathrm{CuO}_4$ and $Bi_2Sr_2CuO_6$ show the kink to have the same energy in all compounds, with ubiquitous doping and temperature dependencies. The similarity of results from different compounds leads to a unifying scenario for the kink in terms of electrons coupling with the phonons associated with the movement of the oxygen atoms. This suggests that electron-phonon coupling strongly influences the electron dynamics in the high-temperature superconductors, and must therefore be included in any microscopic theory of superconductivity.

7.1 Introduction

In a conventional metal the observation of an energy scale often provides significant insight into the physical process in the material. The most noted example is the observation of the phonon anomalies in strong coupling superconductors such as lead, which had a far-reaching impact on the understanding of the superconductivity mechanism [82, 83, 84]. For the high-temperature superconductors, a peculiar normal state property is that there appears to be no energy scale, which is often referred to as the marginal Fermi liquid behavior [17]. This behavior is highly anomalous as one would expect certain energy scales in the problem. In the theoretical context this lack of an energy scale is believed to be a key feature of a near-by quantum critical point [85, 86, 87, 88, 33, 17, 90]. In the superconducting state, on the other hand, there are energy scales observed in the cuprate superconductors, such as the superconducting gap.

With its ability to measure both the real and imaginary parts of the self-energy, $\Sigma(\omega, k)$, angle-resolved photoemission (ARPES) experiments provide a unique opportunity to further explore this issue as any relevant energy scale present will manifest itself in the quasiparticle dynamics. In the known case of electron-phonon interaction the coupling causes a kink in the dispersion and also a change in quasiparticle lifetime near the phonon energy [84]. These canonical changes reveal effects in the real and imaginary parts of the self-energy due to the electron-phonon interaction, an effect which was experimentally observed recently [14]. In this chapter we present high-resolution ARPES data from $Bi_2Sr_2CaCu_2O_8$ superconductors as a function of doping and temperature. We have observed a clear break in the quasiparticle dispersion near 50 ± 15 meV binding energy (BE), that results in a change in the quasiparticle velocity up to a factor of two or more. This effect is enhanced in the underdoped sample, and appears to persists above T_C. We also present data from $\mathrm{La}_{2-x}\mathrm{Sr}_x\mathrm{CuO}_4$ and $Bi_2Sr_2CuO_6$, where the same effect is seen. Because the electronic structure calculation [91, 92] predicts a linear dispersion in this range, this result represents an important effect in self-energy. Further, we found that this effect is present at various points of the momentum space. The ubiquity of the effect, its temperature dependence and the similarity of the energy scale in different cuprates, as well as independent observation of phonons at the kink energy scale, leave the interpretation of the kink in terms of electron-phonon coupling as the only surviving explanation.

7.2 Experiment

Angle-resolved photoemission data have been recorded at beamline 10.0.1.1 of the Advanced Light Source utilizing 22, 33 and 55 eV photon energies, in a similar set-up as we have reported recently [11]. The momentum resolution was ±0.1 degrees, which is about an order of magnitude better than our previous study of this material, making the results reported in this letter possible. The energy resolution was 14 meV. The vacuum during the measurement was better than $4 \cdot 10^{-11}$ torr. The pure and Pb-$Bi_2Sr_2CaCu_2O_8$, $\mathrm{La}_{2-x}\mathrm{Sr}_x\mathrm{CuO}_4$ and pure and Pb-$Bi_2Sr_2Cu_1O_4$ samples were grown using floating-zone method. The single crystalline samples were oriented and cleaved *in situ* at low temperature.

7.3 $Bi_2Sr_2CaCu_2O_8$ results

Figure 7.1(a) shows raw ARPES data collected along the $(0,0)$ to (π,π) (nodal) direction of the Brillouin zone from the slightly OD $Bi_2Sr_2CaCu_2O_8$ (T_C=91 K) sample at 30K. In Fig. 7.1(b) we plot the dispersion determined from the fits to the momentum distribution curves (MDCs) - angle scans at a constant binding energy [7]. MDC plots show a peak on a constant background that can be fitted very well with a simple Lorentzian, as illustrated in the inset (b2) of Fig. 7.1. Error bars in $k_{\|}$ and energy are determined from the fit uncertainty and energy resolution respectively. The data clearly show a feature dispersing towards the Fermi energy with an obvious break in the slope near 50 meV BE. A similar break in the dispersion was also observed at photon energies 22 and 55 eV. Data for all three photon energies are plotted in the inset (b1) of Fig. 7.1. To describe the dispersion in the range of (-200 to 0 meV) one

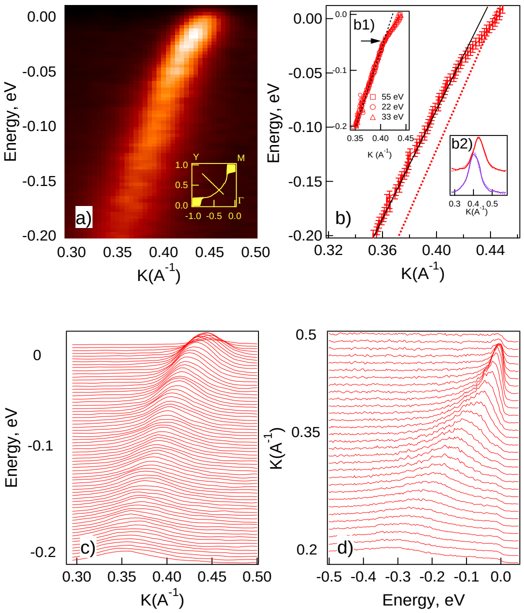

Figure 7.1: Panel (a) shows raw data obtained using Scienta angle mode for slightly overdoped (T_c=91K) $Bi_2Sr_2CaCu_2O_8$ along nodal direction ($\Gamma - Y$) of the BZ at 33 eV photon energy. The position of the cut is given in the inset. Panel (b) shows the dispersion of the quasiparticle determined from the MDC fits of the data in panel (a). The theoretical dispersion from LDA calculation is also included (dotted straight line). Energy is given relative to the Fermi energy. Inset (b1) shows the dispersion along this direction obtained at 22, 33, and 55 eV. Inset (b2) shows MDC's at 16 (blue) and 55 (red) meV BE. Dashed lines represent Lorenzian fits. Panels (c) and (d) show raw MDCs and EDCs respectively.

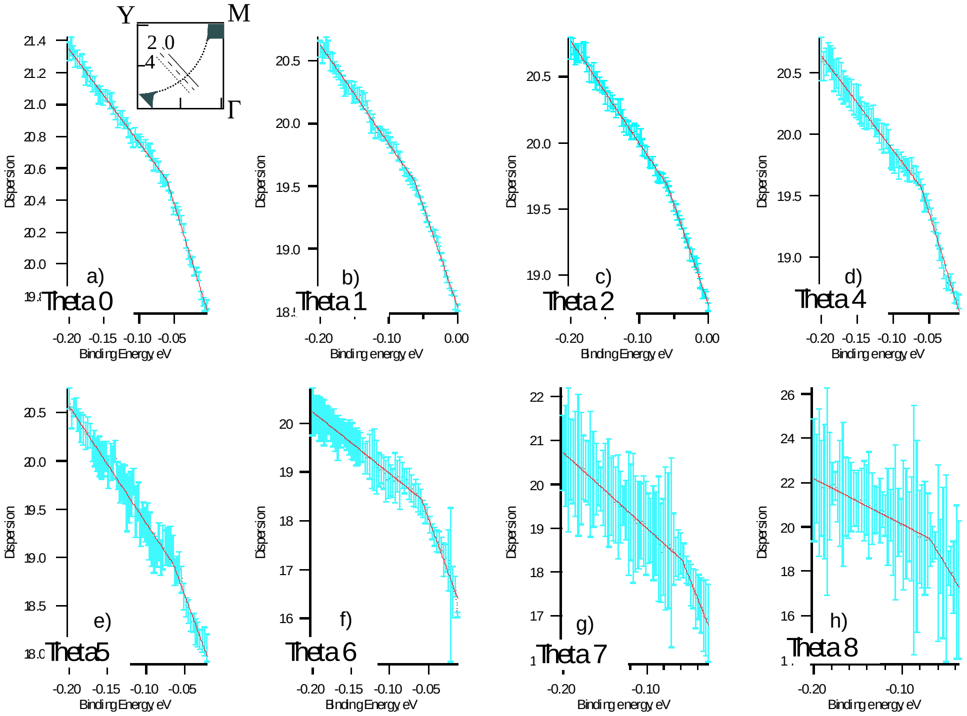

Figure 7.2: This figure shows the MDC-derived dispersions for the underdoped $Bi_2Sr_2CaCu_2O_8$ ($T_c = 84K$) for cuts parallel to $\Gamma - Y$ direction vs the momentum. Inset in panel a) shows the direction of the cuts in the brilluoin zone.

needs only two straight lines intersecting near 50 meV BE. This behavior is clearly different from what one expects from the local density approximation (LDA) or any other electronic structure calculation where a linear dispersion in this energy range is predicted. Raw MDCs are plotted in Fig. 7.1(c), while raw energy distribution curves (EDCs) are plotted in Fig 7.1(d) for reference.

We present in Fig. 7.2 (a)-(h) the dispersions obtained from different cuts parallel to the $(0, 0)$ to (π, π) direction across the Fermi surface for the UD $Bi_2Sr_2CaCu_2O_8$ ($T_C = 84$ K) sample at 20K. Within the error bars, the data are again well described by two straight lines with a break near 50 meV BE. The energy position of the break is constant throughout the BZ within the experimental uncertainty, despite the opening of the gap. Figure 7.3 shows the locations in the two-dimensional zone where the break is experimentally observed. It demonstrates that the effect is present in all directions.

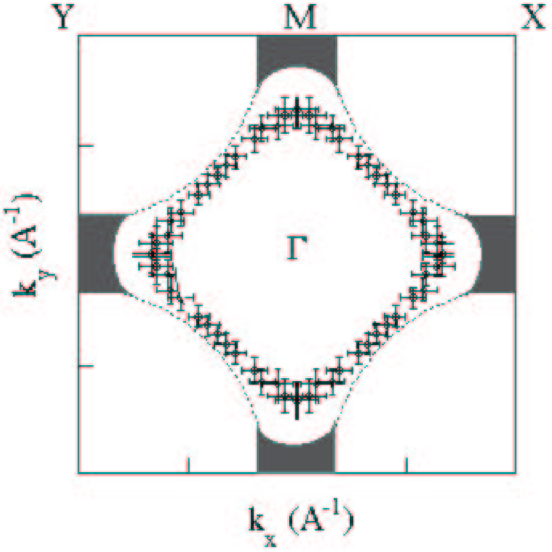

Figure 7.3: Kink position as a function of $\vec{k}_x$ and $\vec{k}_y$ is plotted in the BZ (circles). Eight-fold symmetrization procedure was applied. Error bars reflect uncertainty in kink position from the MDC fits and the experimental angular resolution perpendicular to the scan direction. Fermi surface is plotted for reference (dashed lines).

We have investigated this effect in $Bi_2Sr_2CaCu_2O_8$ as a function of doping and temperature. The effect appears to be stronger in the underdoped sample. The change of the quasiparticle velocity at the break is different, which can be illustrated by data along the $(0, 0)$ to (π, π) direction. For the underdoped sample, the quasiparticle velocity determined from the MDC fits shows a break from 3.6 $eV\AA$ at higher binding energies to 1.5 $eV\AA$ near the Fermi level. The respective velocities for the optimally doped samples are 2.6 and 1.6 $eV\AA$. These results have a significant error bar. In figure 7.2 we plot dispersions as a function of angle. The change of velocities with angle is up to $1eV\AA$ per degree. Although our angular resolution is $\pm.1$ degrees, the error in absolute alignment is ± 1 degree, which is the main source of uncertainty. However, for both dopings we sampled over the whole Brillouin zone. This gives us internal reference point for alignment, since velocities decrease as we go away from nodal direction. We have measured two overdoped samples at three photon energies. The velocities we determined for both samples for low binding energy part are within $0.1eV\AA$. There's no detectable change in velocity with doping or photon energy in this

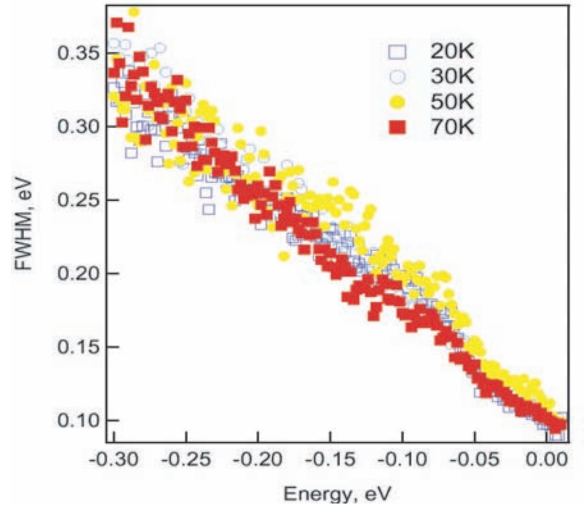

Figure 7.4: This figure shows the MDC-derived widths for slightly overdoped Bi2212 ($T_C = 91$K) for cuts along $\Gamma - Y$ direction at different temperatures. Energy scale is given my multiplying the widths in K by constant bare velocity.

region. Other groups reported $1.14 eV\AA$[7] and $1.6 eV\AA$ [95] for the low binding energy velocities. For the high energy part the difference with samples is also negligible. For the sample we measured at three photon energies we find $2.6 \pm .1 eV\AA$. For a sample of the same doping other experiment gave $2.5 eV\AA$.

In general, one expects to see complementary effects in dispersion and EDC and MDC peak widths as they reflect the quasiparticle self-energy. The self-energy can be easily extracted from an ARPES experiment if $Im\Sigma(\vec{k}, E)$ is much smaller than the energy. In high T_c 's extracting the self energy from ARPES is harder because the EDC peak energy is comparable to the peak width for $E \geq 30$ meV binding energy. However, assuming weak k dependence of the $Im\Sigma(\vec{k}, E)$ [17], the deviation of the MDC dispersion from the LDA calculation gives real part of the self energy and the MDC peak widths represent imaginary part [93].

The effect in the MDC widths is very hard to see, because finite experimental resolution has dramatic effect of smoothing the MDC width curve. We have performed a few scans with extremely high resolution ($< 7\ meV$). The resultant MDC widths are shown in Fig.7.3. The corresponding energy is given by the momentum width of the MDC peak multiplied by the constant bare velocity, approximated by the high

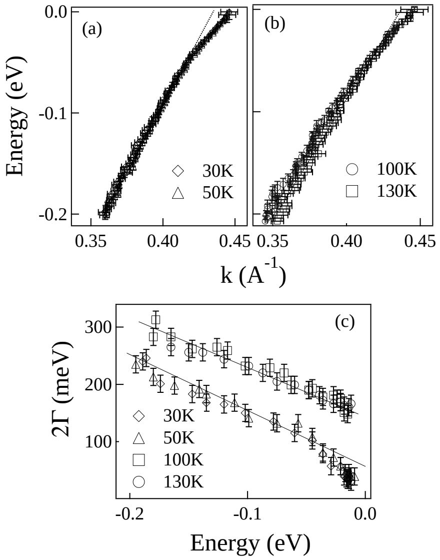

Figure 7.5: In Panel (a) dispersion in the slightly overdoped $Bi_2Sr_2CaCu_2O_8$ (T_c $= 91K$) along nodal direction $(\Gamma - Y)$ of the BZ below T_c is reported. The dotted line represents linear fit into the high energy part of the dispersion. Energy is given relative to Fermi energy. In Panel (b) dispersion above T_c is reported for the same sample. Dotted line represents linear fit into the high energy part of the dispersion. Panel (c) shows EDC derived quasiparticle widths of the spectral feature as function of binding energy. High temperature data is shifted up by 100 meV for clarity.

energy velocity. One clearly sees a drop in scattering rate at the characteristic energy scale. This drop corresponds well to the IR reflectivity data [94].

The dispersions determined from the OD $Bi_2Sr_2CaCu_2O_8$(T_C=91 K) sample above T_c along the $(0, 0)$ to (π, π) $(\Gamma - Y)$ direction are shown in Fig. 7.5(a), while the low temperature dispersions ($T < T_c$) are reported in Fig. 7.5(b) . The dispersions exhibit the same break structure as contrasted to the straight line. The change of dispersion is more difficult to see in the high temperature data compared to low temperature data, but a weak residual effect still appears to be present. In Fig. 7.5(c)we show the temperature dependence of the EDC width. We see a clear change in 2Γ around 50 ± 15 meV in the low temperature data, but the effect is harder to see above T_c, similar to earlier reports [7, 95, 96].

7.4 Ubiquity of the effect in cuprates

To identify the nature of the observed kink in $Bi_2Sr_2CaCu_2O_8$ we performed extensive study of different high temperature superconducting cuprates. The top panels of figure 7.6 reports the MDC derived dispersions along the $(0, 0) - (\pi, \pi)$ direction for LSCO (panel a) and Bi2212 (panel b) superconducting state and for Pb-Bi2201 normal state (panel c) vs the rescaled momentum, k', defined by normalizing to one the momentum k relative to the Fermi momentum k_F, $(k - k_F)$, at the binding energy E=170meV. A "kink" in the dispersion around 50-80meV, highlighted by thick arrows in the figure, is the many-body effect of interest. The direct comparison suggests a similar phenomenon in different systems (although details differ) and at different doping, with the effect getting stronger in the underdoped region. These results put a strong constraint on the nature of the effect. The similar energy scale of the excitation (50-80 meV) in systems with very different gap energy, ranging from (10-20 meV) for LSCO and Bi2201, to (30-50meV) for Bi2212, rules out the superconducting gap as the origin. The data also rule out the proposed explanation [97] in terms of coupling with the magnetic mode at 41meV, because of its temperature dependence and its ubiquity. The phenomenon is observed in LSCO where the magnetic mode does not exist. It is also observed well above the transition temperature in all cases but the magnetic mode sets in at Tc for optimal and overdoped samples[98] (e.g. the 30K data from overdoped Pb-Bi2201 are measured at six times Tc). These considerations, based on direct experimental evidences, leave phonons as the only possible candidate.

The phonon interpretation receives very strong support from a direct comparison between photoemission results and neutron scattering data on LSCO. As shown by the red arrow and the shaded area in Fig. 7.6a, the energy of the zone boundary in-plane oxygen stretching longitudinal optical (LO) phonon, identified by neutron as being strongly coupled to charge [99, 100], coincides with the "kink" energy in our data baring minor correction with the small superconducting gap of 10meV. We identify this mode as the highest energy phonon that strongly contributes to the ARPES data. However, other phonon contribution should be considered as well, for example the apical mode [59], related with the in plane oxygen-stretching mode. Additional

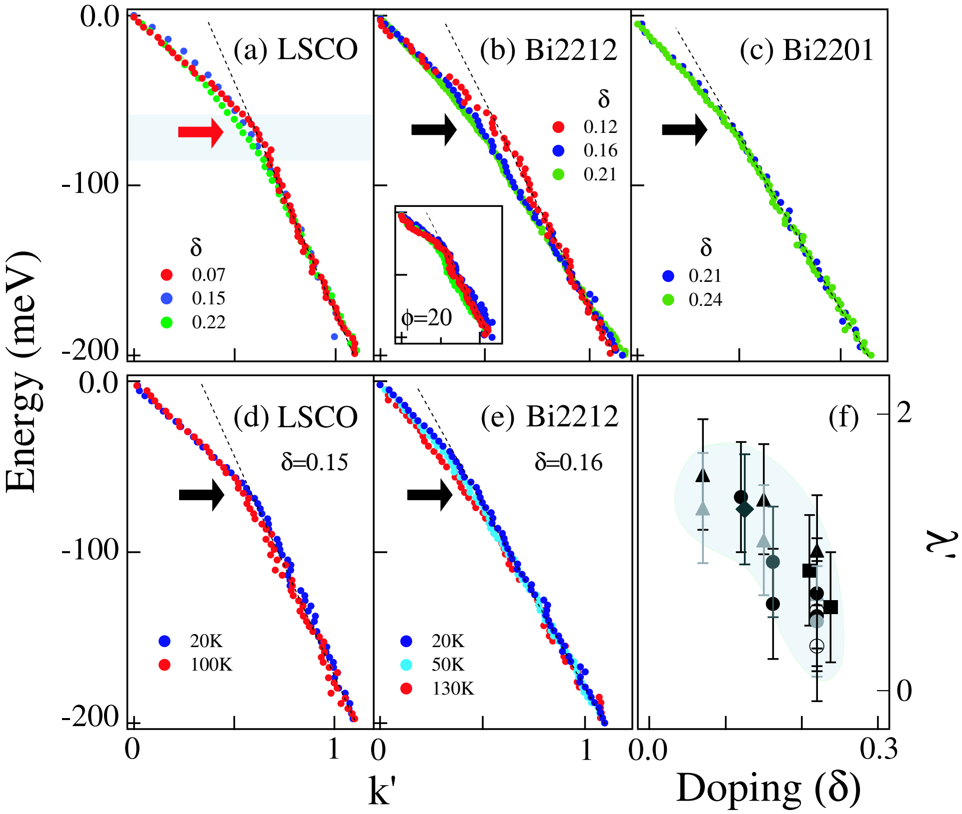

Figure 7.6: Top panels are plots of the dispersion (derived from the momentum distribution curves) along (0, 0)- (π, π) (except panel b inset, which is off this line) versus the rescaled momentum k' for different samples and at different doping. Panels a) to c) show doping(δ) dependence of LSCO (at 20K; a), Bi2212 (superconducting state, 20K; b) and Pb-Bi2201 (normal state, 30K; c). Dotted lines are guides to the eye. The kink position in a) is compared with the phonon energy at q=(π, 0) (thick red arrow) and the phonon width and dispersion (shaded area) from neutron data [99]. The doping was determined from the Tc vs doping universal curve. Inset in b) shows dispersions off the (0, 0)- (π, π) direction, showing also a sharpening of the kink on moving away from the nodal direction. The black arrows indicate the position of the kink in the dispersions. Panels d) and e) show temperature dependence of the dispersions for LSCO (d, optimally doped) and Bi2221 (e, optimally doped). Panel f) shows doping dependence of λ' (see text) along the (0, 0)- (π, π) direction as a function of doping. Data are shown for LSCO (filled triangles) and Nd-LSCO (1/8 doping; filled diamonds), Pb-Bi2201 (filled squares) and Bi2212 (filled circles, in the first Brillouin zone, and unfilled circles in the second zone). The different shadings represent data obtained in different experimental runs. Blue area is a guide to the eyes.

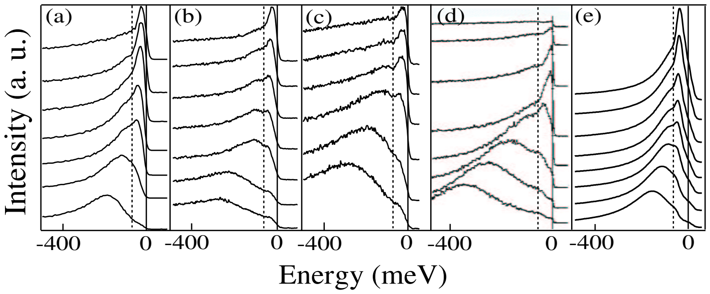

Figure 7.7: Raw energy distribution curves (EDCs) along the (0, 0) to (π, π) direction for the overdoped Pb-Bi2212 (Tc=70K) are shown in panel a), for optimally doped Bi2212 (Tc=91K) in panel b) and for underdoped Bi2212 (Tc=84K) in panel c). In panel d) raw EDCs for the Be(0001) surface are shown [13]. In panel e) EDCs of simulated spectra, obtained in the simple case of an isotropic coupling to a single phonon mode are shown. The straight vertical line highlights the zero energy position and a dashed line highlights the approximate "dip" position, which is related to known phonon energy [99] (see text).

support to the phonon scenario comes also from a temperature dependence analysis. In the lower panel of Fig. 7.6 we report the evolution of the kink above and below the transition temperature for LSCO (Fig. 1d) and Bi2212 (Fig. 1e). In both cases the kink persists clearly above the transition temperature as expected in the case of el-ph interaction, however a thermal broadening is present.

Fig. 7.7 a-c compares energy distribution curve (EDC) data of Bi2212 along $(0,0)-(\pi,\pi)$, directions (panel a-c) at different dopings, with that of Be (0001) surface state [13, 101] (Fig. 7.7d) -in which the el-ph interaction is known to be strong - and with simulated spectra (Fig. 7.7e). A strong similarity among the raw spectra can be observed. In the case of Be, the 65meV phonon sets a scale below which a sharp quasiparticle is possible. This leads to a "dip" or "break" in the spectra near the phonon energy, indicated by the vertical dashed line. This feature is well reproduced in the simple simulation, where a quasiparticle is isotropically coupled to a collective mode near 70meV [84, 97]. The Bi2212 data show also a clear resemblance, with a $(\pi, 0)$ LO-phonon near 55 meV [100], but pushed up by the superconducting gap. All the data suggest that there is an energy scale in the problem close to expected phonon frequency. Therefore, the striking similarity between Bi2212 data and that of a known phonon case strongly supports the phonon explanation.

7.5 Discussion

Although above experimental findings point towards phonons as the only possible scenario, some literature needs to be addressed. The kink in the dispersion along the (π, π) direction and the dip in the EDCs near $(\pi, 0)$ has been attributed [97] to the magnetic mode of 41 meV [98]. Comparing the doping dependence of the energy difference between the dip and the superconducting gap in photoemission data, with that of the magnetic mode in neutron data, a definitive proof for the magnetic mode as the origin of the "peak-dip-hump" structure has been claimed [102]. On the other hand, it has been argued for the absence of an energy scale in the problem [7] and the kink in the dispersion was overlooked [7]. The curving in the normal state dispersion has been attributed to the marginal Fermi liquid (MFL) self-energy [17], and the presence of a sharp kink below Tc to coupling to the (π, π) magnetic mode [103]. Apart from its incompatibility with our data, the magnetic mode scenario has serious weaknesses. First, the mode contains only few percent of the total spin fluctuation spectral weight [104], unlikely an explanation for the very large change seen in EDC spectra above and below Tc. Second, the electronic model is difficult to implement self-consistently as the mode will be altered by the interaction with electrons[97]. Third, the magnetic mode calculation claims to reproduce the experimental data that yield a huge change of the velocity ratio near $(\pi, 0)$ region[97]. As shown in [105], the superstructure complicated the data near $(\pi, 0)$ region in pure Bi2212 sample used by previous study [106], and in superstructure free Pb-Bi2212 the change in velocity near $(\pi, 0)$ is small.

Our data and the above discussion rule out the magnetic mode as a possible scenario, and this makes also the MFL plus magnetic mode interpretation an unnatural explanation for the data. Furthermore, some of the normal state dispersion, for example the 7 percet underdoped LSCO (fig. 1a) measured at Tc where the kink is sharper, cannot be fit within the MFL approach, even with an arbitrary choice of parameters.

If the 7 percent LSCO data can only be explained by coupling to phonons, it is likely that a similar effect, observed at higher doping and temperatures, requires the same cause. Finally, this attempt to attribute the "kink" in the dispersion, occurring at the same energy above and below Tc to two different origins is not consistent with the data in Fig. 1d and Fig. 1e where one sees that the effect washes out gradually with temperature. The phonon model can explain all the aspects of the data attributed to the magnetic mode in a more natural way (N. Nagaosa et al., personal communication). This approach has the added advantage of not suffering from the tiny spectral weight and the self-consistency issue present in the magnetic mode calculation. The phonon picture naturally explains the gradual temperature evolution observed in the MDC derived dispersions.

Although el-ph interaction provides the only interpretation consistent with overall body of data, a few caveats needs to be pointed out. Standard theory of el-ph coupling would produce a drop in resistivity at phonon frequency Ω, or a saturation above a temperature $T \approx 0.3 - 0.5\Omega$. The drop at Ω is observed, although it was given an alternative interpretation [107]. The temperature dependence of the resistivity shows a complex doping dependence, with a saturation seen in underdoped regime but not near optimal and overdoped regime [107]. An understanding of this complex behavior requires going beyond the simple Fermi liquid theory, but is not incompatible with the presence of el-ph coupling [108]. The lack of resistivity saturation is also seen in doped C60 compound where the el-ph interaction is very strong[108]. An improved theory needs to consider the strong electron-electron interaction, the pseudogap[109], and vertex correction that suppress the large momentum transfer scatterings [110], making phonons hard to detect by resistivity experiments. Finally, we stress that el-ph interaction in strongly correlated materials is a largely unexploited topic, and we hope that our finding can stimulate more theoretical work.

Chapter 8

Study of scattering rate anisotropy at the Fermi surface of Bi2212.

The question of the anisotropy of the electron scattering in high temperature superconductors is investigated using high resolution angle resolved photoemission data from Pb doped $Bi_2Sr_2CaCu_2O_8$ (Bi2212) with suppressed superstructure. The scattering rate of low energy electrons along two pieces of the Fermi surface is measured, and no increase of scattering towards the anti-node $(\pi, 0)$ point is observed. The results put a limit on the effects of (π, π) scattering on the electronic structure of superconducting cuprates.

8.1 Introduction

The angular dependence of the "quasiparticle" width along the Fermi surface is a very sensitive test of the scattering process in cuprates, which is ultimately important to understand its superconducting mechanism. In the underdoped regime [111, 112, 113, 102] it has been shown in many systems that the peak width is in general broader than the overdoped counterpart, and the spectra near $(\pi, 0)$ is particularly broad. This anisotropy is generally attributed to spin scattering centered at (π, π), that connects $(\pi, 0)$ to $(0, \pi)$ points in the Brillouin zone. The (π, π) scattering and its suppression of the $(\pi, 0)$ spectra exhibit itself most strongly in the undoped insulator [114]. There is a general agreement that insulating behavior in the undoped system results from strong electron-electron correlation effect which is also intimately related to magnetic interactions peaked at $q = (\pi, \pi)$. Hence, an anisotropy in peak width which increases towards $(\pi, 0)$ is a hallmark of $q = (\pi, \pi)$ antiferromagnetic interaction.

The scattering anisotropy in overdoped sample, on the other hand, has hardly been studied. Shen and Schrieffer noted, that the anisotropy in the overdoped $Bi_2Sr_2CaCu_2O_8$ (still with T_C as high as 80K) is more or less gone [111]. So far, no reports on other materials are available. To further quantify these points, one has to overcome two technical issues that complicate the $(\pi, 0)$ spectra. One is the superstructure, and the other is bilayer splitting [115, 116, 117].

In this paper we present the results of scattering rate measurements along the two bilayer-resolved pieces of the Fermi surface in overdoped Pb-doped Bi2212 that suppresses the superstructure. We performed angle-resolved photoemission (ARPES) measurements above and well below the superconducting transition temperature. We measured the widths of the quasiparticle peaks along the resolved Fermi surface pieces. We found that the scattering rate actually reaches a minimum near $(\pi, 0)$. This strongly suggests, that any magnetic excitations near (π, π) would have minimal effect on the quasiparticle scattering. This finding in a sample with T_C as high as 70K puts a constrain on theory. In particular, it shows that the (π, π) magnetic resonance can not be the driving force for pairing, consistent with [105].

8.2 Experiment

ARPES data have been recorded at beamline 10.0.1.1 of the Advanced Light Source (ALS) utilizing 22 eV photon energy in $4 \cdot 10^{-11}$ $Torr$ or better vacuum. The sample was kept in the fixed position relative to the beam polarization, and the analyzer was rotated. The beam polarization was in the sample plane perpendicular to the $\Gamma - Y$ direction, with beam nearly at grazing incidence with the sample surface. We used a Scienta SES 200 analyzer in the angle mode, where cuts parallel to $\Gamma - Y$ direction were carried out. For 22 eV the momentum resolutions were respectively $\pm 0.004 \mathring{A}^{-1}$ and $\pm 0.011 \mathring{A}^{-1}$, and the energy resolution was 16 meV. The overdoped Pb-doped

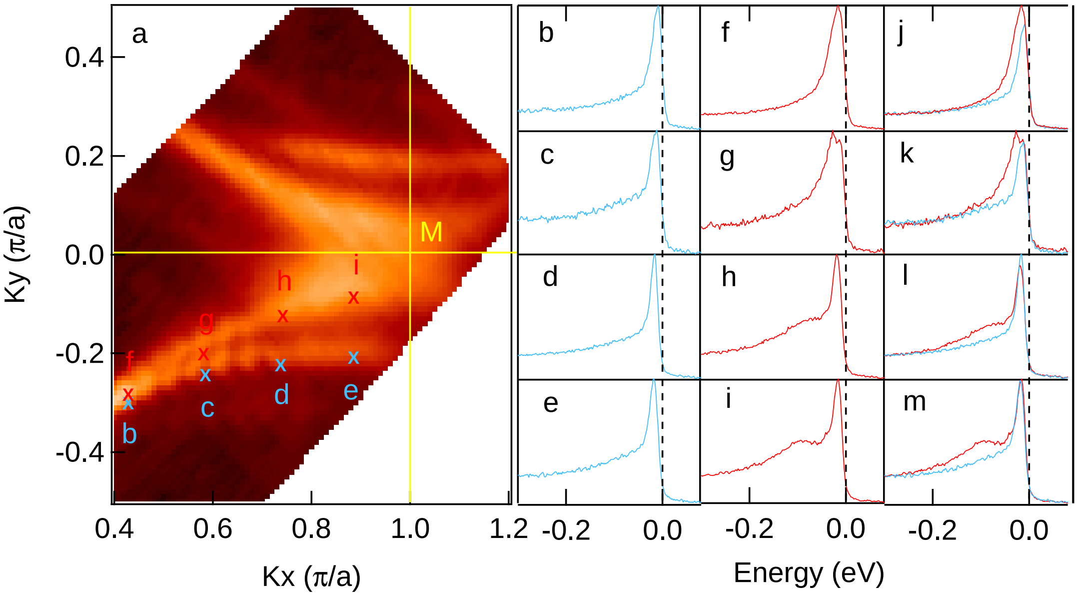

Figure 8.1: In this Figure data collected at 20 K is shown. Panel a) shows the spectral intensity at the Fermi level. Crosses indicate locations in momentum space of the cuts shown in panels b) - i). Spectra b)-e) (blue) come from the bonding band, while spectra f)-i) come from the anti-bonding band. In panels j)-m) we show together spectra b) and f); c) and g); d) and h) and e) and i) respectfully.

Bi2212 ($Tc = 70K$) was grown using the floating-zone method. The single crystalline samples were oriented by using Laue diffraction ex situ and cleaved in situ in vacuum at the measurement temperature. The Fermi energy was obtained from the Energy Distribution Curves (EDCs) of polycrystalline Au.

8.3 Results and Discussion

In panel a) of Fig. 8.1 we show the photoemission intensity map taken at the Fermi level at 20K, well below the superconducting transition temperature of 70K. One can clearly see two Fermi surface pieces, which coincide along the diagonal direction $((0,0) - (1,1)$ in the units of (π/a) and separate significantly at $(1,0)$. As shown

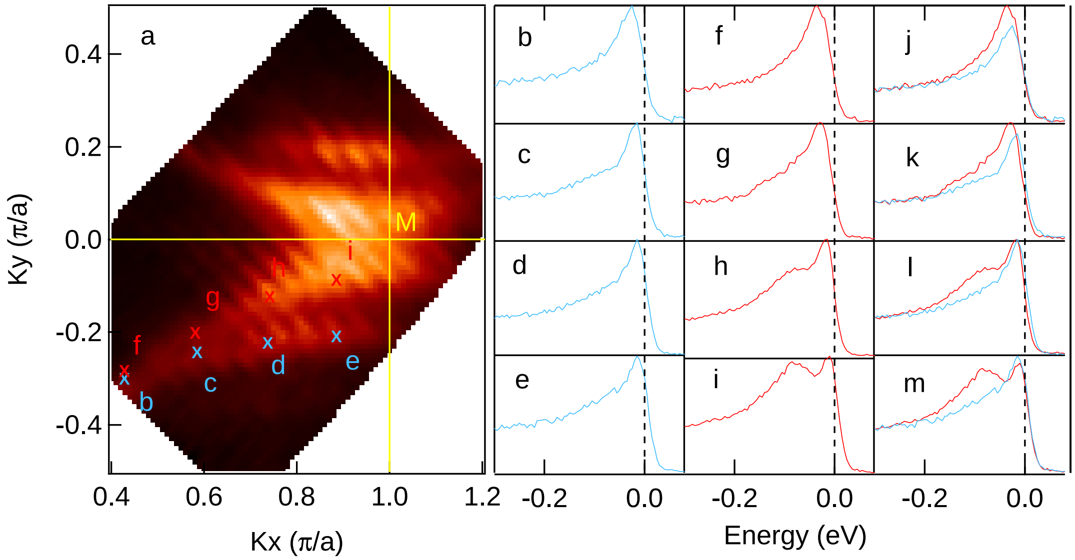

Figure 8.2: In this Figure data collected at 20 K is shown. Panel a) shows the spectral intensity at the Fermi level. Crosses indicate locations in momentum space of the cuts shown in panels b) - i). Spectra b)-e) (blue) come from the bonding band, while spectra f)-i) come from the anti-bonding band. In panels j)-m) we show together spectra b) and f); c) and g); d) and h) and e) and i) respectfully.

before, this separation, observed most clearly with 22 eV and 44 eV photons, results from the interaction between two adjacent CuO_2 planes [117]. The superstructure in our data is significantly suppressed due to Pb doping, simplifying analysis in the critical antinodal region (M point).

Crosses on the map in panel a) indicate momentum-space points where spectra shown in panels b)-i) were taken. Panels b)-e) show the spectra (in blue) taken along the bonding Fermi surface. One sees, that on going along the bonding Fermi surface spectra does not change significantly. The width of the peak appears almost constant independent of the position in momentum space.

Panels f)-i) show the spectra (red) taken along the anti-bonding Fermi surface. Here the structure is more complex, but it is clear that it can be reproduced by two features: a constant peak at the Fermi level and a feature that disperses to higher binding energy as one moves from $(0,0)-(\pi,-\pi)$ direction toward $(0,0)-(\pi,0)$

direction. We interpret the low energy peak as the one from the anti-bonding band at the Fermi surface, and the dispersive high energy feature as resulting from the bonding band, as discussed earlier.

It is interesting to note that the low energy anti-bonding band peak is very similar to the bonding band peak at the Fermi surface. We illustrate this point in panels j)-m), where we plot data from the bonding and anti-bonding Fermi surfaces on the same graph. We see that the low energy signal is similar for both Fermi surfaces, and the anti-bonding result can be represented as the bonding result plus higher energy peak.

In Fig. 8.2 we plot the data at 100K, well above the superconducting transition temperature of 70K. Again, panel a) shows the intensity map at the Fermi level, while panels b)-i) show individual spectra along the two Fermi surfaces. Similar to the results of Fig. 1 the bonding band gives rise to simple one-peak structure at the Fermi level. The anti-bonding Fermi surface results can be represented as the sum of the low energy peak, similar to the peak from the bonding band, and dispersing higher energy feature, as illustrated in panels j)-m).

To quantify the above discussion we employ a simple procedure to fit the experimental data. We model the spectra near the Fermi surface from the antibonding band by the sum of a Lorentzian peak to represent $A(\vec{k}, \omega)$ and a smooth function to represent inelastically scattered electrons (the results are insensitive to the form of the smooth function - we used parabola here, but linear and other functions work as well). This sum is then multiplied by the resolution-broadened Fermi function, where the chemical potential is a fitting parameter. A constant is added to the result to represent the signal from higher order photons.

To fit the spectra near the Fermi surface for the spectra with both bands we simply use two Lorentzian peaks for the two bands visible in the spectra. The results of the fit are represented in Fig. 8.3. We see that the fit is quite good even for the double peak structure, despite the fact that the high energy Lorentzian width is significantly larger than resolution and there's no good reason to believe $A(\vec{k}, \omega)$ to be Lorentzian in energy.

We use the EDC widths to determine the scattering rate. It is reasonable in this

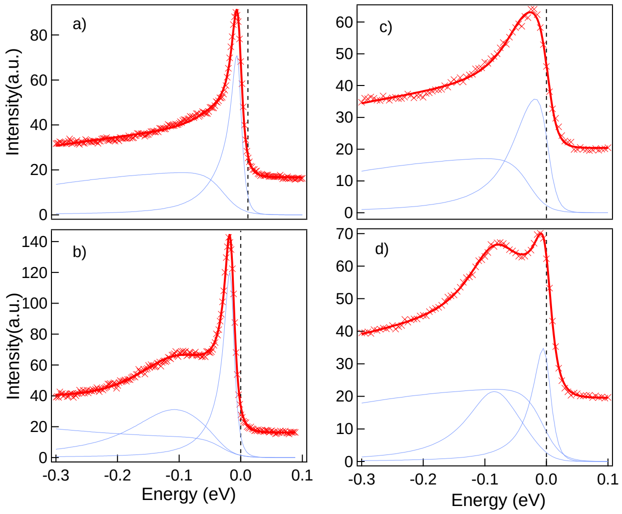

Figure 8.3: Panel a) shows the data at the bonding band Fermi surface in the superconducting state (red crosses)together with the fit results (solid red line). Blue lines represent components of the fit - lorentzian peak and parabolic background multiplied by the Fermi function. Panel b) shows the data at the anti-bonding band Fermi surface in the superconducting state. Similarly to panel a) blue lines represent components of the fit - two Lorentzian peaks and parabolic background multiplied by the Fermi function. Panels c) and d) represent normal state data from bonding and anti-bonding Fermi surfaces respectfully. Again, raw data is given by red crosses, fit components are shown in blue, and the resultant fit function by a solid red line.

case, because the peaks are relatively sharp and we are mainly intersted in relative change with momenta, not necessarily the absolute value. To determine the peak widths along the Fermi surface we have to identify the Fermi surface location in k space first. While it was a fairly easy task in the days when angular uncertainty was over 1 degree, it is much harder now, because the decreased angular uncertainty due to improved resolution meanse there usually is a large number of spectra in finite angular window that have their leading edges at or above the chemical potential, and the lineshapes of these spectra are quite different. The absolutely correct determination of the Fermi surface depends on the specifics of the spectral function and matrix elements, which we do not know at the moment. So it is important to develop the single consistent method, similar to the old leading edge method, to select the Fermi surface.

In this chapter we take the Fermi surface to be the continuum of momentum space locations where the signal intensity at the chemical potential is largest. This should be the case for the Fermi liquid, and in a modern experiment with the data collected every $2meV$ in energy it is very reliable method even for the fairly flat $Bi_2Sr_2CaCu_2O_8$ bands. For the superconducting state we found the surface determined this way to coincide well with the normal state Fermi surface.

We present the widths of the peaks in Fig. 8.4, panel a). We see a clear trend, universal for both bands and temperatures - the decrease in the peak width on approaching the $\phi = 0$ line ($\Gamma - M$ direction). The widths for high temperature are plotted with open symbols, and the widths for the low temperature are plotted with solid symbols. Data from the bonding band is plotted in blue, while the data from antibonding band is plotted in red. We see that the widths from these two different bands are the same in the angular range where both bands are well defined. Beyond the ± 14 degrees lines the bands are very close together, and the data points acquire large error bars, mostly coming from identifying the correct Fermi surface. Typically it is impossible to clearly separate the two bands for ϕ beyond ± 20 degrees. The scatter in the data in this angular region is the measure of uncertainty in the width size.

We have performed peak width measurements in two different Brillouin zone quadrants. The data in panel a) of Fig. 8.4 comes from quadrant I, $Ky = -\pi$ to $Ky = 0$ (negative ϕ), and quadrant II, $Ky = 0$ to $Ky = \pi$, (positive ϕ) (see panel b) of Fig. 8.4). The agreement in the data from the two quadrants shows that the effects of remnant superstructure on the peak widths is negligible, because the superstructure effects are very different in the two quadrants.

Another important issue to consider is the effect of non uniform angular acceptance of each scan. As explained in the *Experiment* part of this chapter, angular resolution along the scan direction (parallel to $(0,0) - (\pi, -\pi)$) is almost a factor of 3 less than the resolution perpendicular to scan direction. The effect of this nonuniformity, as the cut direction relative to the Fermi surface changes, has to be addressed. From the experimental point of view we address this point by analyzing data from the two different quadrants. The scan direction always remained parallel to $(0,0) - (\pi, -\pi)$

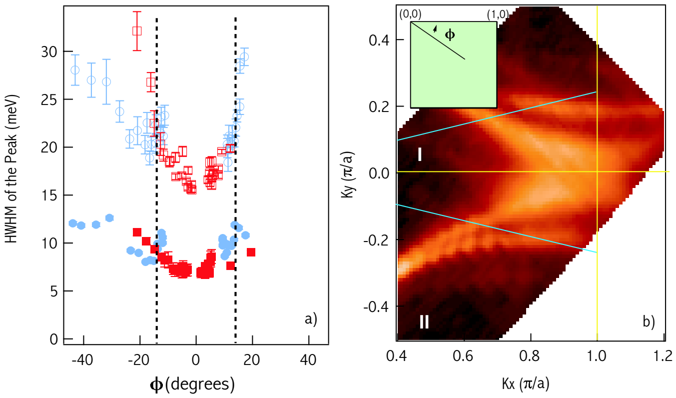

Figure 8.4: Panel a) shows the quasiparticle widths at the Fermi surface determined by the fitting procedure as a function of angle ϕ. Filled symbols correspond to the superconducting state, while empty symbols represent normal state. Red squares show the widths determined from the anti-bonding band and blue circles show data from the bonding band. Panel b) shows the image of the intensity at $12meV$ binding energy in the superconducting state. Blue lines represent the region outlined by dashed lines in panel a). Quadrants I and II are marked. Inset in panel b) explains the angular notation.

line. Let us consider two equivalent points in quadrants I and II (points mirror reflected with respect to $K_Y = 0$ line). Both points were detected with large angular acceptance window along the $(0,0) - (\pi,\pi)$ line and small acceptance window along the $(0,0) - (\pi,-\pi)$ line. However the bands in quadrant II are mirror images of the bands from quadrant I with respect to $K_Y = 0$ mirror plane. It means, that data from the second quadrant was taken with angular acceptance function rotated 90 degrees with respect to the band structure. The fact that the results from the two quadrants are the same implies that the effect of angular acceptance in the data is small.

We can quantify these results theoretically. The broadening of the peak due to finite angular resolution in the first approximation is given by

$\delta E = \sqrt{(v_{\parallel} * \delta K_{\parallel})^2 + (v_{\perp} * \delta K_{\perp})^2}$,

where the two directions are along the scan ($\|$) and perpendicular ($\perp$) to the scan. In the case of $Bi_2Sr_2CaCu_2O_8$ Fermi velocity goes from $1 - 2eV\mathring{A}$ along the node to $0.6 - 0.7eV\mathring{A}$ near the $(\pi, 0)$ point. The Fermi velocity is the largest possible velocity projection for the peaks at the Fermi surface. When the scan is taken perpendicular to the Fermi surface, as in the case of $(0,0)-(\pi,-\pi)$ scan, $v_{\|}$ is given by the Fermi velocity and $v_{\perp}$ is equal to zero. Thus, for the $(0,0)-(\pi,-\pi)$ scan, we get the contribution to the peak width from the angular resolution of $\pm 4-8meV$.

We can extract the $v_{\|}$ and $v_{\perp}$ directly from the data. We find, that the largest contribution to $v_{\perp}$ comes near the $(\pi,0)$ point and is equal to $0.5eV\mathring{A}$. This translates into $\pm(6-7)meV$ contribution to the peak width, largest along the entire Fermi surface from the $v_{\perp}$. At the same time, the contribution to $v_{\|}$ on going from $\phi=-45$ to $\phi=0$ steadily decreases, and $v_{\|}$ contribution is less than $\pm 4meV$ for $\phi>-20$.

Of particular interest to us is the region in the range ± 14 degrees from the $\Gamma-M$ line, shown by dashed lines in panel a) and by blue lines in panel b). In this region the two bands are well separated and the fitting procedure works very well. Further, in this region the broadening of the peaks due to the angular acceptance function is slowly increasing on approaching $(\pi,0)$ from $\pm 0.07meV$ at $\phi=-14$ to $\pm 0.08meV$ near $(\pi,0)$. The main body of data in this ϕ range comes from the antibonding band (two peak spectra). One clearly sees decrease of scattering rate on approaching the anti-nodal $(\pi,0)$ point. Results for both temperatures are consistent, and the scatter in the data is minimal. Away from ± 14 degrees region results are less clear, because the bands come close together and the fits become less reliable. However, the fits in the nodal direction, where band separation is zero, show that there's no dramatic scattering rate decrease in that region.

The unusual decrease in the peak widths on approaching the $(\pi,0)$ point demonstrates negligible effects of the $q=(\pi,\pi)$ scattering, because (π,π) scattering would lead to an increase in the widths at $(\pi,0)$. Further, no noticeable change in the anisotropic scattering rate upon the superconducting transition is observed as demonstrated by the agreement between $T=20K$ data and $T=100K$ data.

Anistropic inelastic spin scattering, known as magnetic mode, was observed by neutron scattering measurements in several families of high temperature superconductors [50, 118, 119, 120, 121]. Some groups interpreted ARPES spectral features even in overdoped samples as resulting from the effect of the mode on the electronic structure [103, 106]. This in turn led them to explore the possibility of coupling to magnetic mode as the pairing mechanism for superconducting electrons [97, 103].

However our results demonstrate, that the effect of the $q = (\pi, \pi)$ scattering in overdoped samples with high T_C (70K) is negligible. This puts a strong constrain on the superconductivity scenarios resulting from strong electron-electron correlations based in anisotropic spin channel.

On the other hand, the weakness of the $q = (\pi, \pi)$ scattering leads to the possibility of alternative pairing mechanism. As discussed in chapter 6, there is strong evidence for the significant electron-phonon coupling in cuprates. Further, the signature of the electron-phonon interaction is present at all dopings and even in the high temperature superconducting compounds where the magnetic mode is not present, e.g. $La_{2-x}Sr_xCuO_4$ [122]. Our conclusion is, that unlike phonons, $q = (\pi, \pi)$ interaction can not play a role of a universal pairing scenario for high temperature superconductors.

Chapter 9

Study of superconducting gap in Bi2212.

High resolution angle resolved photoemission data from pure $Bi_2Sr_2CaCu_2O_8$ (Bi2212) is presented. First photoemission observation of angle-resolved states above the Fermi level in high temperature superconductor is given. The results support the d-wave behavior near the nodal direction.

9.1 Introduction

Unusual symmetry of the superconducting gap in high critical temperature superconducting cuprates (HTSC) along with the high transition temperatures and AFM Mott insulator parent state was the main reason to consider cuprates as materials with non-phononic superconducting (sc) mechanism [123]. In the past decade different theories for the high transition temperature superconductivity emerged, each one explaining d-wave behavior differently and giving different predictions on the detailed shape of the gap in the momentum space (see. e.g. [124, 125, 126, 127, 128, 129]). The only tool able to give the detailed momentum dependent map of the superconducting gap is Angle-Resolved Photoelectron Emission Spectroscopy (ARPES). Significant recent advances in ARPES, such as 10-fold increase in energy and momentum resolution call for the new study of the gap.

Early ARPES reports were able to determine strong gap anisotropy and to fit the

ARPES data with different gap functions [78, 130, 131]. However, earlier results had a number of limitations. First, no reliable picture of the FS was available, because the existence of superstructure in the BiO layer masked the Fermi surface (FS) near the $M(\pi,0)$ point. As a result, earlier reports were not able to measure exactly the $\Delta_0(\vec{k})$, defined as the gap along the normal state Fermi surface, but measured a combination $\sqrt{\Delta(\vec{k})^2 + E(\vec{k})^2}$ along the perceived FS contour. Only recently the experiments on the Pb doped Bi2212 with suppressed superstructure were able to provide a unifying picture of the FS in Bi2212. Among other things existence of two Fermi surfaces due to the existence of two adjacent CuO_2 layers was demonstrated[115, 116, 117]. Second, the method of choice for determining the superconducting gap was the leading edge analysis (either by taking the mid-point, or by a fit). This analysis distorts the gap information, as the leading edge describes the gap for the signal uniform in energy, inappropriate for the peaky Bi2212 spectra. Without the high resolution, leading edge method was appropriate as a consistent way of gap mapping, however with improved resolution new methods for gap mapping are available, such as measurements of thermally excited states above the Fermi level for the small gap regions [132], or measuring positions of the well defined peaks.

In this chapter we present results of the superconducting gap mapping along the Fermi surface of Bi2212. Very high resolution data allowed us for the first time to observe angular resolved thermally excited states above E_F coexisting with states below E_F in certain momentum space regions, giving a direct proof of the splitting of the band by the opening of the gap.

9.2 Experiment

ARPES data have been recorded at beamline 10.0.1.1 of the Advanced Light Source (ALS) utilizing 33 eV for pure Bi2212 in $4 \cdot 10^{-11}$ $Torr$ or better vacuum. For high resolution studies on pure samples we chose 33 eV photon energy, because in our setup it gives highest resolution with small contribution from higher order light. The sample was kept in the fixed position relative to the beam polarization, and the analyzer was rotated. The beam polarization was in the sample plane perpendicular to the $\Gamma - Y$ direction, with beam nearly at grazing incidence with the sample surface. We used a Scienta SES 200 analyzer in the angle mode, where cuts parallel to $\Gamma - Y$ direction were carried out. In the 33 eV study the momentum resolution was $\pm 0.005 \mathring{A}^{-1}$ in the scan direction and $\pm 0.012 \mathring{A}^{-1}$ in the perpendicular direction and the energy resolution was 7 meV. The optimally doped pure Bi2212 ($Tc = 91K$) were grown using the floating-zone method. The single crystalline samples were oriented by using Laue diffraction ex situ and cleaved in situ in vacuum at the measurement temperature. The Fermi energy was obtained from the Energy Distribution Curves (EDCs) of polycrystalline Au.

9.3 Results and Discussion

In Fig. 9.1 we show energy distribution curves (EDCs) near the Fermi surface collected from pure optimally-doped $Bi_2Sr_2CaCu_2O_8$ at 60 K. Location of cuts shown in panels a)-h) is indicated in the Brillouin zone (BZ) picture in the inset of panel a). Panel a) also introduces angle ϕ used to denote different momentum-space cuts. A single spectrum away from any features was taken to represent background and was subtracted from all EDCs. Spectra shown in panels a)-h) are separated by .136°, or $0.05 \mathring{A}^{-1}$. Collection time for each cut was 2-3 hours to achieve good statistics with this extremely high resolution. In panels a)-c) and we see the main feature dispersing and peaking almost at the Fermi level, indicating Fermi level crossing. In panels d)-f), where substantial gap is open, we clearly see additional structure above the Fermi level. This structure looks like a high energy foot attached to the strong peak below E_F [133]. In Figure 9.2 we zoom in on the raw data used for panel e) of figure 9.1. The high energy foot is very well pronounced, as indicated by the shadowed area. In panel h), where the gap is really large, we do not see the high energy feature anymore.

We interpret this foot structure as the signature of the band above the Fermi level. BCS theory predicts that the conduction band $E(k)$ in superconducting state splits into $\sqrt{E(k)^2 + \Delta(k)^2}$ and $-\sqrt{E(k)^2 + \Delta(k)^2}$. We believe, that here for the

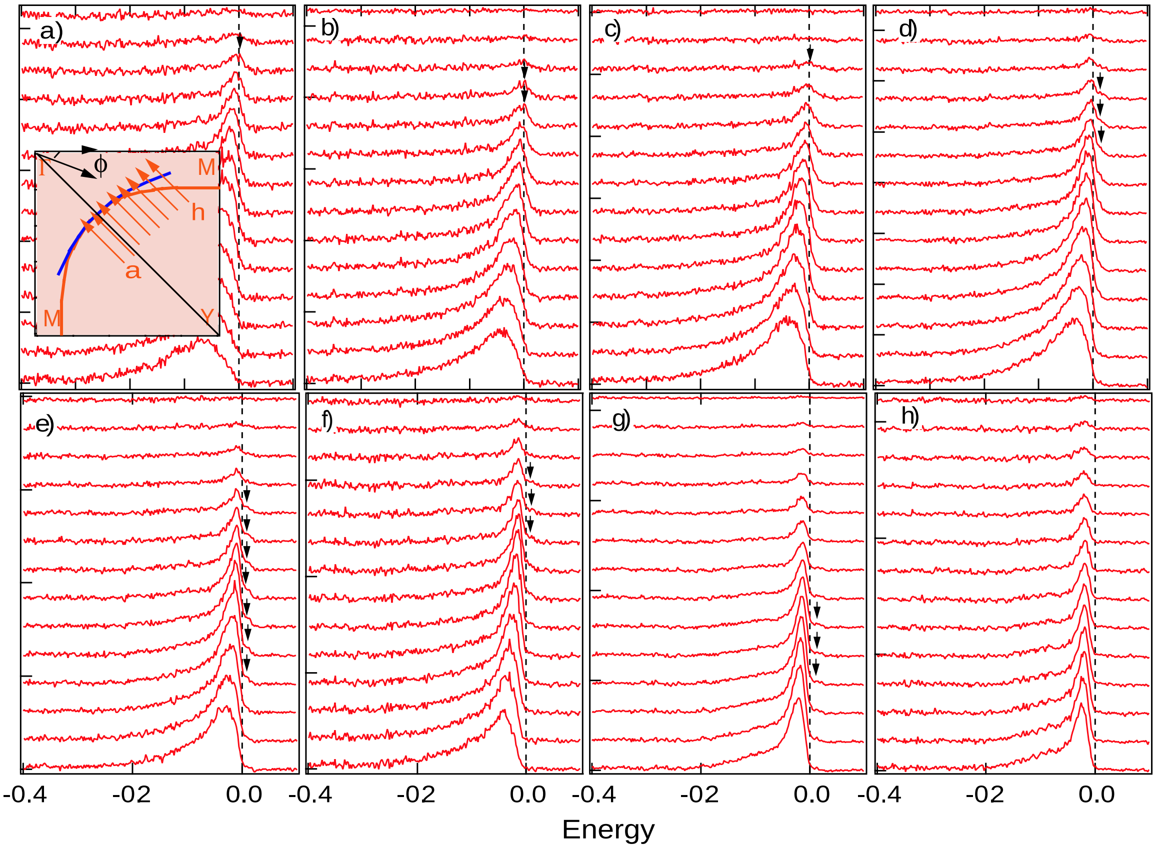

Figure 9.1: Panels a)-h) show EDC spectra of optimally doped pure Bi2212 at 60K with subtracted background along select cuts in the Bi2212 BZ. Spectra are separated by $0.003\mathring{A}^{-1}$. Inset of Panel a) shows the location of the cuts in the BZ, indicated by the red arrows.

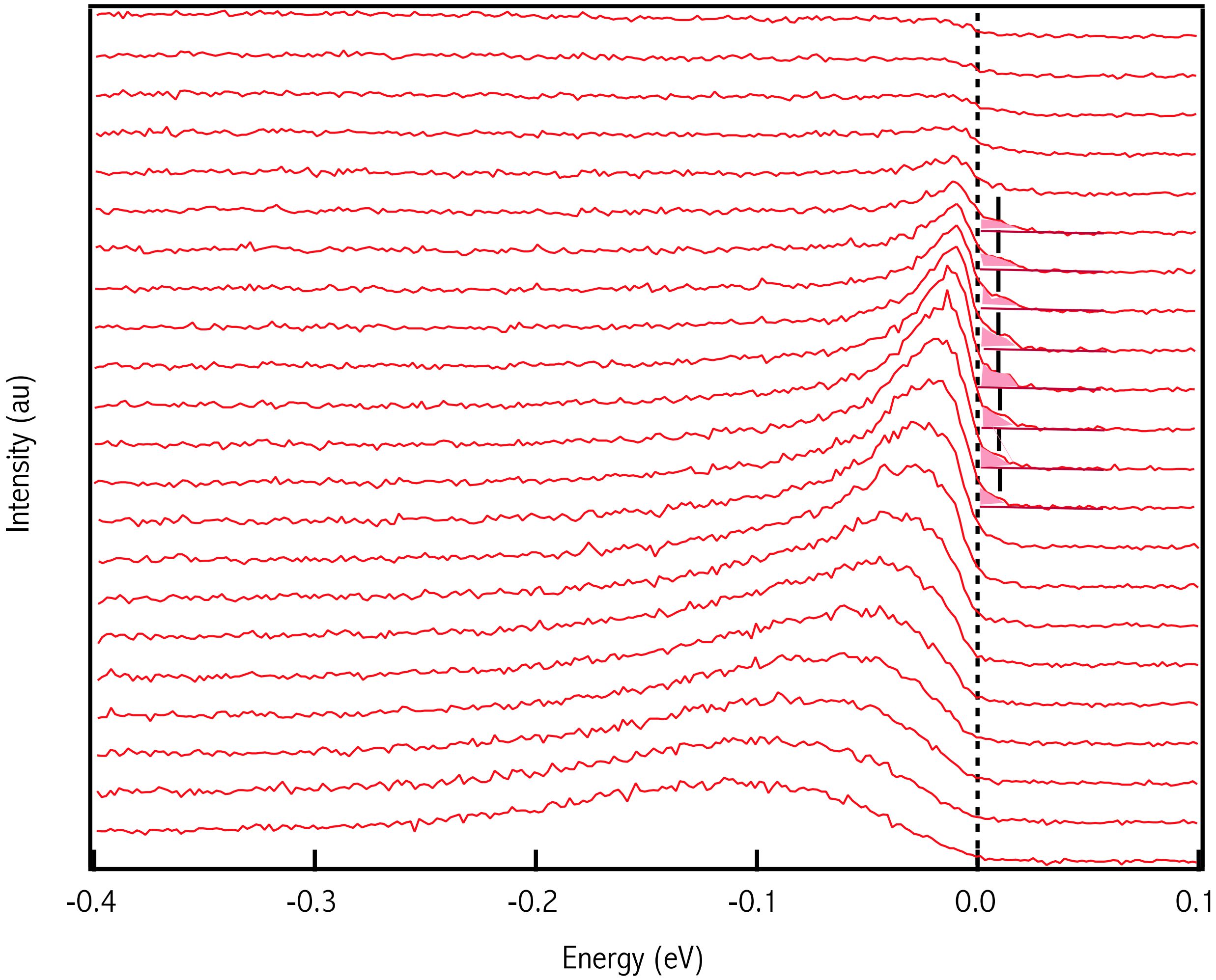

Figure 9.2: Raw data used for panel e) of Fig. 9.1.

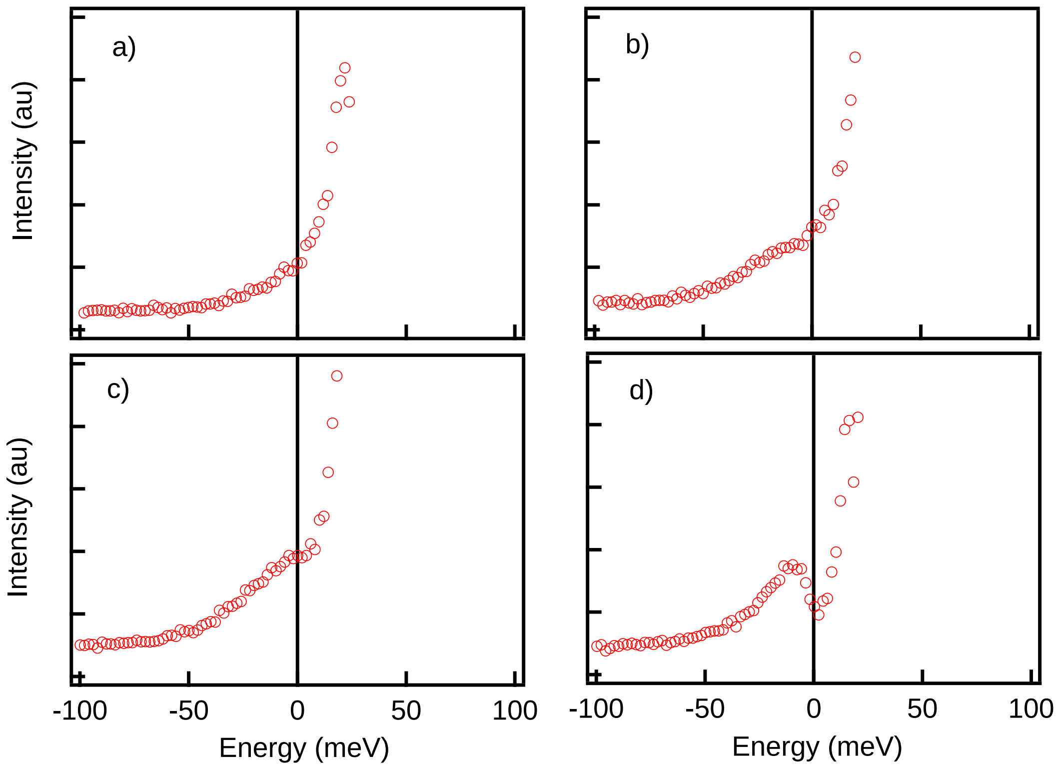

Figure 9.3: Spectra at 60 K at the Fermi surface of optimally doped pure Bi2212 sample divided by the Fermi-Dirac distribution function at 60K are shown. Spectra a) -d) correspond to Fermi surface crossings in cuts b) - e) in Fig. 9.1.

first time we demonstrate the spectroscopic evidence for the coexistence of these two bands in the same momentum space window in cuprate superconductor. This result is robust and was reproduced in several experiments. It can only be observed at sufficiently high temperature, with very high energy resolution and in a relatively small momentum window. For example, we do not see it in panels 9.1 a)-c), where the gap is too small, or in panel 9.1 h), where the gap is so large, that the feature above E_F is suppressed by the Fermi function.

We tried extracting the gap information from data directly, by dividing the spectra with the Fermi-Dirac function and measuring the spacing between the two peaks, see Fig. 9.3. The presence of the two peaks above and below E_F (in panel d)) in thus

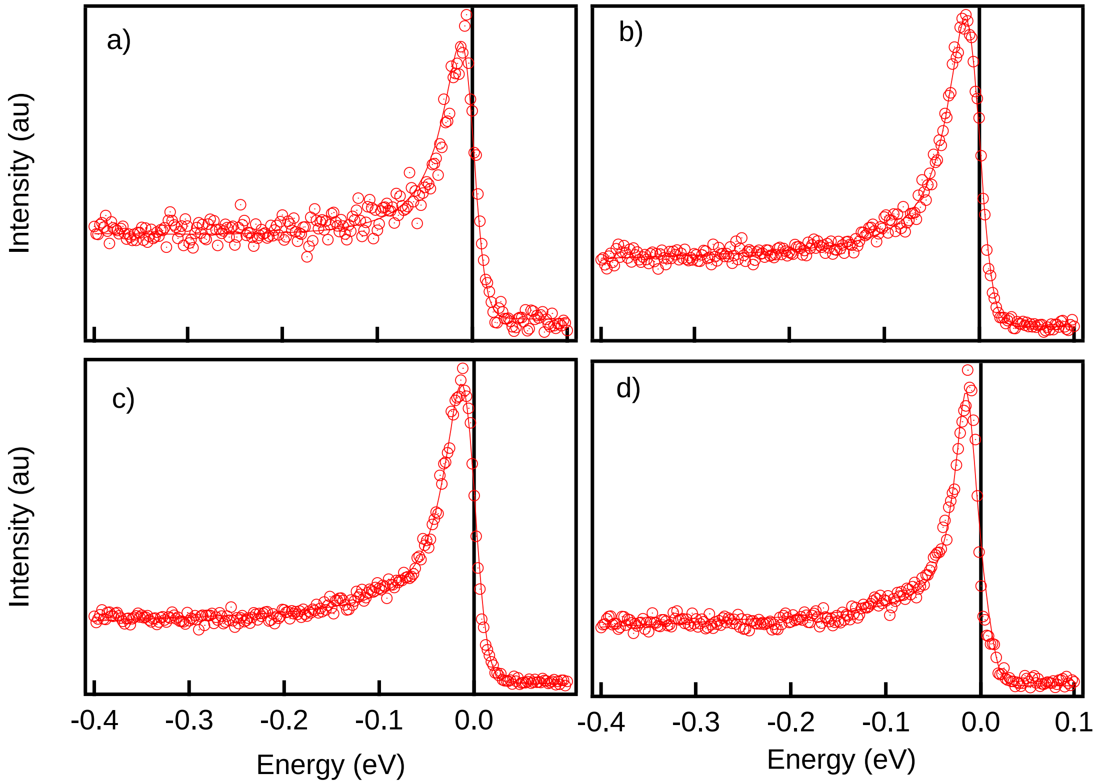

Figure 9.4: Open circles show single spectra at 60 K at the Fermi surface of optimally doped pure Bi2212 sample. Solid lines represent fits to the data (see text). Spectra a) -d) correspond to Fermi surface crossings in cuts b) - e) in Fig. 9.1.

extracted spectral function with a gap between them is a proof of the splitting of the band by the opening of the gap. However this method turns to be quite unreliable, especially in the small gap regions where the expected gap is smaller or comparable to our resolution, see panels a) - c). So instead we developed a simple fitting procedure to get quantitative gap information.

We model raw spectra near the Fermi surface by the sum of two Lorentzian peaks above and below Fermi level, equally spaced from the Fermi level, plus a smooth function below the Fermi level to represent inelastically scattered electrons (the results are insensitive to the form of the smooth function - we used parabola here). This sum is then multiplied by the resolution-broadened (7 meV) Fermi function, with chemical potential set at zero. A constant is added to the result to represent the signal from

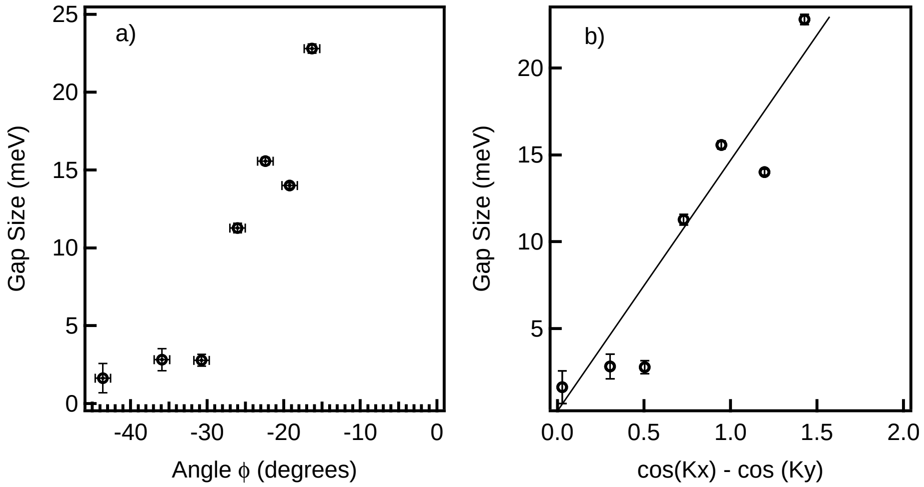

Figure 9.5: Panel a) shows the gap in optimally doped pure Bi2212 at 60K determined from the fits as a function of angle ϕ. Inset shows the spectra at the Fermi surface at $\phi = 36°$ with the fit from the procedure we use. Panel b) displays the gap versus a d-wave functional form.

higher order photons. The results of fits are shown in Fig. 9.4.

We conventionally define the Fermi surface to be the continuum of momentum space locations where the signal intensity at the chemical potential is largest. In Fig. 9.5 we present results from fitting the high resolution spectra at the Fermi surface by a procedure described above. We define the gap as the position of the peak determined from the fit. In panel a) we conventionally plot the gap from the fits as a function of azimuthal angle ϕ [131]. The inset demonstrates quality of the fit for $\phi = 26$ degrees data. To compare our data with d-wave functional form $\Delta(k) = \Delta_0 * (cos(Kx) - cos(Ky))$ in panel b) we plot the same data as a function of $cos(Kx) - cos(Ky)$, where K is in units of π. We see a pretty good agreement, and the linear fit gives the Δ_0 of $15meV$.

However, data away from the nodal point can be misleading due to the effect of the bilayer splitting [115, 116, 117]. Further research is needed to quantify the effect. We present some preliminary results in the Appendix A to these thesis.

In conclusion, unprecedented angular and momentum resolution allowed us for the first time to observe momentum-dependent thermally excited states above E_F

and to determine the superconducting gap near the node with great precision in pure $Bi_2Sr_2CaCu_2O_8$. We found the gap to be consistent with the d-wave form, with $\Delta_0 = 15meV$.

Chapter 10

Future directions.

The physics of high temperature superconductors is so rich that hundreds of PhD dissertations have been written on the topic, tens of them in the field of angle-resolved photoemission. New and often surprising results continue to be reported, so it is not a very productive job to try to predict the future. However, in this chapter I dare to propose some future experiments, which in my opinion have the highest potential to advance the field to the final understanding of HTSC phenomena.

10.1 Fermi Surface Studies

So far the results obtained with the new generation of ARPES experiments concerning the Fermi surfaces of cuprates were: the confirmation of the large Fermi Surface in cuprates, observation of one-dimensional character in striped 1/8 Nd-doped LSCO, and observation of bilayer splitting and photon energy dependence in two-layer Bi2212. The next thing to do is to look for bilayer splitting in double-layer LSCO and compare the splitting with Bi2212. If the inter-layer interaction is one of the factors in determining T_C, one would expect a smaller splitting in LSCO case, because electron-phonon coupling, as determined from dispersions, is very similar for both materials. It is also interesting to search for splitting in triple layer materials. The doping dependence of the Fermi surface in Bi2212 at very low dopings is also very important, because it can shed more light on evolution of the system from insulator to superconductor.

10.2 Energy Scale

By now it is fairly well established that the energy scale observed in Bi2212 and subsequently in Bi2201 and LSCO is due to electron-phonon coupling. The energy in all cases is very similar, maybe a little larger in LSCO case. It's important to study single-layer compounds with very high transition temperatures, such as Tl-based cuprate, to determine whether the energy scale is the same for all cuprates, or whether it increases with higher T_C as suggested by the drop-off in IR reflectivity measurements. Further, isotope effect measurements of the energy scale are in order, to confirm electron-phonon coupling explanation.

10.3 Mapping Gaps

There is a lot of research yet to be done to get the final picture of the evolution of the gap in cuprates with doping and temperature. In the overdoped regime, Pb-doped Bi2212 is the top choice, because it combines great crystal quality, large gap size, high transition temperature, and absence of superstructure. Unfortunately, Pb-doped Bi2212 is not available in underdoped (UD) regime, and strong superstructure in pure Bi2212 makes gap study controversial. The natural choice in UD regime is LSCO, because the UD crystal quality is very high. UD samples are particularly important because of the pseudogap phenomenon. Very high resolution studies, similar to that in chapter 6, have to be performed on UD crystals at various temperatures.

Appendix A

Preliminary study of the superconducting gap from Pb doped Bi2212 along the two resolved Fermi surfaces

In this appendix we present the preliminary study of superconducting gap from Pb doped $Bi_2Sr_2CaCu_2O_8$ (Bi2212) along the two resolved Fermi surfaces. Near anti-nodal point gap is determined as a function of ϕ for two pieces of bilayer-split Fermi surface. Results indicate that the gap for two different Fermi surfaces may not be described by a single gap function $\Delta(\vec{K})$.

ARPES data have been recorded at beamline 10.0.1.1 of the Advanced Light Source (ALS) utilizing 22 eV photon energy in $4 \cdot 10^{-11}$ $Torr$ or better vacuum. 22 eV photon energy was necessary to see two pieces of the FS in Pb-doped Bi2212 [117]. The sample was kept in the fixed position relative to the beam polarization, and the analyzer was rotated. The beam polarization was in the sample plane perpendicular

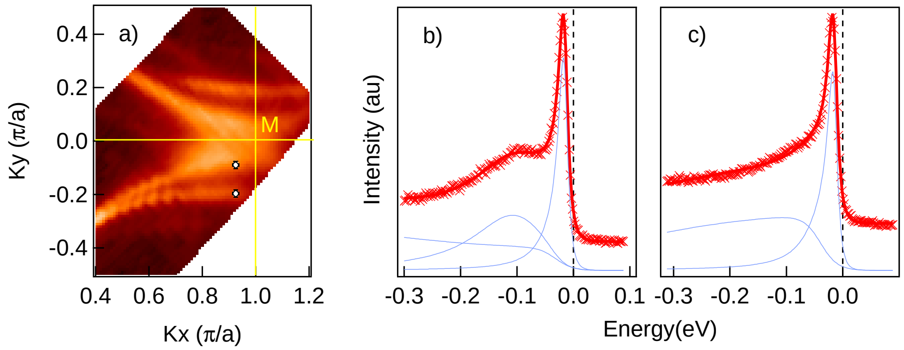

Figure A.1: Panel a) shows the Fermi surface map at 20K of the Pb-doped Bi2212. White circles indicate momentum space locations where the spectra shown in panels b) and c) were taken. Red crosses in panel b) show the spectra taken at the anti bonding Fermi surface, the one closer to the (1,0) point. Solid red line represents the fit to the data, and blue lines show fit components. Panel c) shows the spectra and the fit at the bonding Fermi surface.

to the $\Gamma - Y$ direction, with beam nearly at grazing incidence with the sample surface. We used a Scienta SES 200 analyzer in the angle mode, where cuts parallel to $\Gamma - Y$ direction were carried out. The momentum resolutions was $\pm 0.004\mathring{A}^{-1}$ and $\pm 0.011\mathring{A}^{-1}$, and the energy resolution was 16 meV. The overdoped Pb-doped Bi2212 ($Tc = 70K$) was grown using the floating-zone method. The single crystalline samples were oriented by using Laue diffraction ex situ and cleaved in situ in vacuum at the measurement temperature. The Fermi energy was obtained from the Energy Distribution Curves (EDCs) of polycrystalline Au.

A.1 Results and Discussion

To demonstrate the effect of this splitting we plot in panel a) of Fig A.1 the Fermi surface map of the Pb-doped $Bi_2Sr_2CaCu_2O_8$ at 22 eV photon energy. One clearly sees two high intensity contours in the BZ. The position of high intensity points is essentially the same as that at E_F for the normal state of the same sample [117] and indicates the Fermi surface location. The spectral line shapes that one obtains from

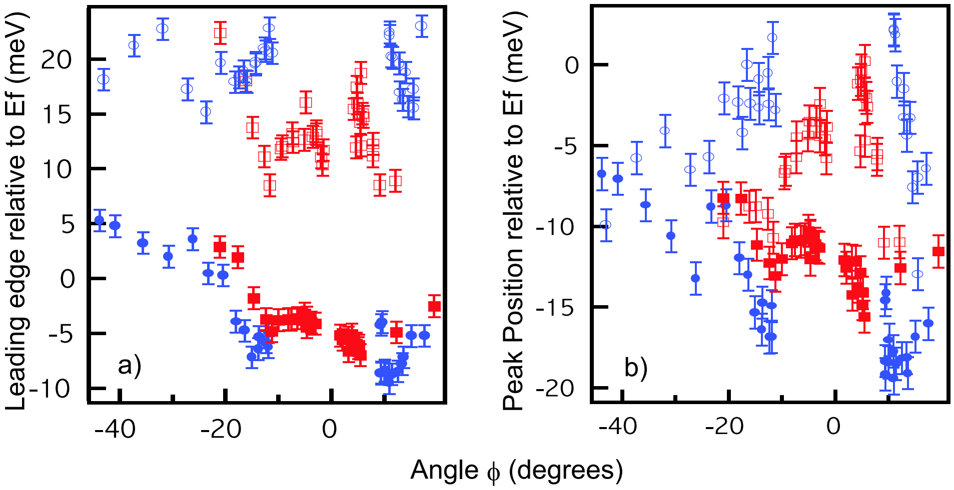

Figure A.2: In this figure 100K data is represented by open symbols, and 20K data is given by solid symbols. Red symbols represent the data from the anti-bonding Fermi surface, and blue symbols represent the data from bonding Fermi surface. Panel a) shows leading edge position of the peaks with respect to the Fermi level. Panel b) shows peak positions alone.

each FS piece are quite different. Inner piece gives a peak with a strong hump, shown in panel b). Outer piece of the Fermi surface, which crosses the $M - Y$ line further from the M point, gives a clear single peak as shown in panel c). Actually all EDCs in the area inside the inner Fermi surface have this famous peak and hump structure, with hump position consistent with outer band dispersion.

To extract quantitative data we use fitting procedures established in Chapter 7 to fit spectra at the Fermi surfaces from different bands. In Fig. A.2 we plot both peak positions and peak leading edges as determined by the fits. Because of the complexity of the line shapes we compare results from the normal state with the corresponding results from the superconducting state. We plot 100K data with open symbols and 20K data with solid symbols. Red symbols represent the data from the anti-bonding Fermi surface and blue symbols represent the data from the bonding Fermi surface.

In panel a) we plot leading edge positions as determined from the fits. Leading edge conventionally was the method of choice for defining superconducting gap (see, e.g. [78]), and it is interesting to check its validity with improved data. The leading edge is defined as the peak position plus HWHM of the fitted Lorentzian. In panel b)

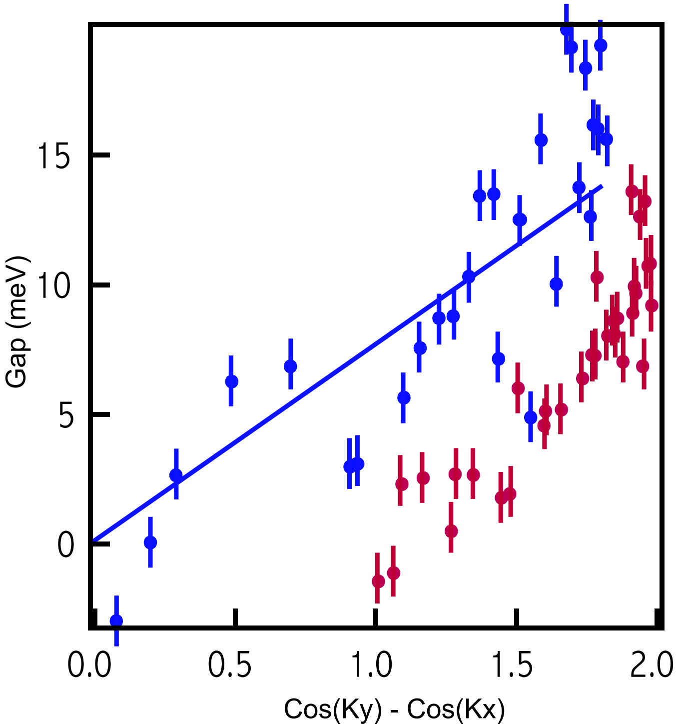

Figure A.3: This figure shows the gap in the Pb-doped Bi2212 vs a d-wave functional form. Blue symbols represent data from the bonding band, and red symbols represent the anti-bonding band. Straight blue line is the d-wave fit result for the bonding band.

we plot peak positions alone. We see that the difference in the leading edges above and below T_C is much larger than the change in peak positions. This is quite natural, as HWHMs of the peaks get narrower at lower temperature due to thermal effects. It is thus better to look at peak positions alone because they do not suffer from thermal broadening. There is additional problem which contaminates leading edge analysis. In Chapter 7 we have shown that peak widths decrease on approaching the $(\pi, 0)$ point. Thus leading edge method also distorts the gap information by artificially increasing the gap at $(\pi, 0)$ point.

We define the superconducting gap as the difference in peak positions between normal and superconducting state. Since we used slightly different locations on the Fermi surfaces to obtain peak positions for the two temperatures, we employ linear interpolation between the points to obtain continuous peak position curves. The resultant gap is shown in Fig. A.3. In this figure blue symbols represent data from the bonding band, and red symbols represent the anti-bonding band.

We clearly see that the gap from the bonding band is always larger than that of anti-bonding band. Bonding band gap appears to agree with the d-wave functional form with $\Delta_0 = 8meV$ as shown by the blue line in Fig. A.3, while the anti-bonding band gap appears to close already at $(cos(Ky) - cos(Kx)) = 1$ and can not be fitted by a simple d-wave. This means that it is necessary to include two different gaps in our discussion of the physics of $Bi_2Sr_2CaCu_2O_8$.

There is a strong possibility that our results are effected by the particulars of the fitting procedure. For example it is possible, that the double peak fitting gives consistently lower low energy peak position due to the presence of the broad hump. To check for this effect, we fitted the same peaks from bonding band (single peak) by both single peak and double peak functions. The results for peak positions were within $2meV$ of each other, but the double peak fit appeared to give slightly lower peak position. However, comparison of high temperature with low temperature data from the same momentum space points (the same line shape) should take care of the particulars of the fit function, that's why the result of apparent closing of the gap at $(cos(Ky) - cos(Kx)) = 1$ for the anti bonding band is likely reliable.

In conclusion, we used Pb-doped $Bi_2Sr_2CaCu_2O_8$ for a preliminary study the gap away from the node. We found the existence of two gaps. One is d-wave like, and occurs along the bonding band derived Fermi surface. The other one occurs along the anti-bonding band derived Fermi surface and does not appear to agree with simple d-wave functional form. These preliminary results, if true, put a strong constraint on the superconducting pairing mechanism.

Bibliography

[1] R. B. Laughlin and David Pines, PNAS **97** (2000), 28–31.

[2] Z. X. Shen and D. S. Dessau, Physics Reports **253** (1995).

[3] S. Hufner, *Photoemission spectroscopy*, Springer-Verlag, New York, 1995.

[4] Bansil *et al.*, Phys. Rev. Lett. **83**, 5154 (1999)

[5] Kipp *et al.*, Phys. Rev. Lett. **83**, 5551 (1999)

[6] R. Joynt, Science **284**, 777 (1999)

[7] T. Valla *et al.*, Science **285**, 2110 (1999)

[8] S. V. Borisenko *et al.*, Phys. Rev. Lett. **84**, 4453 (2000)

[9] H. M. Fretwell *et al.*, Phys. Rev. Lett. **84**, 4449 (2000)

[10] A. D. Gromko *et al.*, preprint, cond-mat / 0003017

[11] X. J. Zhou *et al.*, Science, **286**, 268 (1999)

[12] N. P. Armitage *et al.*, preprint

[13] M. Hengsberger *et al.*, Phys. Rev. Lett. **83**, 592(1999)

[14] T.Valla *et al.*, Phys. Rev. Lett. **83**, 2085 (1999)

[15] J. W. Allen *et al.*, J. Phys. Chem. Solids, **56**, 1849 (1995)

[16] P. V. Bogdanov *et al.*, Phys. Rev. Lett. **85**, 2581 (2000)

[17] C. M. Varma, *et al.*, Phys. Rev. Lett. **63**, 1996 (1989)

[18] J. Bardeen *et al.*, Phys. Rev. **108**, 1175 (1975)

[19] M. L. Cohen and P. W. Anderson, AIP Conf. Proc. 4, *Superconductivity in d- and f- Band Metals*, p. 17 (1972)

[20] for general discussion see e.g. P.W. Anderson, *The Theory of superconductivity in the high-TC cuprates*, Princeton University Press, Princeton (1997) and references therein

[21] B. Batlogg *et al.*, Phys. Rev. Lett. **58**, 2337 (1987)

[22] T. Timusk and B. Statt, Rep. Prog. Phys. **62**, 61 (1999)

[23] E. Dagotto, Rev. Mod. Phys. **66**, 763 (1994)

[24] F. C. Zhang and T. M. Rice, Phys. Rev. B **37**, 3759 (1988)

[25] S. A. Kivelson *et al.*, in *Strongly Correlated Electronic Materials: The Los Alamos Symposium 1993*, edited by K. S. Bedell, Z. Wang, D. E. Meltzer, A. V. Balatsky and E. Abrahams, (Addison-Wesley, Reading, Massachusetts, 1994) p619

[26] V. J. Emery *et al.*, Phys. Rev. B **56**, 6120 (1997).

[27] J. Zaanen and O. Gunnarson, Phys. Rev. B **40**, 7391 (1989).

[28] J. M. Tranquada *et al.*, Nature **375**, 561 (1995)

[29] J. M. Tranquada *et al.*, Phys. Rev. B **59**, 14712 (1999).

[30] K. Yamada *et al.*, Phys. Rev. B **57**, 6165 (1998); Y. S. Lee *et al.*, Phys. Rev. B **60**, 3643 (1999); Wakimoto *et al.*, cond-mat/9908115

[31] D. Poilbanc *et al.*, Phys. Rev. B **39**, 9749 (1989).

[32] H. J. Schulz, J. Phys. (Paris) **50**, 2833 (1989).

[33] C. Castellani *et al.*, Phys. Rev. Lett. **75**, 4650 (1995).

[34] A. H. Castro Neto *et al.*, Phys. Rev. Lett. **76**, 2165 (1996).

[35] J. Zaanen *et al.*, Phys. Rev. B **53**, 8671 (1996).

[36] H. Eskes *et al.*, Phys. Rev. B **54**, R724 (1996)

[37] H. Eskes *et al.*, Phys. Rev. B **58**, 6963 (1998).

[38] C. Morais Smith *et al.*, Phys. Rev. B**58**, 453 (1998).

[39] S. A. Kivelson *et al.*, Nature **393**, 550 (1998).

[40] J. Zaanen *et al.*, Phys. Rev. B **58**, R11868 (1998).

[41] N. Hasselmann *et al.*, Phys. Rev. Lett. **82**, 2135 (1999).

[42] J. Zaanen *et al.*, Annalen der Physik **5**, 224 (1996).

[43] C. Nayak *et al.*, Phys. Rev. Lett. **78**, 2465 (1997).

[44] M. I. Salkola *et al.*, Phys. Rev. Lett. **77**, 155 (1996).

[45] S. R. White *et al.*, Phys. Rev. Lett. **81**, 3227 (1998).

[46] T. Tohyama *et al.*, Phys. Rev. Lett. **82**, 4910 (1999).

[47] A. V. Balatsky *et al.*, Phys. Rev. Lett. **82**, 5337 (1999).

[48] B. O. Wells *et al.*, Science **277**, 1067 (1997).

[49] G. Aeppli *et al.*, Science **278**, 1432 (1997).

[50] H. A. Mook *et al.*, Nature **395**, 580 (1998).

[51] A. W. Hunt *et al.*, Phys. Rev. Lett. **82**, 4300 (1999).

[52] P. H. Dickinson and S. Doniach, Phys. Rev. B **47**, 11447 (1993).

[53] Y. Nakamura and S. Uchida, Phys. Rev. B **46**, 5841 (1992).

[54] M. v. Zimmermann *et al.*, Europhys. Lett. **41**, 629 (1998).

[55] A. Ino *et al.*, cond-mat/9809311 (1998); cond-mat/9902048 (1999).

[56] T. Noda *et al.*, Scienc **286**, 265 (1999)

[57] S. W. Cheong *et al.*, Phys. Rev. Lett. **67**, 1791 (1991)

[58] T. E. Mason *et al.*, Phys. Rev. Lett. **68**, 1414 (1992)

[59] A.Bianconi *et al.*, Phys. Rev. Lett. **76**, 3412 (1996).

[60] M. Fleck *et al.*, Phys. Rev. Lett. **84**, 4962 (2000)

[61] M. G. Zacher *et al.*, Phys. Rev. Lett. **85**, 2585 (2000)

[62] S. R. White *et al.*, Phys. Rev. Lett. **80**, 1272 (1998).

[63] J.-H. Xu, T. J. Watson-Yang, J. Yu, and A. J. Freeman, Phys. Lett. A **120**, 489 (1987).

[64] T. Yoshida *et al.*, Phys. Rev. B **63**, 220501-1 (2001).

[65] X. J. Zhou *et al.*, Phys. Rev. Lett. **86**, 5578 (2001)

[66] M. R. Norman, preprint, cond-mat / 9912203

[67] C. G. Olson *et al.*, Science **245**, 731 (1989)

[68] D. Dessau *et al.*, Phys. Rev. Lett. **71**, 2781 (1993)

[69] P. Aebi *et al.*, Phys. Rev. Lett. **72** 2757 (1994)

[70] Jian Ma *et al.*, Phys. Rev. B **51**, 3832 (1995)

[71] A. G. Loeser *et al.*, Science **273**, 325 (1996)

[72] P. J. White *et al.*, Phys. Rev. B **54**, 15669 (1996)

[73] H. Ding *et al.*, Phys. Rev. Lett. **76**, 1533 (1996)

[74] M. R. Norman *et al.*, Nature **392**, 157 (1998)

[75] N. L. Saini *et al.*, Phys. Rev. Lett. **79**, 3467 (1997)

[76] Y. -D. Chuang *et al.*, Phys. Rev. Lett. **83**, 3717 (1999).

[77] D. L. Feng *et al.*, preprint, cond-mat / 9908056.

[78] J. Mesot *et al.*, Phys. Rev. Lett. **83** 840 (1999)

[79] S. Legner *et al.*, preprint, cond-mat / 0002302.

[80] P. Schwaller *et al.*, J. Elec. Spec. Rel. Phen., **76** 127 (1995).

[81] A. Bansil *et al.*, private communication

[82] W. L. MacMillan and J.M.Rowell, *Superconductivity*, R.D.Parks Ed., Vol.1 (M.Dekker Inc., New York, 1969, Chap.11, p. 561)

[83] D. J. Scalapino *et al.*, Phys. Rev. **148**, 263(1966)

[84] D. J. Scalapino, *Superconductivity*, R.D.Parks Ed., Vol.1 (M.Dekker Inc., New York, 1969, Chap.11, p. 561)

[85] S. Chakravarty *et. al*, Phys. Rev. B **39**, 2344 (1989)

[86] S. Sachdev *et al.*, Phys. Rev. Lett. **69**, 2411 (1992)

[87] A. Sokol *et al.*, Phys. Rev. Lett. **71**, 2813 (1993)

[88] V. J. Emery *et al.*, Phys. Rev. Lett. **71**, 3701 (1993)

[89] C. M. Varma, Phys. Rev. B **55**, 14554 (1997)

[90] R. B. Laughlin, *cond. mat.* 9709195

[91] S.Massida *et al.*, Physica C **152**, 251(1988)

[92] H. Krakauer and W.E.Pickett, Phys. Rev. Lett. **60**, 1665 (1988)

[93] P. V. Bogdanov *et al.*, unpublished

[94] A. Puchkov et. al., Phys. Rev. Lett. **77**, 3212 (1996)

[95] A. Kaminski *et al.*, Phys. Rev. Lett. **84**, 1788 (2000)

[96] A. V. Puchkov *et al.*, J. Phys. Cond. Matter **8**, 100049 (1996)

[97] M. Eschrig *et al.*, Phys. Rev. Lett. **85**, 3261 (2000).

[98] H. He *et al.*, cond-mat 0002013 (2000).

[99] R. J. McQueeney *et al.*, Phys. Rev. Lett. **82**, 628 (1999)

[100] Y. Petrov *et al.*, cond-mat 0003414 (2000)

[101] S. Lashell *et al.*, Phys. Rev. B **61**, 2371 (2000)

[102] J. C. Campuzano *et al.*, Phys. Rev. Lett. **83**, 3709 (1999)

[103] P. D. Johnson *et al.*, cond-mat 0102260 (2001)

[104] H. F. Fong *et al.*, Phys. Rev. B **54**, 6708 (1996)

[105] A. Lanzara *et al.*, Nature **412**, 510 (2001)

[106] A. Kaminski *et al.*, cond-mat 0004482 (2000)

[107] H. Takagi *et al.*, Phys. Rev. Lett. **69**, 2975 (1992)

[108] O. Gunnarsson, Rev. Mod. Phys. **69**, 575 (1997)

[109] B. Batlogg *et al.*, Physica C **235**, 130 (1994)

[110] M. L. Kulic, Physics Reports **338**, 1 (2000).

[111] F. Ronning, Ph.D. thesis, Stanford University

[112] Z. -X.Shen and J. R. Schrieffer, Phys. Rev. Lett. **78**, 1771 (1997)

[113] A. Ino, Phys. Rev. B **62**, 4137 (2000)

[114] C. Kim *et al.*, Phys. Rev. Lett. **80**, 4245 (1998)

[115] D. L Feng *et al.*, Phys. Rev. Lett. **86**, 5550 (2001)

[116] Y. D. Chuang *et al.*, Phys. Rev. Lett. **87**, 117002 (2001)

[117] P. V. Bogdanov *et al.*, Phys. Rev. B **64**, 180505 (2001)

[118] H. F. Fong *et al.*, Phys. Rev. Lett. **75**, 316 (1995)

[119] H. F. Fong *et al.*, Nature **398**, 588 (1999)

[120] J. Rossat-Mignod *et. al*, Physica C **235**, 59(1994)

[121] P. Dai *et. al*,Phys. Rev. Lett. **77**, 5425 (1996)

[122] M. A. Kastner *et al.*, Rev. Mod. Phys. **70**, 897 (1998)

[123] P.W. Anderson, *The Theory of superconductivity in the high-TC cuprates*, Princeton University Press, Princeton (1997)

[124] R.J Radtke *et al.*, Phys. Rev. B **53** 5137 (1996)

[125] S.D. Adrian *et al.*, Phys. Rev. B **56** 7878 (1997)

[126] B. Chattopadhyay *et al.*, Phys. Lett. A **246** 201 (1998)

[127] A.N. Das *et al.*, Physica C **294** 97(1998)

[128] G.G.N. Angilella *et al.*, Eur. Phys. Journal B **15** 269-75 (2000)

[129] M. G. Zacher *et al.*, Phys. Rev. Lett. **85** 824 (2000)

[130] Z.-X. Shen *et al.*, Science **267** 343 (1995)

[131] H. Ding *et al.*, Phys. Rev. B **54** R9678 (1996)

[132] inspired by the talk of S. Hufner at the ALS, Spring 2000

[133] F. Reinert *et al.*, Phys. Rev. Lett. **85** 3930 (2000)